Università degli Studi di Padova
Department: Centro Ricerche Fusione
Università degli Studi di Napoli Federico II

JOINT RESEARCH DOCTORATE IN FUSION SCIENCE AND ENGINEERING
Cycle XXXVI

TITLE

Modeling and correction of 3D error fields in tokamak plasmas

Coordinator: Prof. Gianmaria De Tommasi

Supervisor:

Prof. Fabio Villone

Co-Supervisor:

Prof. Raffaele Albanese

Prof. Raffaele Martone

Prof. Andrea Gaetano Chiariello

Ph.D. student:
Pasquale Zumbolo

Padova, October 2023

List of Figures

List of Tables

Acknowledgements

The activity described in this manuscript was carried out with the assistance, direction, and active involvement of several people whom I had the honour of collaborating with.

In particular, I want to express my gratitude to my mentors, Prof. Raffaele Albanese, Prof. Andrea Gaetano Chiariello, Prof. Raffaele Martone, and Prof. Fabio Villone. They trained me and played an important role for achieving this result.

Next, I would like to thank Proff. M. De Magistris and V.P. Loschiavo for their influence on the writing of this manuscript.

During these three years, I met many people which contributed to my scientific formation and excitement towards research. I would like to thank Francesco Maviglia for the intense scientific discussions we had during my stay in Garching and the other researchers I met at the EUROfusion headquarters, and I would like to thank Prof. Salvatore Ventre for sharing his expertise and for his support in approaching the CARIDDI code. His advice was extremely important. I would like to express my sincere gratitude to the CREATE research group, especially to the students and several young researchers with whom I had the privilege to share the office and who became friends during these years (too many to list all of you without forgetting anyone ☺).

Finally, beyond my daily research environment, I would like to thank my old friends for their constant support during our weekends together.

Dedicated to my Family

To my parents, Antonio and Maria,
and my sister, Roberta,
for always believing in me.
To my girlfriend, Giusy,
for always encouraging me.
Without her deep affection
and empathy, this goal would
not have been possible. I love you ♡.

Contents

Summary

THE high demand for energy and the environmental, concerns associated with the greenhouse effect and global warming, necessitate the development of renewable energy sources. Controlled thermonuclear fusion holds immense promise as a decisive contribution to the medium-term global energy problem. The process is clean, highly secure, and theoretically capable of providing vast amounts of energy. However, achieving nuclear fusion on Earth requires substantial scientific and technological efforts. The fuel, in the state of *plasma*, is made up of charged particles that should be appropriately confined to produce nuclear fusion reactions, similar to what naturally happens in the Sun. Mainly two "artificial" confinement approaches are currently under investigation: inertial confinement, based on the use of high coherence lasers, and magnetic confinement, based on high magnetic fields. The most promising configuration for future commercial reactors are the *Tokamaks*, based on magnetic confinement. These machines have a toroidal geometry and are in principle axisymmetric. The presence of high magnetic fields allows: to induce the plasma current, to confine the charged particles and to control the shape of the plasma ring. The plasma current, on the order of $10^6 \div 10^7$ A, plays a dual role: provides heating (through ohmic dissipation) and stabilizes the plasma itself.

Three-dimensional effects, known as Error Fields, can significantly impact tokamak performance. Error fields refer to small imperfections or deviations in the symmetry and uniformity of the tokamak's magnetic fields. These errors can arise from various reasons, including manufacturing tolerances, mechanical deformations, or electromagnetic interactions. Although these errors may appear as minor issue, they can profoundly affect plasma confinement stability and performance. Presence of error fields can in fact lead to plasma disruptions, caused by instabilities and confinement losses. These disruptions not only reduce fusion efficiency but also risk damaging the tokamak's plasma-facing components. In extreme cases, such disruptions can release substantial amounts of energy and heat, potentially damaging the tokamak itself.

Researchers and engineers work on mitigating error field effects through advanced control techniques and sophisticated magnetic field shaping. Understanding and managing error fields, together with other still open problems, are critical steps towards achieving a stable and efficient fusion reactor. Here, the model for the estimation and treatment of error fields is presented, on which the candidate concentrated his contribution. The approach allows to take into account both assembly and manufacturing uncertainties of the magnetic system. The uncertainties are projected in a suitable functional space of finite dimension, called space of parameters, and, a relation between the set of the parameters and the perturbed field contribution is obtained via geometry modelling of the coils. In the limit of small perturbations, this complex model provides a linear relation suitable for Monte Carlo analysis of the error fields impact. The procedure has been successfully applied for the estimation of error fields in two tokamaks: the Divertor Tokamak Test (DTT) facility, the Italian tokamak under construction at the Frascati ENEA Research Center, Rome, and DEMO, the European demonstration power plant, where the plasma response to the error fields was also taken into account by integrating the procedure with the MARS code. In order to develop an alternative linearized plasma response model, the continuity of the magnetic field should be guaranteed. A technique, acts as a post-processor of the magnetic flux solution of the Grad-Shafranov equation employing Helmholtz's theorem, is also shown, to which the candidate has made a further contribution. The procedure, based on the triangular elements, provides magnetic field with an accuracy of $O(h^2)$ resulting in reliable linearized models derived with limited computational effort.

1 Introduction

Most of the energy production, from electricity for our homes to fuel for our cars, comes from fossil fuels, namely oil, gas, and coal. Over the past half-century, numerous alternative energy sources have been developed and refined. Some of these are the so-called "clean" energy sources, which have been spreading in recent years, thanks in part to increased public awareness. Unfortunately, due to various technical and technological limitations, they are currently unready for large-scale deployment and can only serve as complementary resources. Nuclear fission is one of the leading low carbon power generation methods of producing electricity. Unfortunately, it has with important limitations related to the the disposal of waste materials. Meanwhile, in the basket of these alternatives, fusion energy could offer the potential for an unlimited and clean main energy source. In this chapter the controlled thermonuclear fusion is presented as well as the most promising reactor models.

1.1 Nuclear reactions and mass defect

Currently, the use of fission energy might be an alternative to fossil fuels for large scale electricity production. Nuclear fission is the physical process in which the atomic nucleus of a heavy element is split into two or more nuclei and a variable number of new neutrons following a collision with a neutron. The total mass of each of the fission fragments is less than the mass of the starting atomic nucleus. A large amounts of energy (fission energy), corresponding to this "mass defect", is released after this process. This amount, can be calculated by the Einstein's equation, $\Delta E = c^2 \Delta m$,

where ΔE is the nuclear binding energy (see Fig. 1.1) and Δm the mass defect [1].

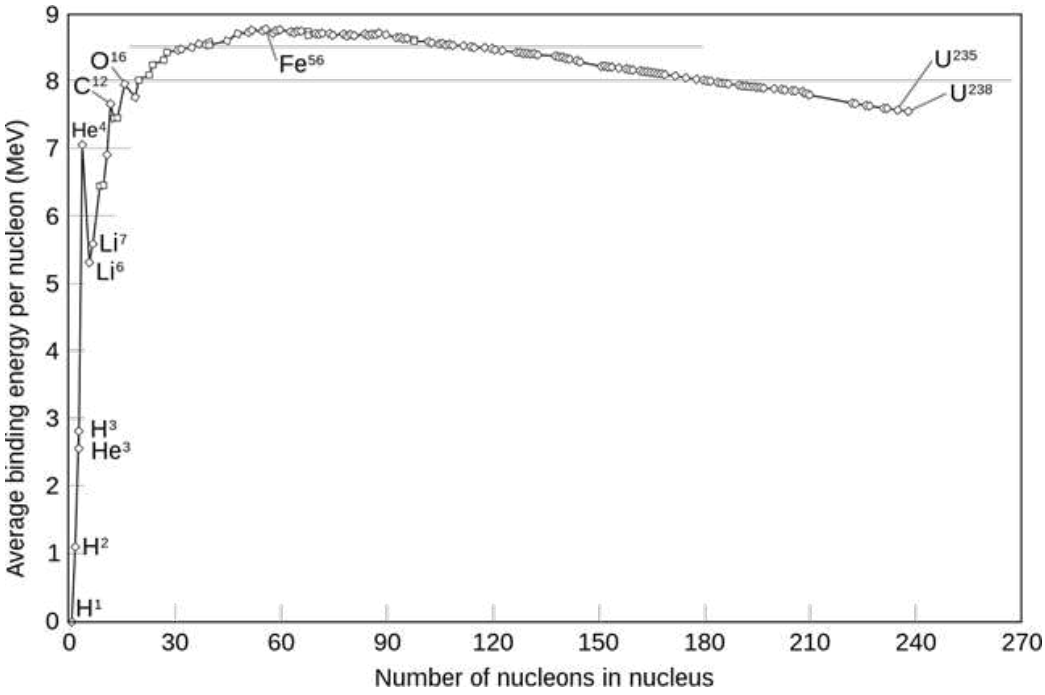

Figure 1.1: Binding energy ΔE per nucleon versus atomic number A.

The first artificial nuclear fission was achieved in 1932 by scientists Ernest Walton and John Cockcroft, who, by accelerating protons against a lithium-7 atom, managed to split its nucleus into two alpha particles [2]. The first reaction involving heavy atoms was performed by the scientist Otto Hahn together with the physicist Lise Meitner. Hahn continued the research work that had been initiated in 1934 by the Italian physicist Enrico Fermi with the bombardment of uranium with neutrons, resulting in what Hahn called an "explosion" of the uranium nucleus into atomic nuclei of medium weight. It is important to underline that, the nuclear fission research also had a great acceleration during the World War II, when the first nuclear weapon was developed (the Manhattan Project). One practical phenomenon of exceptional interest, resulting from neutron emission after nucleus fission, is the chain reaction. In fact, if each of the neutrons resulting from a fission causes other fission reactions, the number of these grows rapidly. A sole a single initial neutron is sufficient to provoke the fission of an enormous number of nuclei in the target (Fig. 1.2) [4]. Nuclear fission power plants are designed precisely to activate and simultaneously control, using appropriate materials called

moderators, a chain reaction based on ^{235}U, from which heat is derived to be transformed into electrical energy. Nuclear weapons, on the other hand, are specifically engineered to produce a reaction that is so fast and intense it cannot be controlled after it has started and leads to an explosive energy release.

The approximately 440 nuclear power plants scattered around the world contribute a significant and growing fraction of the total electrical power (in 2021 nuclear plants supplied 2653 TWh of electricity, up from 2553 TWh in 2020) [3][4][5]. Being a low-carbon energy source with relatively little land-use requirements, nuclear energy can have a positive environmental impact from this point of view. As well known, there are further environmental considerations and potential risks associated with nuclear energy, primarily coming from the management of radioactive waste and the risks of accidents or intentional attacks. However, historically there have only been few disasters at nuclear power plants with known relatively substantial environmental impacts.

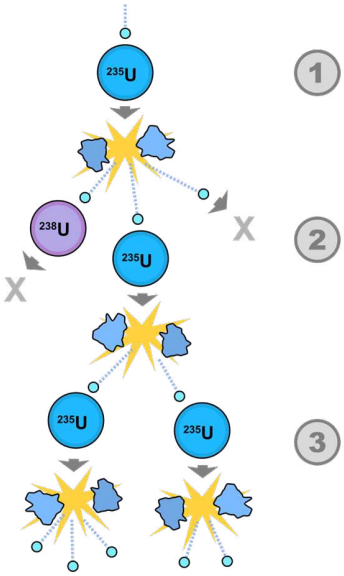

Figure 1.2: Sketch of a fission reaction of a core of ^{235}U.

Nuclear fusion is the reverse process compared to fission and occurs when two nuclei of an element with a low atomic number (e.g., hydrogen) combine to form a nucleus with a higher atomic number. In order to trigger a fusion reaction, the nuclei must be brought close together with an enormous force, which allows them to overcome electrostatic repulsion and let the "strong" short-range nuclear forces prevail (Fig. 1.3).

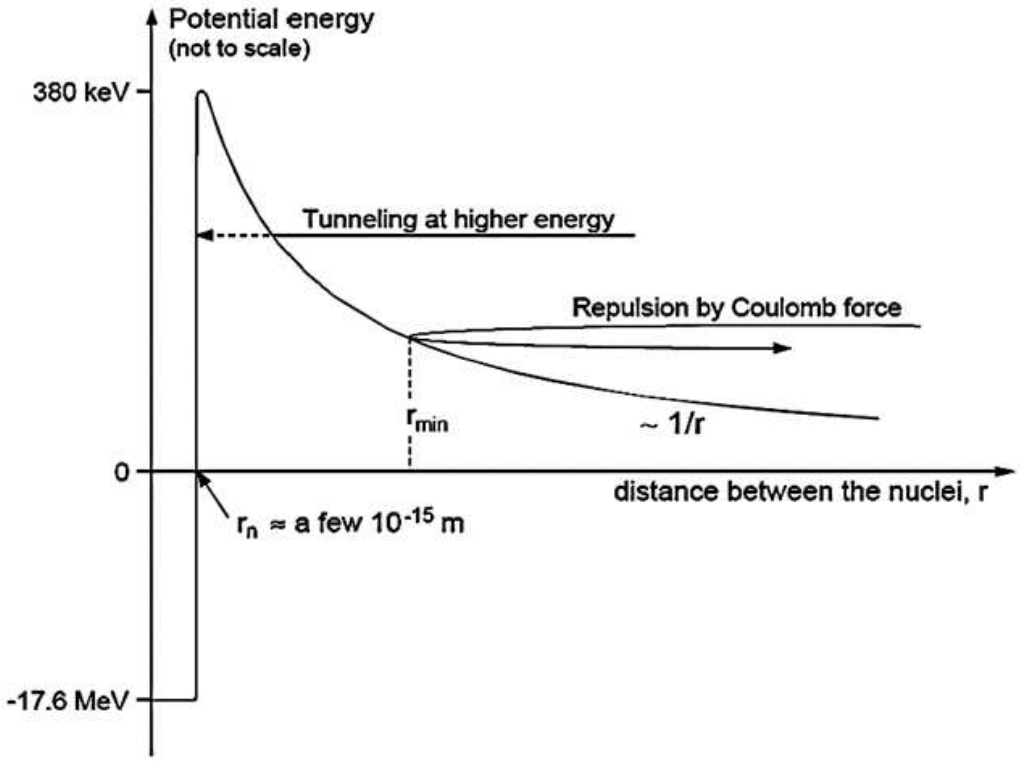

Figure 1.3: Coulomb barrier (electrostatic repulsion) between two nuclei.

The nucleus produced by the reaction has a lower mass than the sum of the masses of the reacting nuclei because the mass of the nucleons of the intermediate elements is lower than that of the elements with low and high atomic numbers. It is precisely this mass defect, converted into energy again through Einstein's equation. This reaction is the same as the one continuously occurring in stars; in fact, the core of the Sun is predominantly composed of hydrogen (H) and its isotopes, deuterium (D), with one neutron and one proton, and tritium (T), with two neutrons and one proton. As the temperature reaches around 16 million degrees and the pressure is extremely high, there are optimal conditions for a fusion reaction. Hydrogen, deuterium and tritium are ionized, and thanks to the high temperatures, many fusion reactions are triggered, ensuring self-sustainability. It should be noted that as a consequence of this process occurring in all stars, 99.9% of the visible matter in the universe exists as plasma[6][7][8].

1.1.1 Controlled Thermonuclear Fusion

In order to obtain fusion reactions a plasma has to be heated up to very high temperature. The artificial plasma confinement [6][7][9] is now-day a critical issue for physicists and engineers involved in design of thermonuclear fusion power devices. The "mechanical" container is not practicable, since a contact of the high energy particles with a "physical" wall, will provide a strong and rapid cooling of the plasma. In the stars' cores the gravitational forces are so strong to be able to compress the matter up to very large densities and pressures, in such a way that the thermonuclear fusion reactions operate at a fully steady state rate (gravitational confinement). This approach cannot be adopted on the earth for obvious reasons. Beyond gravitational confinement, mainly two possibilities have been investigated during the last decades:

- The inertial confinement [10]: involves high density plasmas confined and heated for a very limited time. The idea is to use a fuel capsule called "pellet", compressed by means of an inward shock wave (e.g. X-rays created by a laser source). The inertia of the fuel keeps it from escaping, hence the name "inertial". The main problems are related to the efficiency of the required large laser sources and to the automation of the process. The National Ignition Facility, in Livermore, California, on December 5, 2022, announced important milestone for this technology, using 192 laser beamsand producing 3.15 megajoules of energy from a 2.05 megajoule input of laser light (somewhat less than the energy needed to boil 1 kg of water) [11].

- The magnetic confinement [12]: is, instead, the most promising approach along the road to the realization of a fusion power plant. The idea is to use magnetic fields properly generated by suitable coils, to confine plasma charged particles. The approach has given satisfying results in several reactor configurations, mainly Tokamaks [6], Reversed Field Pinches (RFPs) [13] and Stellarators [14]. In the thesis activity particular attention has been given to the Tokamak, that now-day represents the most promising configuration of magnetic fusion device

. The most promising reaction for commercial applications is the one between a deuterium nucleus and a tritium nucleus, since has the highest reaction rate (defined later) at the lowest temperature (Fig. 1.4).

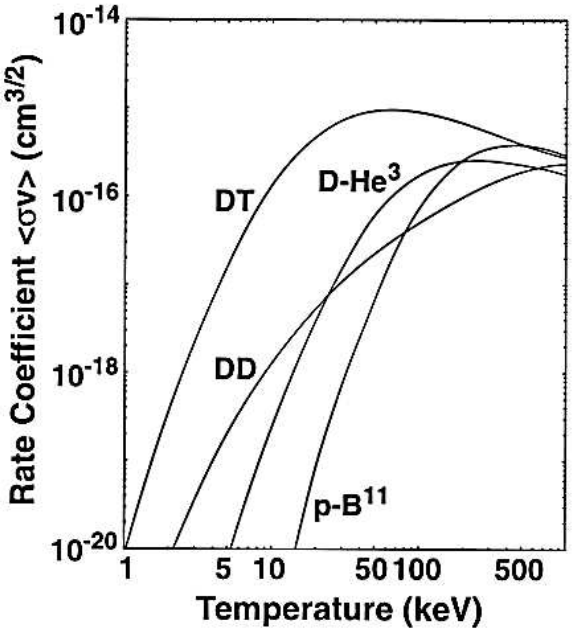

Figure 1.4: Reaction rate as a function of temperature.

D–T reaction produces a helium nucleus (alpha particle) and a neutron [6]:

$$^{2}\mathbf{D} + {}^{3}\mathbf{T} \rightarrow {}^{4}_{2}\mathbf{He} + n \tag{1.1}$$

In (1.1), the products have higher atomic numbers, leading to a lower total mass compared to that of the interacting particles. As a result, energy is released following the principle of mass-energy equivalence mentioned earlier. The liberated energy is distributed between the alpha particle and the neutron in inverse proportion to their respective masses. Therefore, the majority of the energy will be present in the free neutron in the form of kinetic energy. Specifically, 17.6 MeV of kinetic energy is released in the resulting products, 14.1 MeV in the neutron, and 3.5 MeV in the alpha particle (helium). These amounts of energy are enormous; in fact, in 1 kg of deuterium there are approximately $3{\times}10^{26}$ atoms and so the energy released per kilogram would be $2.35{\times}10^{10}$ kWh ($5.27{\times}10^{29}$ MeV) [15].

Deuterium can be found in seawater and is relatively easy to extract. Instead, tritium is radioactive and present in a low quantity in the natural environment. In addition there are problems related to tritium transport. For this reason several methods have been studied to produce tritium on site. The main process under investigation consists in the use of the lithium-neutron interactions; this process is known as "Tritium breeding" [16].

1.1.2 Energy balance and Lawson criterion

To achieve controlled thermonuclear fusion in the laboratory, which provides a positive energy balance, it is necessary to heat the plasma to extremely high temperatures (around 100 million degrees, more than six times the temperature inside the Sun), while confining it to a limited space for a sufficient amount of time. This allows the energy released from fusion reactions to offset both the losses and the energy used to produce it, resulting in:

$$Q = \frac{P_{fusion}}{P_{external}} > 1 \tag{1.2}$$

where Q is the power gain, P_{fusion} is the fusion reactions power and $P_{external}$ the external power. The constraint in (1.2) represents the situation where the power supplied by the fusion reactions is enough on its own to compensate losses and where the external power can thus be switched off. This corresponds to an infinite Q amplification factor ($P_{external} = 0$). The plasma is thus self-maintained like a candle, which, once it has been ignited by a match (external power), carries on fuelling itself. Properly, it is necessary to satisfy the conditions expressed by the *Lawson Criterion* which depends on the plasma temperature T:

$$nT\tau_E > 3 \cdot 10^{21} m^{-3} keV s \tag{1.3}$$

where τ_E is the energy confinement time of particles and is defined as:

$$\tau_E = \frac{W}{P_{losses}} \tag{1.4}$$

where W is the plasma energy and n the plasma density.

In order to maximize the reaction rate (number of reactions per second per unit volume) $R = n_1 n_2 < \sigma\nu >$, the following relationship should apply:

$$n_1 = n_2 = n \tag{1.5}$$

where $_1$ and n_2 are reactant densities. For a 150 million degree D–T plasma, (about 10 KeV energy) and with low impurity content, the product $n\tau_E$ must be greater than $3 \cdot 10^{20} m^{-3} s$. In magnetic confinement devices, the goal is to achieve high confinement times while also preventing particles from impacting against the vacuum chamber with a number of negative consequences such as cooling of the plasma, heating of the machine walls, and introduction of impurities into the plasma itself. It is worth pointing out that Lawson's criterion as presented is derived from an initial power budget that does not take into account the boundary consumption required to power all the systems in a reactor; therefore, a more accurate ignition condition is used in

prototype machines, and Lawson's criterion provides only indicative data on the operating conditions of a controlled thermonuclear fusion machine.

1.2 The Tokamak

The Tokamak, soviet acronym for (TOroidal KAmara MAgnitic Katushka) is a device which uses a powerful magnetic field to confine plasma in the shape of a torus (Fig 1.5). This configuration was proposed in the 1950s by Russian researchers [17]. In order to maintain the fusion process, particles from the hot plasma must be confined in the central region, or the plasma will rapidly cool. Tokamaks exploit the fact that charged particles in a magnetic field experience a Lorentz force and follow helical paths along the field lines (Fig 1.5) [6].

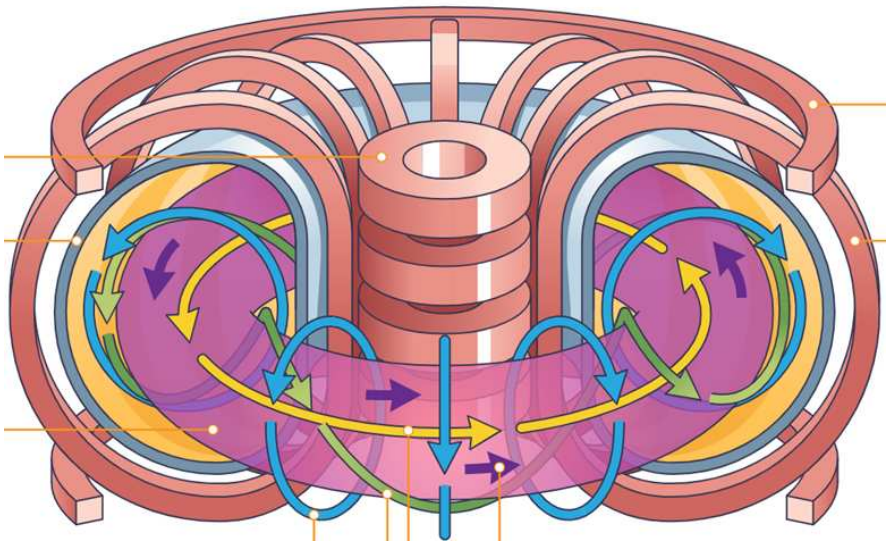

Figure 1.5: 3D sketch of tokamak sources (red), plasma (pink) and field lines: poloidal field lines (blue vertical circles), toroidal (yellow horizontal circle), and their combination, producing a three-dimensional curve (green helix) in which the plasma is highly confined.

Tokamaks include the following main components: i) a vacuum system, based on an integrated Vacuum Vessel with the first wall and a suction system [18]; ii) a blanket system for neutron moderation and, if feasible, on-site tritium breeding from lithium [16]; iii) an additional heating system, based on antennas and Neutral-beam injection (NBI) [19]; iv) a complex magnetic system, whose main characteristics will be illustrated later; v) a diagnostic

system a large array of instruments such as: Magnetic diagnostics, neutron diagnostics, Optical systems, bolometric systems, spectroscopic instruments and microwave diagnostics, to provide the measurements necessary to control, evaluate and optimize plasma performance and to understand plasma physics [20]; vi) a comprehensive system of mechanical supports and auxiliary prevention systems. In Fig. 1.6a a sketch of the ITER tokamak is shown, while in Fig. 1.6b the radial overview of a tokamak layers is sketched.

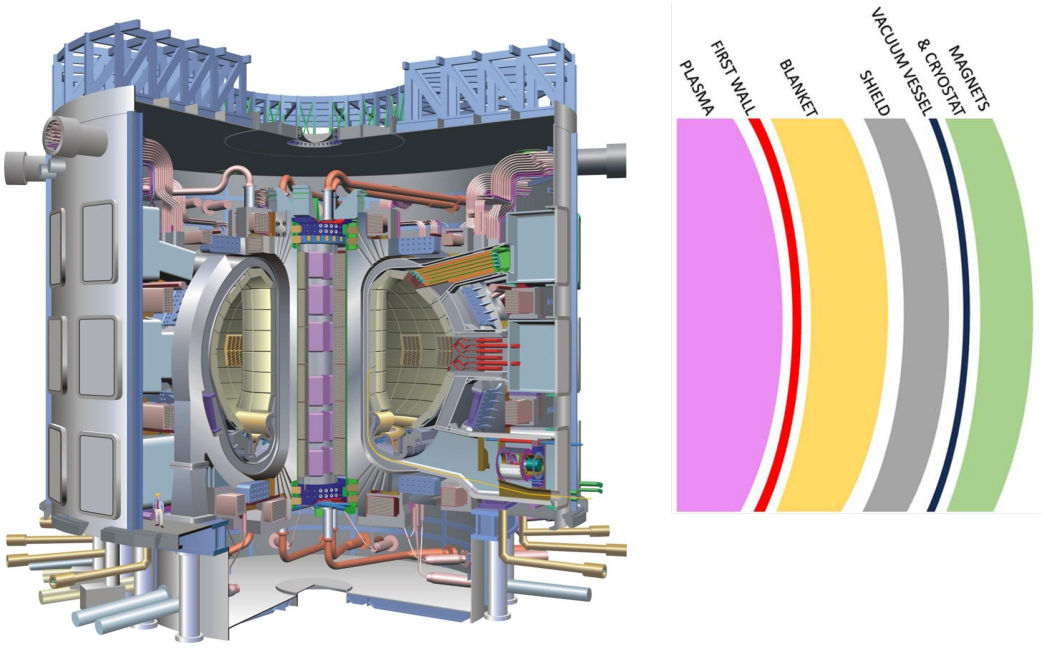

(a) (b)

Figure 1.6: Sketch of the ITER tokamak (a), and a radial overview of a tokamak layers (b).

1.2.1 Magnetic system

Different kind of magnets are used together in order to confine the particles, to induce plasma current and to stabilize and control the plasma. In particular:

1- "D"-shaped toroidal field (TF) magnets (Fig. 1.7a), placed around the vacuum vessel, produce a toroidal magnetic field B_ϕ whose primary function is to confine the plasma particles. It's worth noting that in

2D approximation the following relationship stands:

$$2\pi R B_\phi = \mu_0 I_T \qquad \Rightarrow \qquad B_\phi \propto \frac{1}{R} \tag{1.6}$$

where R is the radial coordinate, I_T the total TF current and μ_0 the vacuum permeability. The number of toroidal coils is chosen appropriately to limit 3D effects (ripple) [21].

2- Poloidal field (PF) magnets (Fig. 1.7b), circular coils used to shape the plasma and contribute to its stability by "pinching" it away from the walls. The shape of the plasma, which depends on the poloidal field, is chosen on the basis of performance optimisation criteria. It should be recalled that external currents are required to confine a plasma (Virial Theorem within electromagnetism), and the PF coils are used to satisfy this requirement [22]. In fact, a toroidal plasma cannot be kept in equilibrium by its currents alone. Equilibrium is maintained, for example, by the poloidal magnetic system, which interacts with the plasma current through its so-called vertical component to produce a suitable centripetal force that allows equilibrium at the desired position in the chamber.

3- Central Solenoid (CS) magnets (Fig. 1.7c), represent the "backbone" of the magnet system, located in the centre of tokamak torus, in the "donut hole". CS allows a powerful current to be induced in the plasma, by transformatory effect, and maintained during long plasma pulses. As the CS produces a strong magnetic field, it is subject to large electromagnetic forces that try to tear the solenoid apart. Coils of solenoid are therefore usually placed in some kind of support structure that holds them in position during a pulse.

4- Error Field Correction Coils (EFCCs) (Fig. 1.7d), generally inserted between the TF and PF coils, are non-asymmetric saddle-shaped coils used to compensate for field errors caused by geometrical deviations due to manufacturing and assembly tolerances and to control the instabilities (ELM mitigation or suppression) [23].

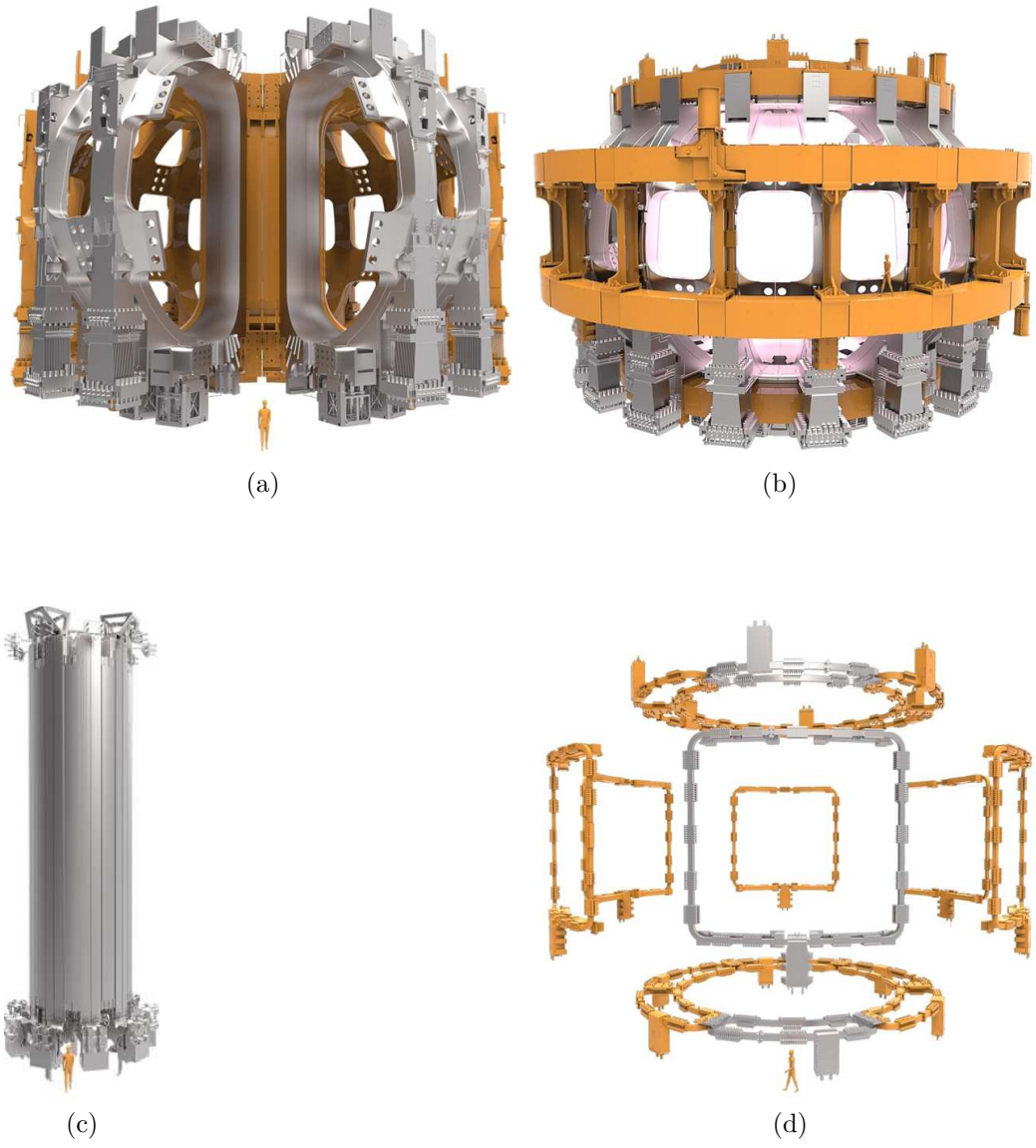

(a) (b)

(c) (d)

Figure 1.7: Sketch of the ITER: a) TF, b) PF, c) CS and d) EFCC magnets.

1.2.2 The safety factor

In magnetic confinement devices, the helical shape of the field lines can be described by the *rotational transform* t [24]:

$$t = \lim_{N\to\infty} \sum_{n=1}^{N} \Delta\theta_n \tag{1.7}$$

where $\Delta\theta_n$ is the poloidal angle made by the field line after n toroidal turns. In tokamak research, the quantity $q = \frac{2\pi}{t}$, called *safety factor*, is preferred. The basic magnetic field configuration consists of toroidally nested flux surfaces (Fig 1.8), while each flux surface is characterised by a certain value of the rotational transform or safety factor q.

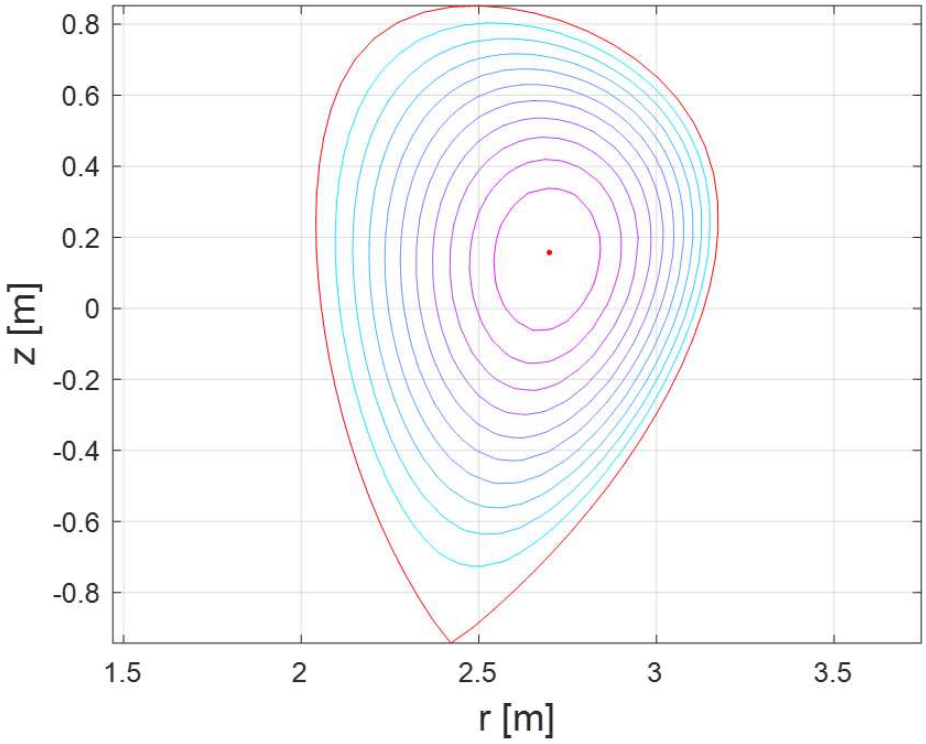

Figure 1.8: Example of nested flux surface.

In a roughly circular tokamak, the equation of a field line on the flux surface is approximately:

$$\frac{rd\theta}{B_\theta} = \frac{Rd\varphi}{B_\varphi} \tag{1.8}$$

where ϕ and θ are the toroidal and poloidal angles, respectively. Thus $q = m/n = \langle d\varphi/d\theta \rangle$ can be approximated by:

$$q \simeq \frac{rB_\varphi}{RB_\theta} \tag{1.9}$$

where the poloidal magnetic field B_θ is mostly produced by a toroidal plasma current. The term "safety" refers to the resulting stability of the plasma; Field lines that rotate poloidally around the torus about q times as toroidally

are inherently less susceptible to certain instabilities. Generally, if $q \leq 2$ at the last closed flux surface (the plasma edge), the plasma is magnetohydrodynamically unstable. In tokamaks with a divertor configuration [25] q approaches infinity at the separatrix, so it is more useful to consider q just inside the separatrix. It is customary to use q at the 95% flux surface (the flux surface that encloses 95% of the poloidal flux), q_{95}.

1.2.3 DTT and DEMO: role in the road-map for the commercial reactors

Despite the progress in research, the goal of producing more energy than that supplied as plasma input, and making the reaction self-sustaining, has not yet been achieved. The results achieved so far by the triple product $nT\tau_E$, in an effort to obey Lawson's criterion are shown in Fig. 1.9.

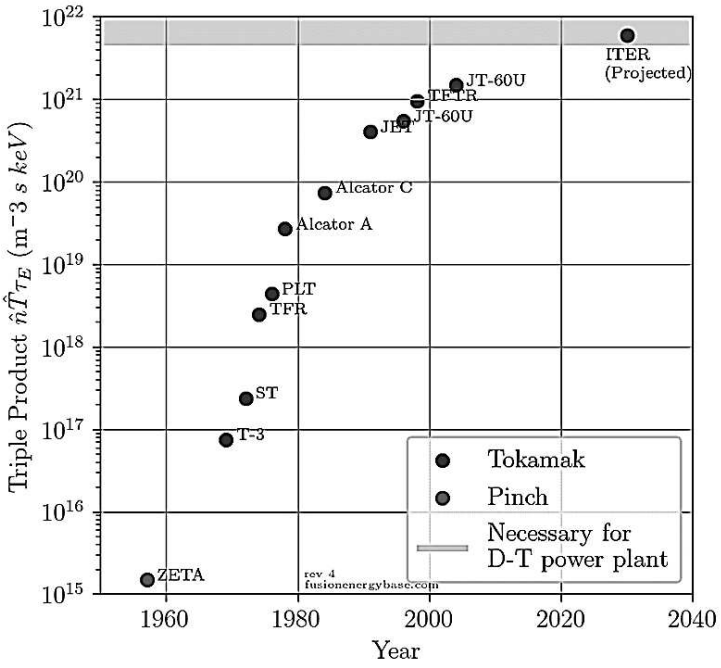

Figure 1.9: Triple product behaviour from 1955 to 2040 (prospect).

The conventional approach for increasing in the fusion gain Q requires to scale up the reactor size. Larger reactors would have to be built to achieve the desired conditions, compared to those still operating in laboratories today. For this purpose, due to costs incompatible with budgetary constraints, and to the real technological possibilities of a single nation, strong international cooperation has increasingly materialized.

Currently the tokamaks are close to the break-even condition (Q=1). The JET tokamak, Joint European Torus, whose realization dates back to 1978, to date holds the record of gain $Q \approx 0.6$. A second specific example is the Japanese JT-60, which holds the record for the highest fusion triple product value of any machine to date, achieved in 2018. The next-step tokamak will be ITER (an acronym for International Thermonuclear Experimental Reactor), whose realization is currently underway in the south of France thanks to the collaboration, since the project's inception in 1985, of Europe, United States, South Korea, China, Japan, Russia and India. ITER will have the daunting task of demonstrating the technical and technological feasibility of a thermonuclear fusion reaction and thus open the door wide for the realization of the first DEMO demonstration reactor prototype, capable of feeding electricity into the public grid.

DEMO must demonstrate the technologies required not only to control a more powerful plasma than exists today, but also to generate electricity safely and consistently, and to maintain the plant regularly, quickly and reliably. The design of such a plant must take account, not just of physics requirements, but also of engineering and technological limitations. Most of the ITER partners have plans for their own DEMO-class reactors. The most well-known and documented DEMO-class reactor design is the European DEMO. On 9 October 2014 EUROfusion [26], the European Consortium for the Development of Fusion Energy, was born. Presently EUROfusion supports and funds fusion research activities on behalf of the European Commission's Euratom programme within 26 EU member states, while Switzerland, Norway and the United Kingdom participate in the activities with their national fusion budgets. Building and operating DEMO, which will hook fusion electricity to the grid, is the subject of the last phase of the EUROfusion Roadmap. The central requirements for DEMO lie in its capability to generate between 300 Megawatt to 500 Megawatt net electricity to the grid and to operate with a closed fuel-cycle, meaning spent tritium fuel will be reprocessed. The Fusion Technology team is looking at requirements that will lay the foundation for a robust conceptual design:

- Selecting the right breeding blanket. Blankets are the internal components of the reactor wall that absorb the energy from the fusion reaction, ensure the tritium breeding process and shield the components outside the reaction chamber from the fast fusion neutrons.

- Selecting the right design for the first-wall, the innermost lining of the reactor wall. Its integration into the blanket must take into account that the first-wall might see higher heat loads than assumed in experimental settings.

- Selecting the minimum pulse duration of DEMO and of the corresponding mix of plasma heating systems.

- Designing in a way that all maintenance work can be carried out remotely via manipulators.

- Incorporating nuclear safety issues from the very beginning of conception.

- Selecting the right divertor concept (described below).

The power released in the form of alpha particles by fusion reactions in the core of the tokamak is transported down to an actively cooled component (the divertor) where it is extracted. The heat flux on the divertor could be very large, reaching values around $60 MW/m^2$, which is the same order of magnitude as the heat flux at the surface of the Sun! The divertor has to withstand harsh conditions and is one of the most critical components of a fusion system. A solution for the divertor has been investigated in present experiments and will be implemented in ITER. However, it is unclear at the moment if the solution implemented in ITER can be extrapolated to future power plants, since the amount of fusion power density released in a reactor will be much larger than in ITER.

A dedicated facility to address these challenges was pointed out first back in 2012, when EFDA, the European Fusion Development Agreement, published the "European Fusion Roadmap". The Divertor Tokamak Test (DTT) project was born.

DTT is a tokamak designed to accommodate a variety of divertor configurations, both in single and double null scenarios, in regimes where core and edge are in conditions of reactor-relevant power flow. The main DTT features are: 6T on-axis at R=2.19 m maximum toroidal magnetic field and plasma current up to 5.5 MA in pulses with total duration up to 100s. The D-shaped vacuum chamber is able to host a plasma with major radius R=2.19 m, minor radius a=0.70 m and average triangularity 0.3. The auxiliary heating power coupled to the plasma at maximum performance is 45 MW, which allows matching ITER and DEMO P_{SEP}/R values, where P_{SEP} is the power flowing through the last closed magnetic surface [27]. DTT sketch is shown in Fig. 1.10, while the main features are reported in Tab. 1.1 together with other tokamaks.

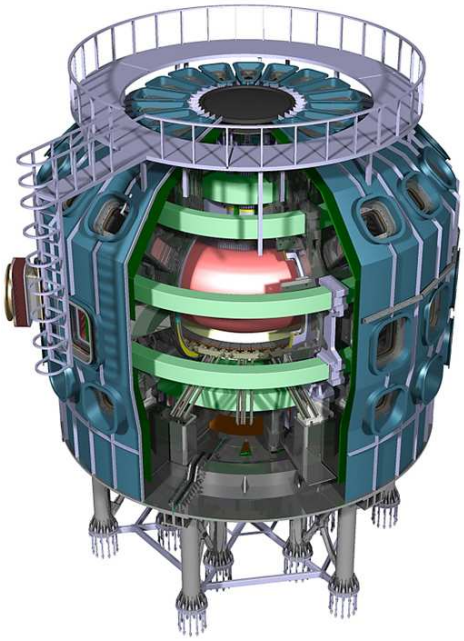

Figure 1.10: DTT project proposal.

Parameter	**DTT**	**JT60SA**	**JET**	**ITER**	**DEMO**
R [m]	2.19	2.96	2.98	6.2	8,2 - 13,1
a [m]	0.70	1.18	0.22	2.0	6,10 - 9,55
B_t **[T]**	6.0	2.25	3.2	5.3	5,6 - 7,0
I_p**[MA]**	5.5	5.5	3.5	15	18 - 20

Table 1.1: Main DTT parameters and comparison with other machines.

However, recent studies have shown that for steady state tokamaks operating at fixed fractions of the density and beta limits, the fusion gain Q, depends mainly on the absolute level of the fusion power and the energy confinement, and only weakly on the device size [28]. In addition, recent progress on the High Temperature Superconducting (HTS) magnets could make compact fusion possible. Private company, such as Tokamak Energy, announced the development of a superconducting compact spherical tokamak called Demo4 in the 2030s [29]. The outcome of these initiatives is uncertain, but a robust partnership between public and private entities in the scientific community could significantly impact the path towards constructing the initial commercially viable fusion reactor. In Fig. 1.11 a high-level schematic of a generic D–T fusion system for electrical energy production, using a conventional thermal conversion cycle approach, is shown.

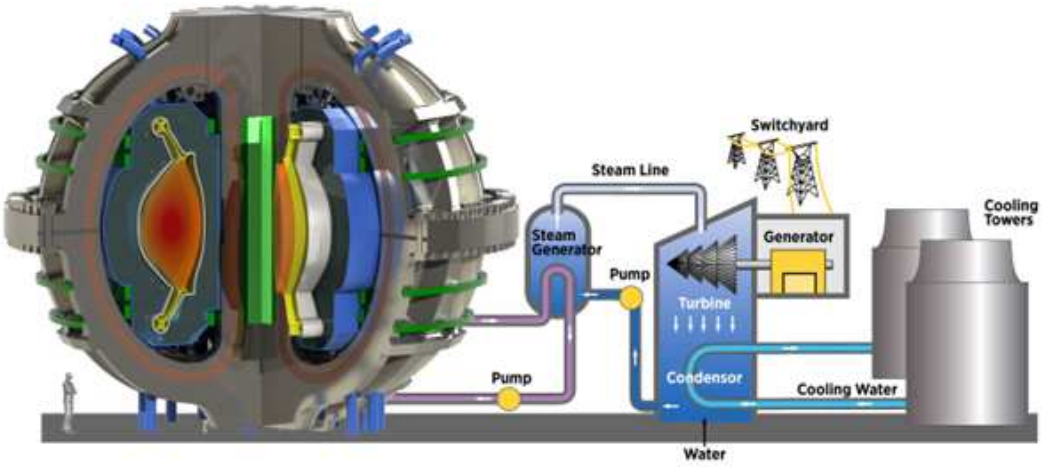

Figure 1.11: Schematic of a generic D–T fusion system for electrical energy production.

Bibliography

[1] Bolch, W. E. (2000). Introduction to Nuclear Concepts for Engineers. Health Physics, 78(1), 102-103.

[2] I. Asimov, (1984). Asimov's New Guide to Science. New York: Basic Books. ISBN 0-465-00473-3.

[3] World-nuclear website, https://world-nuclear.org/information-library/current-and-future-generation/nuclear-power-in-the-world-today.aspx

[4] Krane K. S. & Halliday D. (1988). Introductory nuclear physics. Wiley.

[5] Archive website, https://web.archive.org/web/20080303234143

[6] J. Wesson, D.J. Campbell, "Tokamaks", Oxford university press, vol. 149, 2011.

[7] Friedberg, J. (2007) Plasma Physics and Fusion Energy. 1st Edition, Cambridge University Press, Cambridge.

[8] International Energy Agency (IEA) website, http://www.iea.org/

[9] R. D. Hazeltine and J. D. Meiss, Plasma confinement. Courier Corporation, 2003.

[10] J. J. Duderstadt and Gregory A. Moses, Inertial confinement fusion. John Wiley & Sons, 1982.

[11] National Ignition Facility website, https://lasers.llnl.gov/

[12] F. F. Chen and M. D. Smith, Plasma. John Wiley & Sons, 1984.

[13] H. A. B. Bodin and A. A. Newton. "Reversed-field-pinch research," Nuclear fusion, vol. 20, no.10, 1980.

[14] G. Grieger, et al., "Physics optimization of stellarators," Physics of Fluids B: Plasma Physics, vol. 4, no. 7, pp. 2081-2091, 1992.

[15] schoolphysics website, https://www.schoolphysics.co.uk/age16-19/Nuclear%20physics/Nuclear%20energy/text/Nuclear_fusion/index.html

[16] Pereslavtsev, P., Bachmann, C., & Fischer, U. (2016). Neutronic analyses of design issues affecting the tritium breeding performance in different DEMO blanket concepts. Fusion Engineering and Design, 109, 1207-1211.

[17] The JET Team, The JET Project - Design Proposal, Rep. EURJET-R5, CEC, Brussels (1975)

[18] Ioki, K., Johnson, G., Shimizu, K., & Williamson, D. (1995). Design of the ITER vacuum vessel. Fusion engineering and Design, (27), 39-51.

[19] Marcuzzi, D., Agostinetti, P., Dalla Palma, M., Falter, H. D., Heinemann, B., & Riedl, R. (2007). Design of the RF ion source for the ITER NBI. Fusion Engineering and Design, 82(5-14), 798-805.

[20] ITER website, https://www.iter.org/mach/Diagnostics

[21] Albanese, R., Chiariello, A. G., Di Grazia, L. E., Iaiunese, A., Martone, R., Mattei, M., ... & Zumbolo, P. (2023). Three-dimensional evaluation of the connection lengths in a Tokamak. Fusion Engineering and Design, 192, 113622.

[22] Tsutsui, H., Nomura, S., & Shimada, R. (2001). Application of virial theorem to magnetic confinement fusion device. Purazuma, Kaku Yugo Gakkai-Shi, 77(3), 300-308.

[23] Albanese, R., Bolzonella, T., Chiariello, A. G., Cucchiaro, A., Iaiunese, A., Lampasi, A., ... & Zumbolo, P. (2023). Error field and correction coils in DTT: A preliminary analysis. Fusion Engineering and Design, 189, 113437.

[24] Chen, F. F. (2016) Introduction to Plasma Physics and Controlled Fusion, 3rd Ed., Los Angeles, CA, Springer.

[25] Janeschitz, G., Borrass, K., Federici, G., Igitkhanov, Y., Kukushkin, A., Pacher, H. D., ... & Sugihara, M. (1995). The ITER divertor concept. Journal of Nuclear Materials, 220, 73-88.

[26] EUROfusion website, https://euro-fusion.org/

[27] DTT website, https://www.dtt-project.it/

[28] Costley, A. E., Hugill, J., & Buxton, P. F. (2015). On the power and size of tokamak fusion pilot plants and reactors. Nuclear Fusion, 55(3), 033001.

[29] Tokamak Energy website, https://www.tokamakenergy.co.uk/

2
Error fields

Inevitable inaccuracies in both manufacturing and assembly of magnetic field coils in a tokamak cause discrepancies between actual and nominal field in the plasma region called Error Fields (EFs), and their limitation is needed. A methodology based on the first order truncated Taylor expansion able to flexibly model these deformations and to estimate the EFs is here shown. A vacuum (no plasma response) figure of merit to quantify EFs is also presented together with the procedure for calculating a set of currents needed for an active correction action. The main contribution of the candidate is highlighted in Section 2.4.

2.1 Error fields in a Tokamak

A magnetic field map with prescribed specifications is necessary for the plasma confinement in a fusion device. In an ideal tokamak, the magnetic field should be basically axisymmetric (independence of the toroidal angle), so that the helical magnetic field lines remain on the same magnetic surface as they transit the torus [1][2]. Deviations from nominal magnetic field map, due to external perturbations, are known in literature as Error Fields (EFs) [1][3]. Inaccuracies and tolerances in manufacturing and assembly of magnets, joints, current feeds, or non-axially symmetric parts, are examples of EFs sources. When they exceed a certain critical level, the trajectory of magnetic field lines is altered and "magnetic islands" are created. Islands always degrade confinement of energy, particles, and toroidal angular momentum.

The most observable effects of EFs on tokamaks are quasi-stationary modes (QSM's), which are slowly rotating magnetic islands, and locked modes, which are non-rotating magnetic islands. In JET QSM's are found to almost invariably precede disruptions, predominately n=1. The modes have been observed to lock (stop rotation) and later unlock within the same shot [4][5]. Large amplitude QSM's affect the amplitude and shape of saw-teeth, flatten the electron temperature profile around the rational flux surface, slow down or stop the plasma rotation, and can cause significant degradation of the energy confinement. Locked modes have also been studied on DIII-D[6], Compass-C [7], and other tokamaks [8] [9] and reversed field pinches [10] [11]. To prevent these phenomena, the EFs should be firstly correctly quantified and secondly reduced below a specific threshold. A suitable active correction system, called "Error Field Correction Coil" (EFCC) system, is designed to reach the second purpose. Essentially the correction coils are used to generate an EFs that is, as much as possible, "equal and opposite" to the actual one. An example of EFCC system is shown in Fig. 2.1.

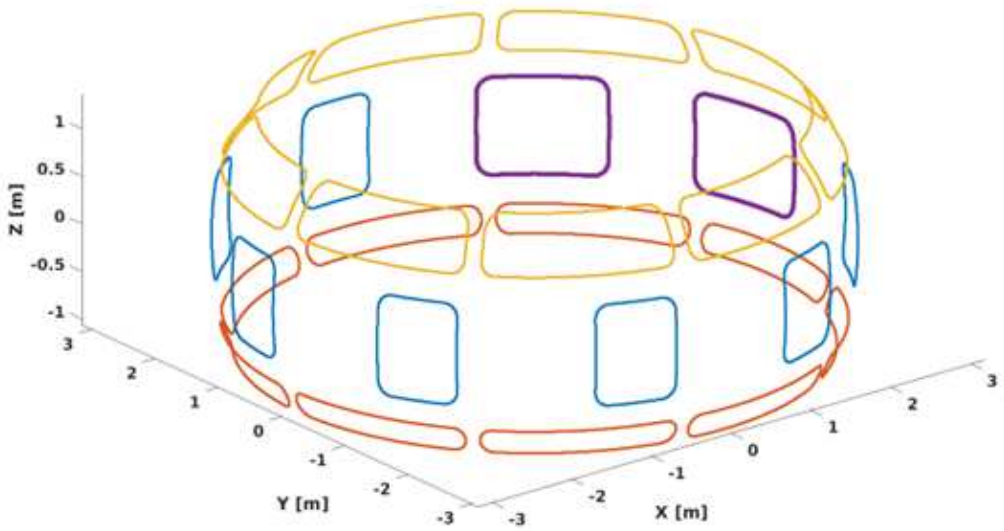

Figure 2.1: Perspective view of the three window-pane coil sets. The correction system shown have nine coils per coil set.

2.2 Vacuum response: Three Modes Error Index

A commonly used performance index to describe the quality of the field mapping while ignoring the plasma response is a weighted quadratic average of the amplitudes of the first three poloidal modes of the error field, defined as the normal component of the difference between the actual and nominal fields, evaluated on a specific plasma surface, called the "Three Modes Error Index" ($TMEI$).[12]:

$$TMEI = \frac{\sqrt{0.2\|\tilde{B}_{1,1}\|_2 + \|\tilde{B}_{1,2}\|_2 + 0.8\|\tilde{B}_{1,3}\|_2}}{B_{tor}} \tag{2.1}$$

where B_{tor} is the unperturbed toroidal field on the magnetic axis of the device [13][14], while $\tilde{B}_{1,1}, \tilde{B}_{1,2}$ and $\tilde{B}_{1,3}$ are the spectral components of 3D complex Fourier space [15] defined as:

$$\tilde{B}_{n,m} = \frac{1}{2\pi^2} \oiint B_N(\theta,\varphi) e^{-i(n\varphi - m\widetilde{\theta})} d\widetilde{\theta} d\varphi \tag{2.2}$$

with $m = 1, 2, 3$ spectral components, just $n = 1$ toroidal spectral component and $B_N(\theta,\varphi)$ the normal component of the field to the q=2 surface, θ, φ the angular coordinates of a quasi-toroidal (ρ, θ, φ) coordinate system, and $\widetilde{\theta}$ the angular curvilinear abscissa [16], defined as:

$$\widetilde{\theta}(l) = \frac{1}{q} \int_0^l \frac{B_t}{r B_p} dl \tag{2.3}$$

where l is the length of the unperturbed field line projected on the poloidal section and B_t and B_p are the toroidal and poloidal components of the unperturbed field on the q=2 surface.

The estimation of EFs is strictly related to the specific scenario instant because the q=2 surface is needed. An electromagnetic code, able to compute the field due to deformed coils is used for the computation of the harmonics used in the TMEI.

2.3 A flexible magnet description: MISTIC

In the frame of 3D fields computation, a critical issue is the mathematical modeling of magnetic field sources, including currents and magnetic materials, which act in different components of the fusion device and may have different shapes. In absence of ferromagnetic materials, it is possible to assume to have the same properties as the vacuum. Therefore, the superposition principle applies and the total magnetic field can be evaluated by summing up the contributes generated by all the known sources. This is a very important hypothesis, because it allows a strong parallelization of the computational burden, by distributing the load on the computational units of a parallel computing system [17][18][19]. A non-commercial code, well known in literature as MISTIC[17], is able to manage the actual (deformed) magnets in linear media, and has been here adopted. The MISTIC code is based on the representation of coils in terms of current filaments, and on the successive decomposition of each filament in a suitable number of current sticks. In this way, the required flexibility and accuracy can be guaranteed just fixing a suitable discretization level. On the other hand, the trade-off between the number of sticks and the computational time must be accurately considered, particularly on standard computing environments, when no parallel speedup is available. In order to extend the computational power, an implementation of MISTIC on High Performance Computing (HPC) architectures, based on dedicated GPU's, has been recently realized and adopted here [17][18][19][20]. The elementary contribution to the field per unit current in a generic field point $\boldsymbol{r}$ is given by [21]:

$$\mathbf{b}_{stick} = \frac{\mu_0}{4\pi} \frac{\mathbf{c} \times \mathbf{a}}{\|\mathbf{c} \times \mathbf{a}\|} \left(\frac{\mathbf{a} \cdot \mathbf{c}}{\|\mathbf{c}\|} - \frac{\mathbf{a} \cdot \mathbf{b}}{\|\mathbf{b}\|} \right) \tag{2.4}$$

where the vector $\mathbf{a}$ has the same length as the stick and the orientation of the current flowing in it,whereas $\mathbf{b}$ and $\mathbf{c}$ are vectors pointing from $\boldsymbol{r}$ to the end-points of the stick as reported in Fig. 2.2.

The MISTIC code, starting from the inputs describing the electric data (the currents in each filament) and the geometric data (the coordinates array of the field points and the coordinates array of the filament points (tails and heads of the sticks)) of the problem, computes all the elementary contributes to the field in (2.4) and hence, sum all these contributes to obtain the Cartesian components of the overall field in a set of desired field points. Consequently, a massive coil can be discretized by means of a number of one-dimensional current segments effectively placed in the volume of interest (Fig. 2.2). The field of the discretized source is the superposition of its

segments' field contributions, and, generally, the higher the discretization, the higher the accuracy. MISTIC has been abundantly assessed and used in the past for many kinds of applications, spacing from the medical purposes to controlled thermonuclear fusion[22][23][12]. Here, the stick approach has been adopted for modelling the coil deformations. An extension of the classical formulation has been developed to flexibly treat the error fields. The basic idea is to take advantage from the linearity of small variations in terms of manufacturing and assembly tolerances of the coils to compute EFs.

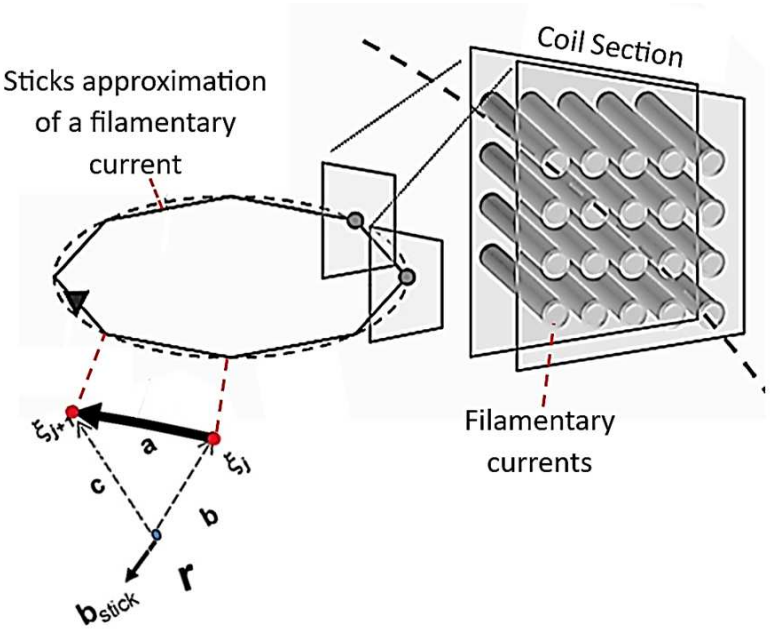

Figure 2.2: Coil discretization using filaments of current.

2.4 Taylor first order model for EFs analysis

In a linear assumption, the magnetic flux density Cartesian component $B_{x0}(\boldsymbol{r})$ (similarly for y and z components) can be described as the superposition of the sources contributions, including magnetic system and plasma:

$$B_{x0}(\boldsymbol{r}) = B_{x0}^{(1)}(\boldsymbol{r}) + B_{x0}^{(2)}(\boldsymbol{r}) + ... + B_{x0}^{(N)}(\boldsymbol{r}) \tag{2.5}$$

where $\boldsymbol{r}$ is the generic field point in $\mathbb{R}^3$ and N the number of sources.

Inaccuracies and tolerances in manufacturing and assembly of tokamak magnets, joints, current feeds, or non-axially symmetric parts act as an additive contribution $\delta B_x(\boldsymbol{r})$, altering the field in (2.5).

The total perturbed field $B_x(\boldsymbol{r})$ can be expressed as:

$$B_x(\boldsymbol{r}) = B_{x0}(\boldsymbol{r}) + \delta B_x(\boldsymbol{r}) \tag{2.6}$$

where $\delta B_x(\boldsymbol{r})$ takes into account of N perturbing contributions corresponding to the deformation of the N sources:

$$\delta B_x(\boldsymbol{r}) = \delta B_x^{(1)}(\boldsymbol{r}) + \delta B_x^{(2)}(\boldsymbol{r}) + ... + \delta B_x^{(N)}(\boldsymbol{r}) \tag{2.7}$$

A basket of perturbation parameters can be selected in order to reproduce the effects of the EFs due to magnets deformations. The deformations of the *i-th* source, then the associated EF, can be related to a suitable set of a finite dimensional space parameters:

$$\underline{\delta p}^{(i)} = [\delta p_1^{(i)}, \delta p_2^{(i)}, \dots \delta p_K^{(i)}] \tag{2.8}$$

where $i = 1, \dots, N$, and K is the dimension of the space.

It should be noted that $\delta B_x^{(i)}(\boldsymbol{r}, \underline{\delta p}^{(i)})$ may depend non-linearly on $\underline{\delta p}^{(i)}$. This could lead to performance problem if, for example, a Monte Carlo analysis has to be performed, as iterative solver are required.

Under the small perturbations hypothesis, the *i-th* term in (2.7) can be expressed as a Taylor series respect to the perturbation parameters [24]. The truncation at first order derivatives provides:

$$\delta B_x^{(i)} \simeq \frac{\partial B_x^{(i)}}{\partial p_1}\delta p_1^{(i)} + \frac{\partial B_x^{(i)}}{\partial p_2}\delta p_2^{(i)} + ... + \frac{\partial B_x^{(i)}}{\partial p_K}\delta p_K^{(i)} \tag{2.9}$$

Each source can be discretized in a finite number of current segments N_{seg} [17][18] as described in previous section. Since the analytical expression (2.4) of the field of each segment depends on the coordinates of its extremes and on its current, the derivatives in (2.9) can be split by using the chain rule:

$$\frac{\partial B_x^{(i)}}{\partial p_k} = \frac{\partial B_x^{(i)}}{\partial x_j}\frac{\partial x_j}{\partial p_k} \tag{2.10}$$

where x_j is the j-th current segment coordinate ($j = 1, \ldots, N_{seg}$). Similarly can be done for y_j and z_j.

A procedure, able to provide perturbed magnetic field (usually the normal component of the perturbed magnetic field on a suitable flux-surface) related to the set of deformation parameters, has been developed for the calculation of analytical electromagnetic and geometric derivatives in the right hand side of (2.10). In a finite dimensional space, combining the expressions in (2.2),(2.9) and (2.10) the relation between the vector of the deformation parameters and the TMEI harmonics can be obtained [24]:

$$\underline{\tilde{B}}_{harms}^{(i)} = \underline{\underline{\widetilde{M}}}^{(i)}\underline{\Delta p}^{(i)} \tag{2.11}$$

where $\underline{\underline{\widetilde{M}}}^{(i)} \in \mathbb{C}^{3\times K}$ is the complex sensitivity matrix of deformations referred to the i-th coil, and K is the number deformation parameters.

Once the set of deformation parameters is defined, the TMEI modes matrices $\underline{\underline{\widetilde{M}}}^{(1)}, \ldots, \underline{\underline{\widetilde{M}}}^{(N)}$ can be stored making the EFs analysis easily executable thanks to the linearity. In Fig (2.3) the block diagram of the coupling between the set of the deformation parameters and the vacuum error field model based on the sticks is shown. The main contribution of the candidate to the work consisted in choosing and treating a basket of deformation parameters and developing the procedure for computing the related sensitivity matrices, then used to characterize of the EFs in a tokamak.

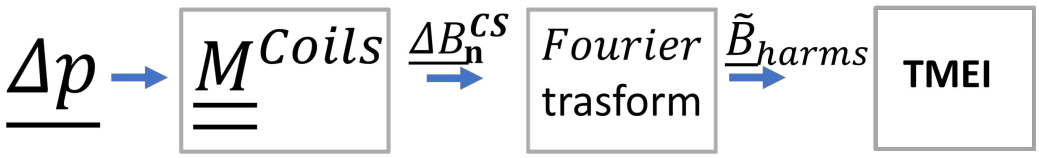

Figure 2.3: Block diagram of the coupling between the set of the deformation parameters and the vacuum error field model.

2.4.1 Assembly and manufacturing inaccuracies of PF, CS and TF coils modelling

Inaccuracies and tolerances in manufacturing and assembly of magnets produce EFs. The generic point $\underline{Q}_j \in \mathbb{R}^3$ of the discretized magnet, which coincides with the head (or the tail) of the *j-th* stick of current can be "perturbed" as:

$$\underline{\tilde{Q}}_j = \tilde{T}(\underline{Q}_j) \tag{2.12}$$

where $\tilde{T}$ is the $\mathbb{R}^3 \rightarrow \mathbb{R}^3$ operator describing the deformation. Assembly inaccuracies of a coil can be described as translations and rotations respect to the axis of a suitable coordinates system. Translations along the specific axis can be modelled just using an additive constant contribute to the coordinates describing the coil geometry, while rotations using Euler's rotation matrices [25].

Here, PF and CS coils system assembly inaccuracies are treated as translations respect to the x, y and z Cartesian directions, and rotations respect to $\widetilde{x}||x$, $\widetilde{y}||y$ and z axes, passing through the coil barycenter (Fig. 2.4). Manufacturing errors are instead implemented both as planar elliptical deformation of the Central Coil Line (CCL), the line passing through the coil section barycenter, and a coil radius perturbation[24]. The coil sections are kept rigid.

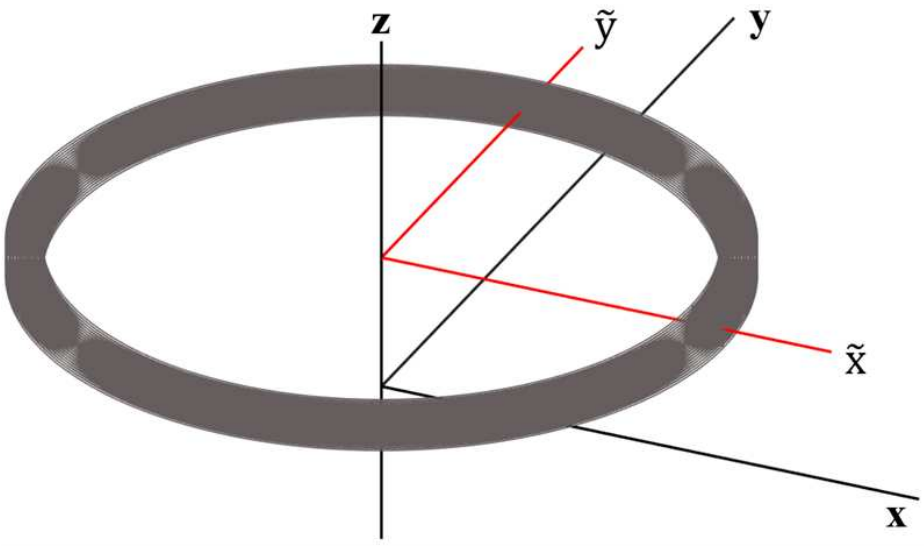

Figure 2.4: PF coil 3D representations along with the axes of the system.

TF coil assembly inaccuracies are implemented similarly to the PF-CS case, are described in a suitable coordinate system $(\widetilde{r}, \widetilde{t}, \widetilde{z})$: where $\widetilde{r} \| r$, $\widetilde{z} \| z$, and $\widetilde{t} = \widetilde{z} \times r$ are centered in the TF barycenter (Fig. 2.5).

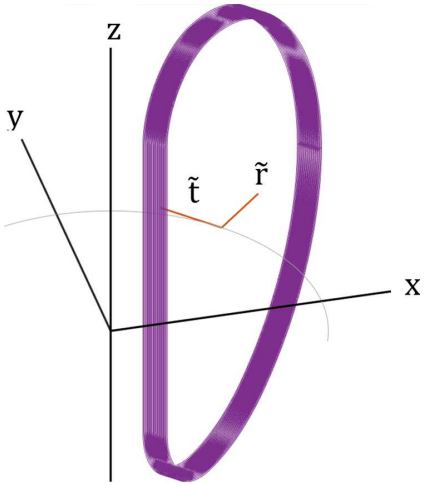

Figure 2.5: TF coil 3D representations along with the axes of the system.

The non-rigid deformations working on TF D-shape, have been implemented using cubic spline interpolation functions [24] controlled in some points along the D-shape (Fig. 2.6) called Control Points. The coil sections are kept rigid.

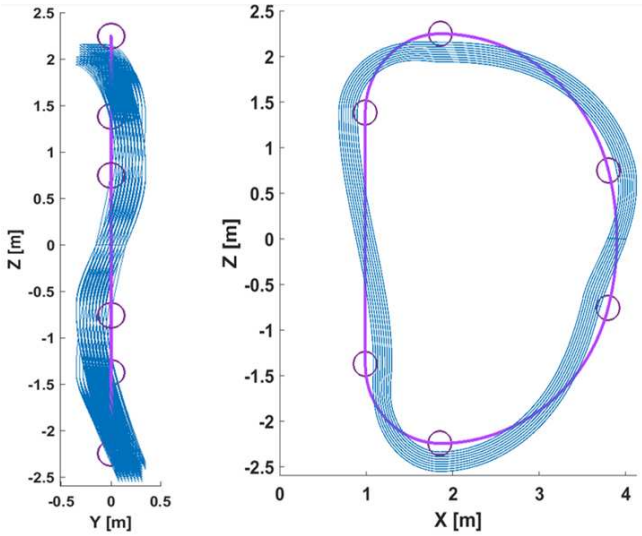

Figure 2.6: TF coil shape and 3D representations of the deformations (blue) and Control Points (pink circles).

The spline function is designed to assign the maximum deformation on the control nodes. The 1D cubic spline expression, depending on the generic curvilinear abscissa t, in the *i-th* interval between two subsequent nodes (with indices i and i-1), is:

$$\begin{aligned} s_3(t) = & \frac{(t_i - t)^3 6\left(\frac{f(t_i)-f(t_{i-1})}{h_i^2}\right) + (t_{i-1} - t)^3 6\left(\frac{f(t_i)-f(t_{i-1})}{h_i^2}\right)}{6h_i} + \dots \\ & + 3\left(\frac{f(t_i) - f(t_{i-1})}{h_i}\right)(t - t_{i-1}) + f(t_{i-1}) - h_i\left(\frac{f(t_i) - f(t_{i-1})}{h_i}\right) \end{aligned} \tag{2.13}$$

where t_i and t_{i-1} are the coordinates of the nodes, $f(t_i)$ and $f(t_{i-1})$ are the respective deformation amplitudes used to control the spline shape, and h_i is the step. In order to manage rigid and non rigid deformations as in (2.10), the geometrical first order derivatives of 2.12 are needed for each kind of deformation. A model of this "linearized" set of deformations has been collected and used for the analysis of EFs.

2.4.2 Stochastic analysis and Correction Action: EFCC currents optimization

In order to correctly characterize the EFs and to allow a reliable design of the EFCCS, usually a reasonable worst case is looked for by means of a Monte Carlo analysis. The linearized model (2.9) is helpful for high performance computation of millions of random cases of deformations, since only matrix multiplications are needed. A distribution of harmonics' values $\underline{\widetilde{B}}^{c}_{harms}$, with c=1,... N_{cases}, can be obtained from (2.11), by randomly varying the vector $\underline{\Delta p} = [\underline{\Delta p}^{(1)}, \underline{\Delta p}^{(2)}, \dots, \underline{\Delta p}^{(N)}]$ within the allowed tolerances for each deformation parameter.

Each examined case $\underline{\widetilde{B}}^{c}_{harms}$ can be used as the input of a EFCCs currents optimization tool solving the system:

$$\underline{\underline{\widetilde{G}}}\ \underline{I_{CC}}^{c} = \underline{\widetilde{B}}^{c}_{harms} \tag{2.14}$$

where $\underline{\underline{\widetilde{G}}}$ is a $\mathbb{C}^{3 \times n_{EFCCs}}$ matrix linking the harmonics for unitary currents and the n_{EFCCs} feeders $\underline{I_{CC}}^{c}$. It is useful rewrite (2.14) in order to split real and imaginary parts of $\underline{B}^{OVF}_{m,n=1}$ obtaining a $6{\times}n_{EFCCs}$. Typically, since $n_{EFCCs} > 6$, then the routine acts on the under-determined system looking for a solution minimizes the maximum EFCCs currents used to reduce the overall EFs below the required threshold. Properly, system in (2.14) is replaced by the minimization of a quadratic function:

$$\min_{\underline{I}_{CC}} \left\{ \frac{1}{2} \left((\underline{I_{CC}}^c)^T \underline{\underline{\widetilde{G}}}^T \underline{\underline{W}}^T \underline{\underline{W}} \underline{\underline{\widetilde{G}}} \underline{I}^c_{CC} \right) - \left(\left((\underline{\widetilde{B}}^c_{harms})^T \underline{\underline{WW}} \underline{\underline{\widetilde{G}}} \right)^T \underline{I}^c_{CC} \right) \right\} \quad (2.15)$$

where $l_b \leq \underline{I_{CC}}^c \leq u_b$, $\underline{\underline{\mathrm{W}}}$ is a suitable regularization matrix and l_b and u_b are vectors with the current limits[24]. The MATLAB® tool quadprog [26] has been used to solve (2.15). Finally, the percentage of corrected cases can be obtained. The candidate's main contribution was to develop the routine for optimising the EFCC currents, then used to reduce the EFs of each case returned by the stochastic analysis.

Bibliography

[1] J. Wesson, D.J. Campbell, "Tokamaks", Oxford university press, vol. 149, 2011.

[2] Friedberg, J. (2007) Plasma Physics and Fusion Energy. 1st Edition, Cambridge University Press, Cambridge. http://dx.doi.org/10.1017/CBO9780511755705

[3] R.J. La Haye, R. Fitzpatrick, T.C. Hender, A.W. Morris, J.T. Scoville, T.N. Todd, Critical error fields for locked mode instability in Tokamaks, Phys. Fluids B 4 (1992) 2098–2103.

[4] J. A. Snipes, D. J. Campbell, P. S. Haynes, T. C. Hender, M. Hugon, P. J. Lomas, N. J. Lopes Cardozo, M. F. F. Nave, and F. C. Sch¨uller, "Large amplitude quasi-stationary MHD modes in JET," Nucl. Fusion, vol. 28, pp. 1085–1097, 1988.

[5] G. M. Fishpool and P. S. Haynes, "Field error instabilities in JET," Nucl. Fusion, vol. 34, pp. 109–119, 1994.

[6] J. T. Scoville, R. J. La Haye, A. G. Kellman, T. H. Osborne, R. D. Stambaugh, E. J. Strait, and T. S. Taylor, "Locked modes in DIII-D and a method for prevention of the low density mode," Nucl. Fusion, vol. 31, pp. 875–890, 1991.

[7] T. C. Hender, R. Fitzpatrick, A. W. Morris, P. G. Carolan, R. D. Durst, T. Edlington, J. Ferreira, S. J. Fielding, S. Haynes, J. Hugill, I. J. Jenkns, R. J. LaHaye, B. J. Parham, D. C. Robinson, T. N. Todd, M. Valovic, and G. H. Vayakis, "Effect of resonant magnetic perturbations on Compass-C tokamak discharges," Nucl. Fusion, vol. 32, pp. 2091–2117, 1992.

[8] H. Ninomiya, K. Itami, Y. Neyatani, O. Naito, R. Yoshino, and the JT-60 Team, "Large m = 3=n = 1 locked mode in JT-60 and its stabilization," Nucl. Fusion, vol. 28, pp. 1275–1281, 1988.

[9] B. P. Van Milligen, A. C. A. P. Van Lammeren, N. J. Lopes Cardozo, F. C. Sch¨uller, and M. Verreck, "Gradients of electron temperature and density across m = 2 magnetic islands in RTP," Nucl. Fusion, vol. 33, pp. 1119–1132, 1993.

[10] A. F. Almagri, S. Assadi, S. C. Prager, J. S. Sarff, and D. W. Kerst, "Locked modes and magnetic field errors in the Madison Symmetric Torus," Phys. Fluids B, vol. 4, pp. 4080–4085, 1992.

[11] P. Greene and S. Robertson, "Locking of kink modes in a reversed-field pinch," Phys. Fluids B, vol. 5, pp. 550–563, 1993.

[12] A. B. Oliva, A. G. Chiariello, A. Formisano, R. Martone, A. Portone, & Testoni, P. (2013). Estimation of error fields from ferromagnetic parts in ITER. Fusion Engineering and Design, 88(9-10), 1576-1580.

[13] J. Knaster et al. (2011). ITER non-axisymmetric error fields induced by its magnet system. Fusion Engineering and Design, 86(6-8), 1053-1056.

[14] A.G. Chiariello et al. (2015). Error Field in Tokamaks: A Plasmaless Measurement Approach.

[15] J.K. Park, A.H. Boozer, & J.E. Menard (2008). Spectral asymmetry due to magnetic coordinates. Physics of Plasmas, 15(6), 064501.

[16] V.D. Pustovitov, (1998). Flux coordinates for tokamaks. Plasma Physics Reports, 24(6), 510-520.

[17] A.G. Chiariello, A. Formisano, R. Martone, "Fast magnetic field computation in fusion technology using GPU technology", Fusion Engineering and Design, 88 (9-10), pp. 1635-1639, 2013

[18] D. B. Kirk and W. H. Wen-mei, Programming massively parallel processors: a handson approach. Newnes, 2012.

[19] F. T. Leighton, Introduction to parallel algorithms and architectures: Arrays · trees · hypercubes. Elsevier, 2014.

[20] A.G. Chiariello et al., "Effectiveness in 3-D magnetic field evaluation of complex magnets" IEEE Transactions on Magnetics, 51 (3), art. no. 7093459, 2015.

[21] H. Haus, J.R. Melcher, Electromagnetic Fields and Energy, Prentice Hall, Upper Saddle River, NJ, 1989.

[22] Formisano, A., & Martone, R. (2019). Different regularization methods for an inverse magnetostatic problem. International Journal of Applied Electromagnetics and Mechanics, 60(S1), S49-S62.

[23] Chiariello, A. G., Formisano, A., & Martone, R. (2015). A high-performance computing procedure for the evaluation of 3D coils inductance. COMPEL: The International Journal for Computation and Mathematics in Electrical and Electronic Engineering, 34(1), 248-260.

[24] Albanese, R., Bolzonella, T., Chiariello, A. G., Cucchiaro, A., Iaiunese, A., Lampasi, A., ... & Zumbolo, P. (2023). Error field and correction coils in DTT: A preliminary analysis. Fusion Engineering and Design, 189, 113437.

[25] Milligan, T. (1999). More applications of Euler rotation angles. IEEE Antennas and Propagation Magazine, 41(4), 78-83.

[26] Gould, N., and P. L. Toint. "Preprocessing for quadratic programming." Mathematical Programming. Series B, Vol. 100, 2004, pp. 95–132.

3

Error fields and linearized plasma response: MARS-F

Non-axisymmetric coil systems on major tokamaks are installed because they provide the opportunity of having ELM-free operation and correcting the error fields. Understanding the plasma response to the applied fields is a crucial issue, since very small non-axisymmetric fields can have surprisingly large consequences. Here, the derivation of the linear MHD equations is presented together with the MARS-F equilibrium code, in order to treat the plasma response to the EFs using the Overlap Field Criterion. The main contribution of the candidate is highlighted in Section 3.4.

3.1 Linearized MHD

THE MHD model allows to study the equilibrium and stability conditions of a plasma, modeled as a conducting fluid interacting with electromagnetic fields[1]. The plasma is viewed as a continuous fluid characterized by distributions of mass density ρ, temperature T, velocity $\mathbf{v}$ related to both electric $\boldsymbol{E}$ and magnetic $\boldsymbol{B}$ field at each point $\boldsymbol{r}$ of space and at each instant t. The model is based on some important assumptions:

- overall neutral plasma, i.e., in case of hydrogen isotopes, $n_e = n_i \equiv n$ (n_e and n_i are the electrons and ions density respectively).
- negligible electron mass, hence $\rho = nm \approx nm_i$, where m and m_i are the average particle mass and ion mass respectively;

- thermodynamic equilibrium, i.e., ions and electrons at same temperature T (isothermy assumption);

- absence of collisions;

- slow, non-relativistic phenomena, so that the displacement current can be neglected($1/\tau << \omega_p$), where τ represents the characteristic time evolution of the quantities and ω_p is the plasma frequency;

From these assumptions, it is possible to obtain the equations that constitute the *MHD model*:

$$\frac{\partial \boldsymbol{B}}{\partial t} = \nabla\times(\mathbf{v}\times\boldsymbol{B}) + \eta\nabla^2\boldsymbol{B} \qquad with \qquad \eta = 1/(\mu_0\sigma) \tag{3.1}$$

$$\rho\frac{D\mathbf{v}}{Dt} = -\nabla p + \frac{1}{\mu_0}(\nabla\times\boldsymbol{B})\times\boldsymbol{B} \tag{3.2}$$

$$\frac{D\rho}{Dt} + \rho\,\nabla\cdot\mathbf{v} = 0 \tag{3.3}$$

$$p = (k_B/m)\rho T \tag{3.4}$$

$$\frac{D}{Dt}\left(\frac{p}{\rho^\gamma}\right) = 0 \tag{3.5}$$

$$\nabla\cdot\boldsymbol{B} = 0 \tag{3.6}$$

where η is the magnetic diffusivity, μ_0 is the vacuum permeability, σ is the electrical conductivity, p is the plasma pressure, k_B is the Boltzmann constant and γ is the adiabatic expansion coefficient.

The assumption of small perturbations allows a first-order derivation of the MHD equations known as the *linearized* MHD, which describes the plasma dynamics around an equilibrium point. The (3.1), (3.2), (3.3), (3.4), (3.5), (3.6) become:

$$\frac{\partial B_1}{\partial t} = \nabla\times(\mathbf{v}_1\times\boldsymbol{B_0}) \tag{3.7}$$

$$\rho\frac{\partial \mathbf{v}_1}{\partial t} = -\nabla p_1 + \frac{1}{\mu_0}(\nabla\times\boldsymbol{B_0})\times\boldsymbol{B_1} + \frac{1}{\mu_0}(\nabla\times\boldsymbol{B_1})\times\boldsymbol{B_0} \tag{3.8}$$

$$\frac{\partial \rho_1}{\partial t} = -\mathbf{v_1}\cdot\nabla\rho_0 - \rho_0\nabla\cdot\mathbf{v_1} \tag{3.9}$$

$$\frac{\partial p_1}{\partial t} = -\mathbf{v}_1 \cdot \nabla p_0 - \gamma p_0 \nabla \cdot \mathbf{v}_1 \tag{3.10}$$

where each variable is described as the sum of a contribution to equilibrium (with subscript 0 to indicate zero order) and one due to small perturbations (with subscript 1 to indicate order 1).

Introducing the displacement vector $\boldsymbol{\xi}(\boldsymbol{r_0}, t)$, such that:

$$\boldsymbol{r} = \boldsymbol{r_0} + \boldsymbol{\xi} \tag{3.11}$$

it follows that:

$$\mathbf{v} = \frac{d\boldsymbol{r}}{dt} = \frac{d\boldsymbol{r_0}}{dt} + \frac{\partial \boldsymbol{\xi}}{\partial t} + (\mathbf{v_1} \cdot \nabla)\boldsymbol{\xi} \tag{3.12}$$

where $\boldsymbol{r}$ is the position vector and $\mathbf{v}$ is the velocity vector. Remembering that $\mathbf{v_0} = \frac{\partial \boldsymbol{r_0}}{\partial t} = 0$ and neglecting second-order terms in the convective derivative, it can be deduced that:

$$\mathbf{v} = \mathbf{v_1} = \frac{\partial \boldsymbol{\xi}}{\partial t} \tag{3.13}$$

Substituting this expression for the velocity into the conservation of mass equation 3.9, yields to the following expression for mass density:

$$\rho_1 = -\boldsymbol{\xi} \cdot \nabla \rho_0 - \rho_0 \nabla \cdot \boldsymbol{\xi} \tag{3.14}$$

In other words, the mass density depends on both a positional change term ($\boldsymbol{\xi}$) and a deformation term ($\nabla \cdot \boldsymbol{\xi}$) of the volume. With similar math on equations (3.7) and (3.10) it is possible to obtain:

$$\boldsymbol{B_1} = \nabla \times (\boldsymbol{\xi} \times \boldsymbol{B_0}) \tag{3.15}$$

$$p_1 = -\boldsymbol{\xi} \cdot \nabla p_0 - \gamma p_0 \nabla \cdot \boldsymbol{\xi} \tag{3.16}$$

Substituting the three results obtained into equation (3.8), we get:

$$\begin{aligned} \rho_0 \frac{\partial^2 \boldsymbol{\xi}}{\partial t^2} = F(\boldsymbol{\xi}) = \nabla(\boldsymbol{\xi} \cdot \nabla p_0 + \gamma p_0 \nabla \cdot \boldsymbol{\xi}) \\ + \frac{1}{\mu_0}\left[(\nabla \times \boldsymbol{B_0}) \times (\nabla \times (\boldsymbol{\xi} \times \boldsymbol{B_0})) + \nabla \times (\nabla \times (\boldsymbol{\xi} \times \boldsymbol{B_0})) \times \boldsymbol{B_0}\right] \end{aligned} \tag{3.17}$$

This equation describes the evolution of the displacement vector $\boldsymbol{\xi}$ for a given equilibrium (p_0, ρ_0, $\boldsymbol{B_0}$).

3.2 MARS-F code overview

The study of plasma responses to external fields such as EFs can be approached in multiple ways, such as treating it as an initial value problem, wherein the system's evolution is observed from an initial unperturbed state, or by adopting a nearby perturbed equilibrium approach. Researchers employ both linear and nonlinear models in these analyses. It's worth noting that the choice of the approach, and sometimes even the same approach, can produce different results [2]. These outcomes are influenced by the physical model used, particularly whether one assumes an ideal or dissipative plasma. In the case of linear models, like the MARS-F code [3], the plasma response can be large, and these models may be inaccurate even when the external field is relatively small. MARS-F solves the linearized MHD (3.7)(3.8)(3.9)(3.10) for three-dimensional perturbations in two-dimensional toroidal geometry. The plasma velocity, the perturbed magnetic field and the pressure are used as unknowns. The code is based on a finite element discretization in the radial direction, and Fourier discretization in the poloidal direction, i.e., as the sum of a finite number of poloidal modes $e^{im\chi}$, where m is the poloidal harmonic number, and χ is the generalised poloidal angle. Fourier expansion is also considered along the toroidal angle ϕ, i.e., considering the term $e^{jn\phi}$ in the basis functions for the n-th toroidal mode number. The plasma response to a given magnetic perturbation on a suitable Coupling Surface (CS) is computed as a plasma response matrix. In the past, MARS-F was effectively integrated with the CARIDDI code [4]. CARIDDI allows a full volumetric three-dimensional description of the conducting structures and a resulting detailed analysis of such instabilities. This integration resulted in the CarMa code, which is designed for investigating plasma MHD instabilities in the presence of 3D eddy currents within the conductive structures of a tokamak [5]. The coupling was performed by assuming that the plasma inertia (and, with it, all Alfven wave-like phenomena) can be neglected on the time scale of interest, which is dictated by the relevant electromagnetic time of the metallic structures. Plasma coupling with the metallic structures has been performed using a suitable surface S. In particular, by adopting the Fourier decomposition in poloidal and toroidal modes, it turns out that each toroidal mode can be associated with a matrix (additively) perturbing the inductance matrix that commonly describes the magnetic coupling of currents in vacuum.

3.3 The Overlap Field Criterion

The general importance of the plasma response for EFs correction was already demonstrated in different tokamaks [6][7][8]. The plasma in fact can both amplify and shield external fields [9][10] and both effects operate in most of the interesting applications, including Resistive Wall Mode (RWM) stability, error field amplification, angular momentum transport, and ELM suppression. The estimation of the linear plasma response to the EFs, based on the Singular Value Decomposition (SVD) technique, has recently been successfully applied to both DIII-D [3] and ITER [11] plasmas. The basic idea is the following. Suppose a stable plasma response to an imposed external vacuum field is the superposition of the response from all stable eigenmodes of the system, for a given toroidal mode number n. In the discrete level (e.g. in the poloidal Fourier space), the response of all the eigenmodes forms a response matrix. The diagonal elements of the SVD of this response matrix indicates the sensitivity of the plasma response to the corresponding eigenvector. In other words, the strongest response from the plasma corresponds to the largest singular value of the $m \times m$ response matrix $\underline{\underline{M}}$, where m is the total number of poloidal harmonics for a given toroidal number n. This strongest response is called Overlap Field (OVF). the SVD eigenvectors, and correcting (i.e. cancelling) the most sensitive component using the EFCC field, a significant reduction of the plasma response to the EF field is expected. The cases $n = 1$ and 2, are generally considered due to their greater impact on plasma performance, but the procedure is applicable to any higher n. The procedure for the computation of the OVF for just n=1 is:

- computation of vacuum magnetic field on the coupling surface due to unit perturbations of coils (sensitivity);
- calculation of (m=-15:15, n=1) 31 harmonics per perturbation;
- calculation of (m=-15:15, n=1) 31 harmonics of vacuum EFCC field;
- multiplication of the vacuum field by the dominant eigenfunction obtaining the OVF.

3.4 Pure electromagnetic model and MARS-F interface matrices coupling

As mentioned before, the CARIDDI code [4] was used in the past, together with the equilibrium code MARS, to take into account the plasma response

and the eddy currents in the conductive structure [5][12][13]. A plasma equilibrium code can be combined with a pure electromagnetic code for EFs plasma response estimation. MARS-F returns the total magnetic field starting from the vacuum normal component of the perturbed field on a suitable coupling surface S_C (fig. 3.1) in input. Therefore, an accurate computation of the perturbed field is needed. The main contribution of the candidate consisted in coupling the pure electromagnetic model in (2.9) and the MARS-F linearized plasma response, for treating EFs in the presence of plasmas.

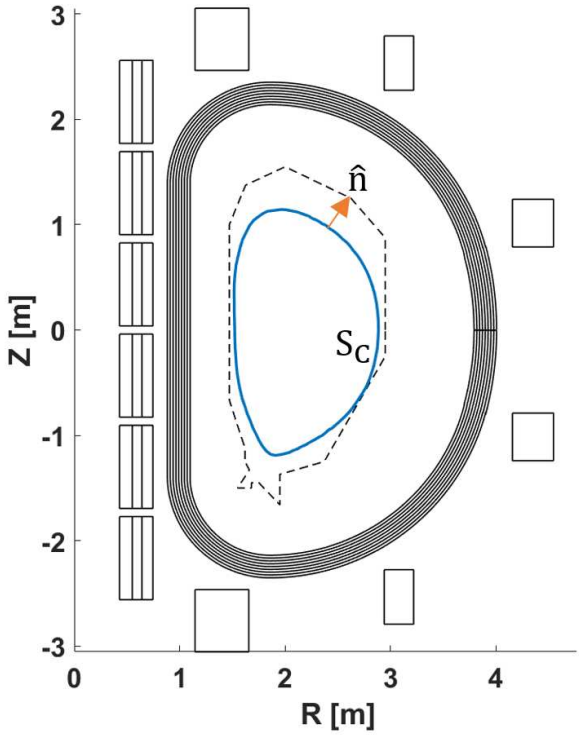

Figure 3.1: Coupling surface points (blue), normal unit vectors $\hat{n}$ (orange arrow) and surrounding magnetic system (CS, PF and TF) (black) sections

The coupling procedure consists in: i) computing the vacuum normal component of the perturbed field ΔB_n^{CS} on S_C with a pure electromagnetic model (such as CARIDDI or the model in (2.9)); ii) projecting ΔB_n^{CS} on a double Fourier space of a finite dimension (θ,ϕ); iii) using the resulting spectrum as input of MARS-F to return the spectrum of the total field (including the plasma response). The the coupling scheme between MARS-F and the vacuum error field model based on the sticks is shown in Fig 3.2.

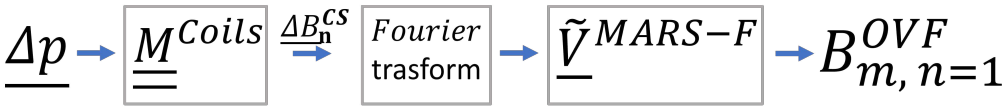

Figure 3.2: Block diagram of the coupling between MARS-F and the vacuum error field model.

where:

- $\underline{\Delta p}$ is the vector collecting the deformation parameters;
- $\underline{\underline{M}}^{Coils}$ is the matrix that links the deformation parameters to the normal component of error field $\underline{\Delta B}_{\mathrm{n}}^{CS}$ on S_C (Fig. 3.3);
- $\underline{\tilde{V}}^{MARS-F}$ is a suitable vector of weights for selecting the dominant singular value to compute the Overlap field $\underline{B}^{OVF}_{m,n=1}$ and m the poloidal harmonic order

It is important to highlight that a suitable discretization of the coils and S_C is needed to reach high accuracy.

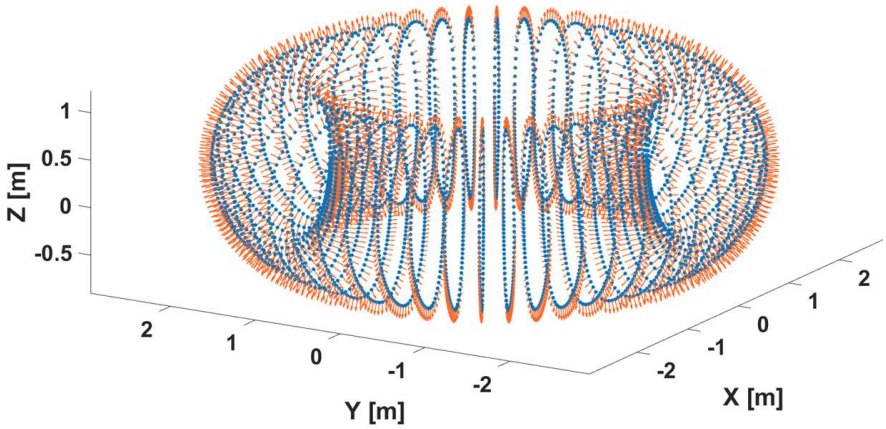

Figure 3.3: Example of a coupling surface points (blue) and normal unit vectors $\hat{n}$ (orange arrows).

A model for the assembly inaccuracies, such as independent rigid displacement and rotations of coils, has been developed and validated for the European DEMO tokamak, and the coupling with MARS-F code has been tested in order to measure the plasma response to this misalignment's (see Chapter 6).

Similarly to (2.14), a reasonable worst case is looked for by means of a Monte Carlo analysis. Each examined case $\underline{B}^{OVF}_{m,n=1}$ can be used as the input of a EFCCs currents optimization tool solving the system:

$$\underline{\underline{\widetilde{G}}}_{OVF} \; \underline{I_{CC}}^{c} = \underline{B}^{OVF}_{m,n=1} \tag{3.18}$$

where, in this case, $\underline{\underline{\widetilde{G}}}_{OVF}$ is a complex vector of n_{EFCCs} elements linking the Overlap field for unit currents and the n_{EFCCs} feeders $\underline{I_{CC}}^{c}$. It is useful rewrite (3.18) in order to split real and imaginary parts of $\underline{B}^{OVF}_{m,n=1}$ obtaining a $2{\times}n_{EFCCs}$. Typically $n_{EFCCs} > 2$, then the routine acts on the underdetermined system looking for a solution minimizes the maximum EFCCs currents used to reduce the overall OVF below the required threshold. System in (3.18) is solved using MATLAB® tool quadprog [14] as an optimization problem. The candidate's main contribution was to readjust, in terms of the OVF, the routine for the EFCC currents optimization in Section 2.4.2, then used to reduce the EFs of each case returned by the stochastic analysis in the presence of plasmas.

Bibliography

[1] Friedberg, J. (2007) Plasma Physics and Fusion Energy. 1st Edition, Cambridge University Press, Cambridge. http://dx.doi.org/10.1017/CBO9780511755705

[2] 7A. D. Turnbull, Nucl. Fusion 52, 054016 (2012).

[3] Park J-K et al 2008 Nucl. Fusion 48 045006

[4] R. Albanese and G. Rubinacci, Integral Formulation for 3D Eddy Current Computation using Edge Elements, IEE Proc 135A (1988), 457–462

[5] Albanese, R., Artaserse, G., Bellizio, T., Rubinacci, G., Fresa, R., Viola, B., ... & Liu, Y. (2010). Coupling plasmas and 3D passive structures in the JET tokamak. International Journal of Applied Electromagnetics and Mechanics, 33(1-2), 533-540.

[6] Park J-K et al 2018 3D field phase-space control in tokamak plasmas Nat. Phys. 14 1223

[7] Fischer R et al 2019 Sawtooth induced q-profile evolution at ASDEX upgrade Nucl. Fusion 59 056010

[8] Callen J D et al 1999 Growth of ideal magnetohydrodynamic modes driven slowly through their instability threshold: applicatio

[9] M. S. Chu, L. L. Lao, M. J. Schaffer, T. E. Evans, E. J. Strait, Y. Q. Liu, M. J. Lanctot, H. Reimerdes, Y. Liu, T. A. Casper, and Y. Gribov, Nucl. Fusion 51, 073036 (2011).

[10] 6M. J. Lanctot, H. Reimerdes, A. M. Garofalo, M. S. Chu, Y. Q. Liu, E. J. Strait, G. L. Jackson, R. J. La Haye, M. Okabayashi, T. H. Osborne, and M. J. Schaffer, Phys. Plasmas 17, 030701 (2010)

[11] Park J-K et al 2011 Nucl. Fusion 51 023003

[12] Portone, A., Villone, F., Liu, Y., Albanese, R., & Rubinacci, G. (2008). Linearly perturbed MHD equilibria and 3D eddy current coupling via the control surface method. Plasma Physics and Controlled Fusion, 50(8), 085004

[13] Albanese, R., & Rubinacci, G. (1988). Integral formulation for 3D eddy-current computation using edge elements. IEE Proceedings A (Physical Science, Measurement and Instrumentation, Management and Education, Reviews), 135(7), 457-462

[14] Gould, N., and P. L. Toint. "Preprocessing for quadratic programming." Mathematical Programming. Series B, Vol. 100, 2004, pp. 95–132.

4

Accurate magnetic field description for a plasma response model

The plasma equilibrium configurations, obtained via standard finite element formulations, as solutions of the Grad-Shafranov equation in terms of poloidal flux using linear triangles, provide the magnetic flux with an accuracy $O(h^2)$. However, the poloidal magnetic field is obtained with a lower accuracy $O(h)$ and is discontinuous across adjacent elements, with consequent problems in the derivation of linearized models for MHD stability analysis. This requires the calculation of terms related to magnetic field derivatives. The method shown here, based on the Helmholtz's theorem, achieves continuity and convergence rate of order $O(h^2)$ for the magnetic field by using three-node linear triangular finite elements. It can be implemented as a post-processor of the magnetic flux solution obtained with linear triangles, in such a way to provide the magnetic field with an accuracy $O(h^2)$. The continuity properties of the magnetic field provide a high level of accuracy and the possibility of deriving reliable linearized models with a limited computational effort. The accuracy is highly reliable for some applications requiring a high precision in the vicinity of magnetic poloidal field null points, like for instance breakdown analysis, or control of the X-point of diverted configurations in a tokamak. The effectiveness of the method is shown in linear and nonlinear cases for which analytical solutions are available. The main contribution of the candidate is highlighted in Section 4.3.

4.1 Grad-Shafranov equation solution guaranteeing the magnetic field continuity

MHD equilibria of 2D axisymmetric plasmas in toroidal nuclear fusion devices are usually obtained by numerically solving the Grad-Shafranov equation in terms of the magnetic poloidal flux. Some numerical codes have been developed using finite element schemes, assuming the magnetic poloidal flux Ψ (or $\psi = \Psi/2\pi$) as basic unknown. In most of them [1][2][3][4][5], the shape functions are in H^1, i.e., square integrable and continuous, with first derivatives square integrable and piecewise continuous. The results obtained with these shape functions are accurate enough for most applications like fixed and free boundary analysis, design of the poloidal field system, simulation of plasma scenarios, design and verification of closed loop magnetic control systems, etc. However, these formulations have the main disadvantage that the value of the magnetic field is not continuous across adjacent mesh elements, and this yields several consequences.

As shown in [6], for linear or nonlinear elliptic problems, monotonicity of the operator and quasi-uniformity of the meshes guarantee that the convergence rate of the solution is $O(h^2)$, i.e. the error approaches zero with the square of the mesh size h. When solving the Grad-Shafranov equation with linear three-node triangular elements, the convergence rate of the poloidal flux is indeed quadratic, i.e., $O(h^2)$. However, the error on the magnetic field is $O(h)$, i.e., approaches zero linearly, since the gradient of the magnetic flux is uniform in each triangle. This fact also implies that the location of the X-point of a diverted configuration, which is a null of the poloidal field, is necessarily approximated by the position of a node of the mesh. Another consequence is that the sensitivity analysis with respect to the position of the magnetic diagnostics is cumbersome. The use of quadratic six-node triangles [2][3] does not yield significant benefits, as the continuity of the field across the elements is not guaranteed. The poor convergence of the magnetic field is not the unique drawback. The derivation of the linearized MHD model for stability analysis [7] calls for the calculation of terms related to the derivatives of the fields, even using variational or weak formulations. This is one of the main reasons why the M3D-C1 code adopts two-dimensional, reduced-quintic triangular finite elements with 18 degrees of freedom in each triangle [8]. JOREK, a non-linear MHD code for tokamak plasmas [9], makes use of 4-vertex elements with 16 degrees of freedom for similar reasons. The formulation introduced here [10] achieves continuity and convergence rate of order $O(h^2)$ for the magnetic field by using three-node linear triangles, based on an extension of the error field approach that dates back to 1981 [11] and

is based on two steps. The first step is the calculation of the poloidal flux. The second step is an application of the procedure proposed in [11] for a more accurate determination of the magnetic field. Furthermore, it should be highlighted that since the method is based on Helmholtz's theorem, the uniqueness of a vector field of whose curl and divergence are known in the domain, is guaranteed if suitable boundary conditions are prescribed.

4.2 Grad-Shafranov equation for the poloidal flux

In a 2D axisymmetric geometry, using a cylindrical coordinate system (r, ϕ, z), the magnetic flux density $\boldsymbol{B}$ and the current density $\boldsymbol{J}$ can be expressed as:

$$\boldsymbol{B} = \nabla\psi \times \frac{\boldsymbol{i}_\phi}{r} + \frac{f}{r}\boldsymbol{i}_\phi \tag{4.1}$$

$$\boldsymbol{J} = \nabla\left(\frac{f}{\mu}\right) \times \frac{\boldsymbol{i}_\phi}{r} + L\boldsymbol{i}_\phi \tag{4.2}$$

where $\boldsymbol{i}_\phi$ is the unit vector in the toroidal direction, μ is the magnetic permeability, f is the poloidal current function, given by the toroidal field multiplied by the radial coordinate $f = rB_\phi$, and:

$$L = -\frac{\partial}{\partial r}\frac{1}{\mu r}\frac{\partial\psi}{\partial r} - \frac{\partial}{\partial z}\frac{1}{\mu r}\frac{\partial\psi}{\partial z} \tag{4.3}$$

which is obtained by (4.1)(4.2) when just Ampere's law along the toroidal direction is considered.

Inside the plasma, a region Ω_p in a poloidal plane rz with the magnetic permeability of the vacuum $\mu = \mu_0$ (Fig. 4.1), the toroidal component of the current density J_ϕ is given by:

$$J_\phi = rp'(\psi) + \frac{ff'(\psi)}{\mu_0 r} \tag{4.4}$$

according to the Grad-Shafranov equation [1][2][3][4][5]:

$$L\psi = rp'(\psi) + \frac{ff'(\psi)}{\mu_0 r} \quad in \quad \Omega_p \tag{4.5}$$

which is an elliptic second order partial differential equation, where the profiles of poloidal current function f and kinetic pressure p are prescribed as functions of the poloidal flux per radian ψ.

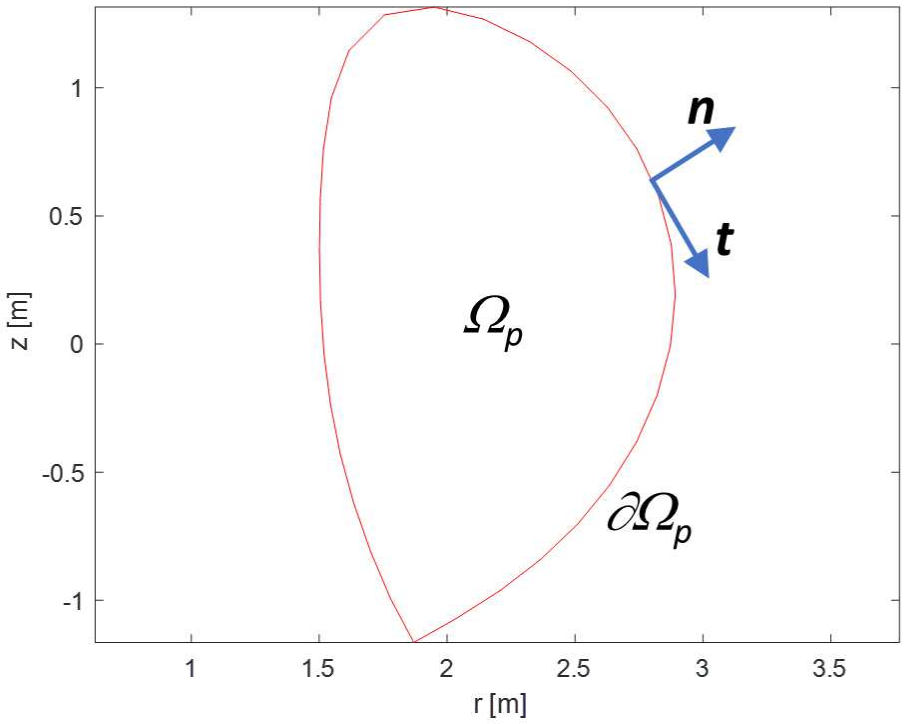

Figure 4.1: Sketch of a plasma region: cross section Ω_p in a poloidal plane rz, showing normal and tangential unit vectors $\boldsymbol{n}$ and $\boldsymbol{t}$ on its boundary $\partial\Omega_p$.

The Grad-Shafranov equation is closed by suitable Dirichlet boundary conditions on $\partial\Omega_p$ if the plasma shape is prescribed:

$$\psi = \psi_b \quad on \quad \partial\Omega_p \tag{4.6}$$

and in this case (4.5) and (4.6) define a boundary value problem, usually denoted as fixed boundary problem. Otherwise, (4.5) has to be coupled to Maxwell's and circuit equations outside the plasma and in this case the formulation is referred to as free boundary problem, being the plasma shape a result of the analysis. Here, for the sake of simplicity, the focus is on problem (4.5)-(4.6), but the method is also applicable to the free boundary case as well. It is worth noticing that problem (4.5)-(4.6) is linear or non-linear, depending on the profiles $p'(\psi)$ and $ff'(\psi)$.

4.3 Field error approach for the calculation of the poloidal flux gradient

Once problem (4.5)-(4.6) is solved in terms of ψ and the poloidal current function is obtained by the profile $f(\psi)$, the calculation of $\boldsymbol{J}$ and $\boldsymbol{B}$ is straightforward from (4.1)-(4.2). This is the standard procedure usually adopted in plasma equilibrium codes. However, as outlined in the introduction, the continuity properties of the magnetic field are not satisfactory for some applications when using first order triangular elements for ψ.

Continuity and $O(h^2)$ convergence rate of ψ are automatically transferred to $p(\psi)$,$f(\psi)$ and hence to $B_\phi = f(\psi)/r$ and to $J_\phi = rp'(\psi) + ff'(\psi)/\mu_0 r$. A dramatic improvement can be achieved by using the approach proposed by [11] for a more accurate calculation of $\boldsymbol{g} = \nabla\psi$ and hence of the poloidal field $B_{pol} = \nabla\psi \times \boldsymbol{i}_\phi/r$.

The poloidal field is solenoidal, hence:

$$\nabla \cdot \boldsymbol{B}_{pol} = 0 \quad in \quad \Omega_p \tag{4.7}$$

Another relationship is obtained by Ampere's law along the toroidal direction:

$$\nabla \times \boldsymbol{B}_{pol} = \mu_0 J_\phi \boldsymbol{i}_\phi \quad in \quad \Omega_p \tag{4.8}$$

Problem (4.7)-(4.8) is closed by the boundary condition:

$$\boldsymbol{n} \cdot \boldsymbol{B}_{pol} = \frac{1}{r}\frac{\partial \psi_b}{\partial t} \quad on \quad \partial\Omega_p \tag{4.9}$$

where $\boldsymbol{n}$ is the unit outward normal vector, $\boldsymbol{t} = \boldsymbol{i}_\phi \times \boldsymbol{n}$ is the unit tangential vector, and $\partial\psi_b/\partial t$ is the tangential derivative of ψ_b, which is zero if $\partial\Omega_p$ is the interface between plasma and vacuum (where ψ_b is constant).

The plasma region is simply connected in the 2D domain Ω_p in the poloidal plane and boundary condition (4.9) is certainly compatible with (4.7). Therefore, according to Helmholtz's theorem, problem (4.7)-(4.9) yields a unique solution for the poloidal field $\boldsymbol{B}_{pol} = \boldsymbol{g} \times \boldsymbol{i}_\phi/r$ and can be reformulated in variational terms as the minimization of an error functional in terms of $\boldsymbol{g} = \nabla\psi$:

$$\begin{aligned} \min \frac{1}{2}\Bigg\{ & \int_{\Omega_p} \left[(\nabla \cdot \boldsymbol{B}_{\mathrm{pol}})^2 + (\nabla \times \boldsymbol{B}_{\mathrm{pol}} - \mu_0 J_\phi \boldsymbol{i}_\phi)^2 \right] r^2 d\Omega \\ & + \int_{\partial\Omega_p} \left[\left(\mathbf{n} \cdot \boldsymbol{B}_{\mathrm{pol}} - \frac{\partial \psi_b}{\partial t}/r \right)^2 \right] r d\Gamma \Bigg\} \end{aligned} \tag{4.10}$$

4.3.1 Finite element procedure

The finite element procedure follows the two steps depicted in the previous section. The first step is the standard finite element solution in terms of poloidal flux per radian ψ using three-node linear triangles [1][2][3][4]. Fig. 4.2 shows an example of mesh of the plasma region Ω_p.

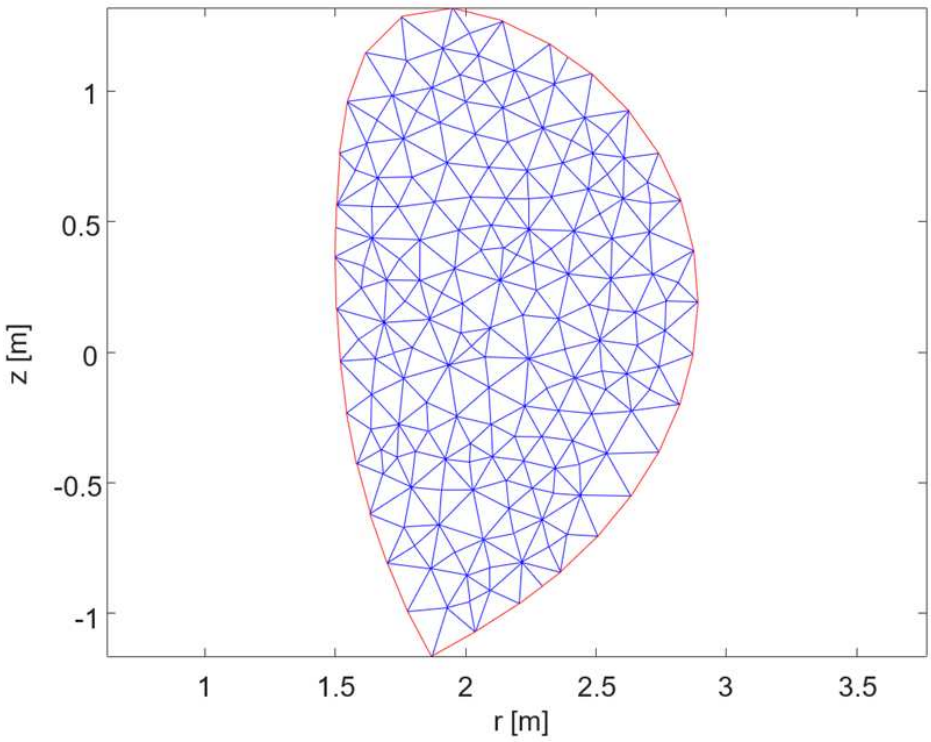

Figure 4.2: Sketch of a plasma region: discretization of Ω_p with linear triangular finite elements.

The second step is an extension of the procedure proposed in [4] for the determination of the vector field $\boldsymbol{g} = \nabla\psi$.

$$\psi(r,z) = \sum_{k}^{N} c_k w_k(r,z) \tag{4.11}$$

where the c_k coefficients are the nodal values, since the generic w_k shape function is 1 at node k and zero at the other nodal points, and N is the total number of nodes. Therefore, the values corresponding to the boundary nodes are directly given by (4.6).

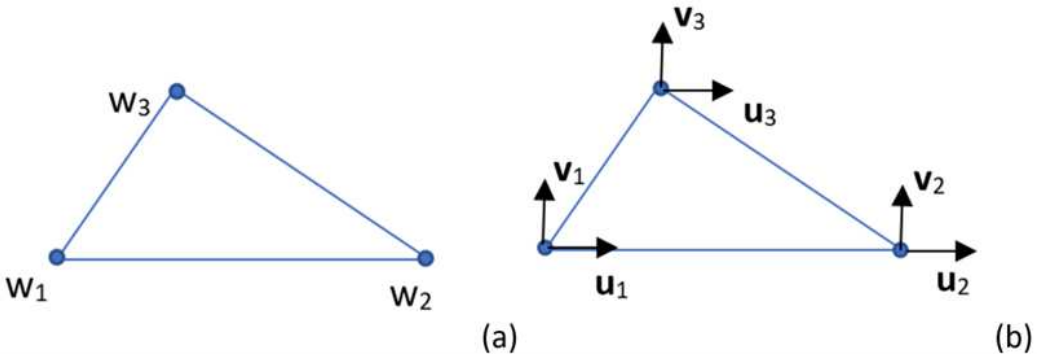

Figure 4.3: Three-node linear triangles: a) three degrees of freedom (scalar shape functions $w1, w2, w3$) for the calculation of the poloidal flux; b) six degrees of freedom for the calculation of $\boldsymbol{g} = \nabla\psi$ (vector shape functions $\boldsymbol{w_1} = \boldsymbol{u_1} = w_1\boldsymbol{i}_r$, $\boldsymbol{w_2} = \boldsymbol{u_2} = w_2\boldsymbol{i}_r$, $\boldsymbol{w_3} = \boldsymbol{u_3} = w_3\boldsymbol{i}_r$, $\boldsymbol{w_4} = \boldsymbol{v_1} = w_1\boldsymbol{i}_z$, $\boldsymbol{w_5} = \boldsymbol{v_2} = w_2\boldsymbol{i}_z$, $\boldsymbol{w_6} = \boldsymbol{v_3} = w_3\boldsymbol{i}_z$, where $\boldsymbol{i}_r$ and $\boldsymbol{i}_z$ are the unit vectors along r and z).

Galerkin weak formulation applied to (4.3), with weight functions coincident with shape functions, yields [12]:

$$\int_{\Omega_p} \frac{\nabla w_i \cdot \nabla\psi}{r} d\Omega = \mu_0 \int_{\Omega_p} w_i \; J_\phi \; d\Omega \tag{4.12}$$

Applying the same approach to (4.5), the values of the coefficients of expansion (4.11) corresponding to the internal nodes are obtained from system:

$$\int_{\Omega_p} \frac{\nabla w_i \cdot \nabla\psi}{r} d\Omega = \int_{\Omega_p} w_i \; [\mu_0 r p'(\psi) + \frac{f f'(\psi)}{r}] d\Omega \tag{4.13}$$

which, for the fixed boundary problem, is linear or nonlinear, depending on the profiles $p'(\psi)$ and $f f'(\psi)$.

4.3.2 Finite element calculation of the magnetic field

This step assumes $\boldsymbol{B}_{pol} = \boldsymbol{g} \times \boldsymbol{u}_\phi / r$, expanding $\boldsymbol{g}$ as a linear combination of vector shape functions $\boldsymbol{w}_k$:

$$\boldsymbol{g}(r,z) = \sum_{k}^{2N} \alpha_k \boldsymbol{w}_k(r,z) \tag{4.14}$$

obtained by using nodal basis functions for its radial and vertical components in three-node linear elements (Fig. 4.3b) where the α_k coefficients are the nodal amplitudes. Minimization of scalar functional (4.10), rewritten in terms of $\boldsymbol{g}$:

$$\min \frac{1}{2}\left\{\int_{\Omega_p}\left(\nabla\times\boldsymbol{g}\right)^2 d\Omega \;+\int_{\Omega_p}\left[\nabla\times(\boldsymbol{g}\times\boldsymbol{i}_\phi)/r-\mu_0 J_\phi \boldsymbol{i}_\phi\right]^2 r^2 d\Omega+\right.$$
$$\left.+\int_{\partial\Omega_p}\left[\left(\boldsymbol{t}\cdot\boldsymbol{g}-\frac{\partial\psi_b}{\partial t}\right)^2/r\right]d\Gamma\right\} \tag{4.15}$$

yields a linear system for the determination of the g_k coefficients:

$$\int_{\Omega_p}\left(\nabla\times\boldsymbol{w}_i\right)\cdot\left(\nabla\times\boldsymbol{g}\right)\,d\Omega\,+$$
$$+\int_{\Omega_p}\left[\nabla\times\left(\frac{\boldsymbol{w}_i\times\boldsymbol{i}_\phi}{r}\right)\right]\cdot\left[\nabla\times(\boldsymbol{g}\cdot\boldsymbol{i}_\phi/r)-\mu_0 J_\phi\boldsymbol{i}_\phi\right]r^2 d\Omega+ \tag{4.16}$$
$$+\int_{\partial\Omega_p}\left(\boldsymbol{t}\cdot\boldsymbol{w}_i\right)\cdot\left(\boldsymbol{t}\cdot\boldsymbol{g}-\frac{\partial\psi_b}{\partial t}\right)/r\,d\Gamma=0$$

The integration is carried out numerically, with a single Gauss point at the element center. As suggested in [6], this does not degrade the accuracy of the solution. The results obtained are shown in the Chapter 6. The candidate's contribution was to develop the post-processing routines based on the Helmholtz's theorem, which return a continuous magnetic field using linear triangular elements.

4.4 Planned activities: EF advanced analysis

The linearized MHD (3.7)(3.8)(3.9)(3.10) requires the continuity of the magnetic field across adjacent elements in order to guarantee the computation of the magnetic field derivatives. The equation for the displacement (3.17) is here recalled for convenience:

$$\rho_0\frac{\partial^2\boldsymbol{\xi}}{\partial t^2}=F(\boldsymbol{\xi})=\nabla(\boldsymbol{\xi}\cdot\nabla p_0+\gamma p_0\nabla\cdot\boldsymbol{\xi})+$$
$$+\frac{1}{\mu_0}\left[(\nabla\times\boldsymbol{B_0})\times\boxed{(\nabla\times(\boldsymbol{\xi}\times\boldsymbol{B_0}))}+\nabla\times\boxed{(\nabla\times(\boldsymbol{\xi}\times\boldsymbol{B_0}))}\times\boldsymbol{B_0}\right] \tag{4.17}$$

The two highlighted terms require the field to be smooth. Nowdays, MHD codes use high degree of polynomial shape functions to guarantee continuity, such M3D-C1 and JOREK[8][13]. The method presented above, achieves continuity and convergence rate of order $O(h^2)$ for the magnetic field by using

three-node linear triangular finite elements; and allows the development of a 3D linearized plasma response model. A brief overview of the approach is here reported.

The problem (4.17) can be closed by a boundary condition:

$$\delta\xi_n \quad \text{on} \quad \partial V_{pl} \tag{4.18}$$

where V_{pl} is the plasma region.

In the Master Thesis titled "Development of a new linearized plasma response model in a tokamak device" [14] a 2D plasma model response to poloidal flux disturbance $\delta\psi_b$ has been faced. For 3D cases, $\delta\psi_b$ can be replaced by the normal component of the field $\delta\mathbf{B}_n$. Here, the main contents of the method are summarized similarly to the 2D case:

1. A disturbance $\delta\mathbf{B}_n$ (or equivalently $\delta\boldsymbol{\xi}_n$), is applied as input.

2. The fixed boundary problem (4.17) is solved using the strategy shown in sections 4.2-4.3 for higher accurate field computation, and $\delta\boldsymbol{\xi}$ is provided in V_{pl}.

3. Using the relation $\delta\mathbf{B}_{pl} = \nabla \times (\delta\boldsymbol{\xi} \times \mathbf{B}_{pl,0})$, the variation of the magnetic field $\delta\mathbf{B}_{pl}$ generated by the plasma is computed in V_{pl}, including the values on ∂V_{pl}, where $\mathbf{B}_{pl,0}$ is the equilibrium magnetic field due to the plasma.

4. On ∂V_{pl}, the contribution of the external disturbance $\delta\mathbf{B}_{n,ext}$ is computed as the difference $\delta\mathbf{B}_{n,ext} = \delta\mathbf{B}_n - \delta\mathbf{B}_{n,pl}$.

5. Finally, the plasma response to a unitary external disturbance can be computed as:
$$\frac{\delta\mathbf{B}_{n,pl}}{\delta\mathbf{B}_{n,ext}} \tag{4.19}$$

The assessment of the previous model for 3D plasma response is planned in the future. The presented model could be a valid alternative to the linear plasma response codes currently used and could provide a more advanced error field analysis.

Bibliography

[1] J. Blum, J. Le Foll, Comput. Phys. Commun. 24 (3–4) (1981) 235–254, https:// doi.org/10.1016/0010-4655(81)90149-1.

[2] R. Albanese, et al., in: 12th Conf. on Numerical Simulation of Plasmas, San Francisco, CA, 1987.

[3] R. Albanese, F. Villone, Nucl. Fusion 38 (5) (1998) 723–738, https://doi.org/10. 1088/0029-5515/38/5/307.

[4] R. Albanese, R. Ambrosino, M. Mattei, Fusion Eng. Des. 96–97 (2015) 664–667, https://doi.org/10.1016/j.fusengdes.2015.06.162.

[5] N. Miki, M. Verrecchia, P. Barabaschi, et al., Fusion Eng. Des. 58–59 (2001) 555–559, https://doi.org/10.1016/S0920-3796(01)00494-X.

[6] A. Abdulle, M.E. Huber, Numer. Methods Partial Differ. Equ. 32 (3) (2016) 955–969, https://doi.org/10.1002/num.22037.

[7] J.P. Freidberg, Rev. Mod. Phys. 54 (3) (1982) 801–902, https://doi.org/10.1103/ RevModPhys.54.801.

[8] S.C. Jardin, J. Comput. Phys. 200 (1) (2004) 133–152, https://doi.org/10.1016/j.jcp.2004.04.004.

[9] M. Hoelzl, et al., Nucl. Fusion 61 (2021) 065001, https://doi.org/10.1088/1741-4326/abf99f.

[10] Albanese, R., Iaiunese, A., & Zumbolo, P. 291 (2023) 108804, https://doi.org/10.1016/j.cpc.2023.108804. Computer Physics Communications, 108804.

[11] P. Neittaanmäki, J. Saranen, Numer. Math. 37 (3) (1981) 333–337, https://doi. org/10.1007/BF01400312.

[12] R. Albanese, R. Fresa, G. Rubinacci, F. Villone, Time evolution of tokamak plasmas in the presence of 3D conducting structures, (2000) IEEE Transactions on Magnetics, 36 (4 I), pp. 1804 - 1807, DOI: 10.1109/20.877795

[13] M. Hoelzl et al., The JOREK non-linear extended MHD code and applications to large-scale instabilities and their control in magnetically confined fusion plasmas, (2021), Nucl. Fusion 61 065001, DOI: 10.1088/1741-4326/abf99f

[14] Marco Neri. Supervisor, Prof. Raffaele Albanese. Co-Supervisors, Ing. Vittorio Di Marzo & Ing. Pasquale Zumbolo, Development of a new linearized plasma response model in a tokamak device. Master thesis, University of Naples, 2023.

5

Parametric analysis and model validation

The characteristic dimensions of a tokamak magnets are in the order of meters, with tolerances in the order of millimeters. Thus, the tool shown in section 2.4, based on first order Taylor approximation, should be validated in order to asses its accuracy to produce a statistical analysis, evaluate the impact on the EFs and optimize the EFCCs currents to counteract them. The assessment has been performed on both DTT and DEMO devices.

5.1 Assessment of the accuracy level of magnetic field

THE analysis aimed at investigating the discretization level of the magnets varying the number of sticks was carried out by comparing the magnetic field calculated analytically (as a reference) with the numerically calculated field using the Biot-Savart law. This comparison was performed using the DTT geometry data, dating back to 2022, reported in Tabs. 5.1, 5.2, 5.3, 5.4 [1][2], feeding the magnets at their maximum current and varying the number of sticks per filament for CSs, PFs and TFs respectively in order to ensure the accuracy about 1μT. In Fig.5.1a and Fig.5.1b two examples of discretization levels of a DTT PF coil are shown.

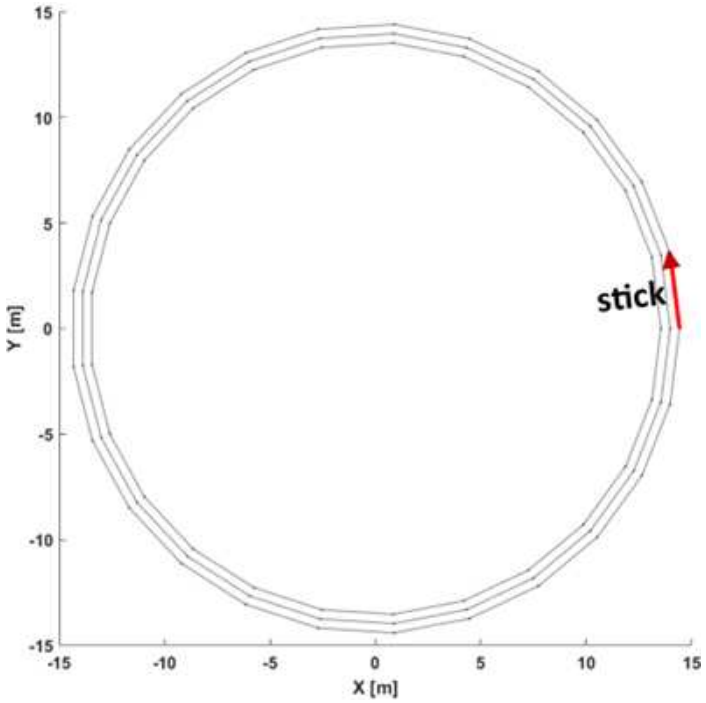

(a)

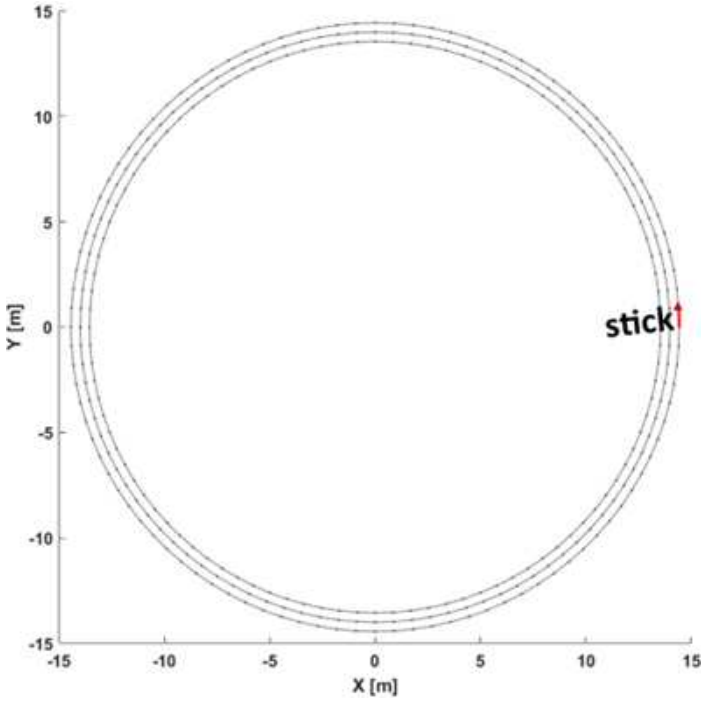

(b)

Figure 5.1: Coarse discretization level (about 20 sticks) (a) and intermediate discretization level (about 200 sticks) (b) of a DTT PF magnet (top view).

Name	R_B **[m]**	Z_B **[m]**	**DR [m]**	**DZ [m]**	**nR**	**nZ**
CS3U-H	0.4896	2.1658	0.1213	0.7880	4	17
CS3U-M	0.5960	2.1658	0.0915	0.7880	4	20
CS3U-L	0.6935	2.1658	0.1035	0.7880	6	24
CS2U-H	0.4896	1.2994	0.1213	0.7880	4	17
CS2U-M	0.5960	1.2994	0.0915	0.7880	4	20
CS2U-L	0.6935	1.2994	0.1035	0.7880	6	24
CS1U-H	0.4896	0.4331	0.1213	0.7880	4	17
CS1U-M	0.5960	0.4331	0.0915	0.7880	4	20
CS1U-L	0.6935	0.4331	0.1035	0.7880	6	24

Table 5.1: DTT CS system geometrical data info adopted.

Name	R_B **[m]**	Z_B **[m]**	**DR [m]**	**DZ [m]**	**nR**	**nZ**
PF1	1.4000	2.7600	0.5100	0.5904	18	20
PF2	3.0795	2.5340	0.2790	0.5168	10	16
PF3	4.3511	1.0150	0.3898	0.4522	14	14
PF4	1.4000	2.7600	0.5100	0.5904	18	20
PF5	3.0795	2.5340	0.2790	0.5168	10	16
PF6	4.3511	1.0150	0.3898	0.4522	14	14

Table 5.2: DTT PF system geometrical data info adopted.

Nodes	**R nodes [m]**	**Z nodes [m]**
B'	1.8606	-2.2113
A'	1.0422	-1.3929
E	1.0422	0
A	1.0422	1.3754
B	1.8606	2.1939
C	3.7962	0.6738
D	3.8732	0
D'	3.7821	-0.7456
C'	2.8609	-1.9533

Table 5.3: R-Z control points coordinates for the DTT TF D-shape (see Fig. 5.2).

Centers	R [m]	Z [m]	Rays [m]
O1	1.8606	-1.3929	0.8184
O2	1.8606	1.3755	0.8184
O3	1.8784	0.2241	1.9698
O4	0.9584	0.0083	2.9148
O5	1.1285	-0.0442	2.7448
O6	1.8660	-0.2392	1.9819
O7	1.9009	-0.2993	1.9124

Table 5.4: R-Z centers coordinates and rays for the DTT TF D-shape arcs (see Fig. 5.2).

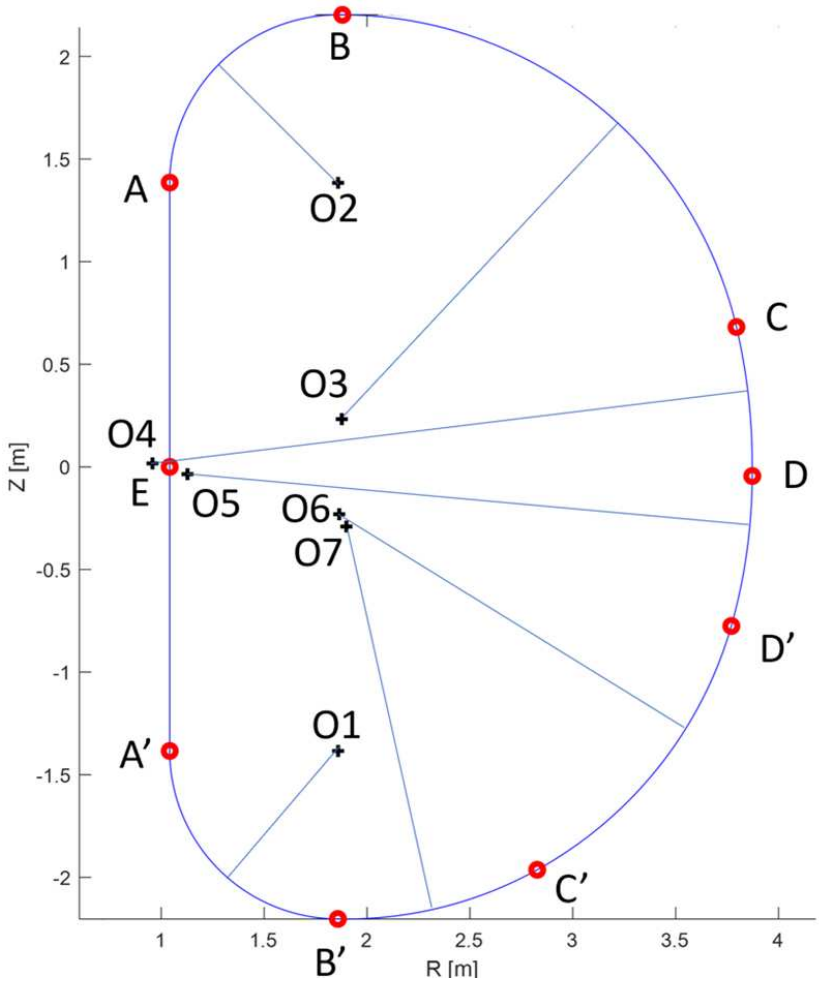

Figure 5.2: DTT TF D-shape sketch within geometrical data info adopted

The results about the magnets discretization, reported in Tabs. 5.5, 5.6 and 5.7, show that approximately 4000 sticks per filament for each magnet are sufficient to guarantee the required level of accuracy.

# of sticks	**1000**	**2000**	**3000**	**4000**	**5000**	**6000**	**7000**
Max Error [μT]	6.16	0.491	0.218	0.123	0.0786	0.0546	0.040

Table 5.5: CS: field error by varying source filament discretization of CS1 (the closest to the surface), where CS1 is obtained as the CS1-U H,CS1-U M and CS1-U L series (see Fig. 6.10).

# of sticks	**1000**	**2000**	**3000**	**4000**	**5000**	**6000**	**7000**
Max Error [μT]	6.16	1.75	0.777	0.437	0.247	0.171	0.126

Table 5.6: PF: field error by varying source filament discretization (PF3 the closest to the surface).

# of sticks	**1000**	**2000**	**3000**	**4000**	**5000**	**6000**	**7000**
Max Error [μT]	6.05	1.52	1.02	0.585	0.381	0.269	0.201

Table 5.7: TF: field error by varying source filament discretization (TF1).

5.2 Sampling of the q=2 surface in order to stabilize of the accuracy of TMEI harmonics.

An appropriate level of discretization of the q=2 surface was achieved to ensure adequate accuracy of the TMEI harmonics. In particular: (i) a reference instant was fixed (since the surface is associated with a specific instant, and at flat top the surface has the maximum volume); (ii) the number of points on the surface was varied to achieve stabilization of the significant digits of the TMEI harmonics at a desired level. The chosen instant as reference was a flat-top instant of a Single-Null scenario of DTT [3]. In Fig.5.3a and Fig.5.3b two examples of discretization levels of a DTT q=2 surface are shown.

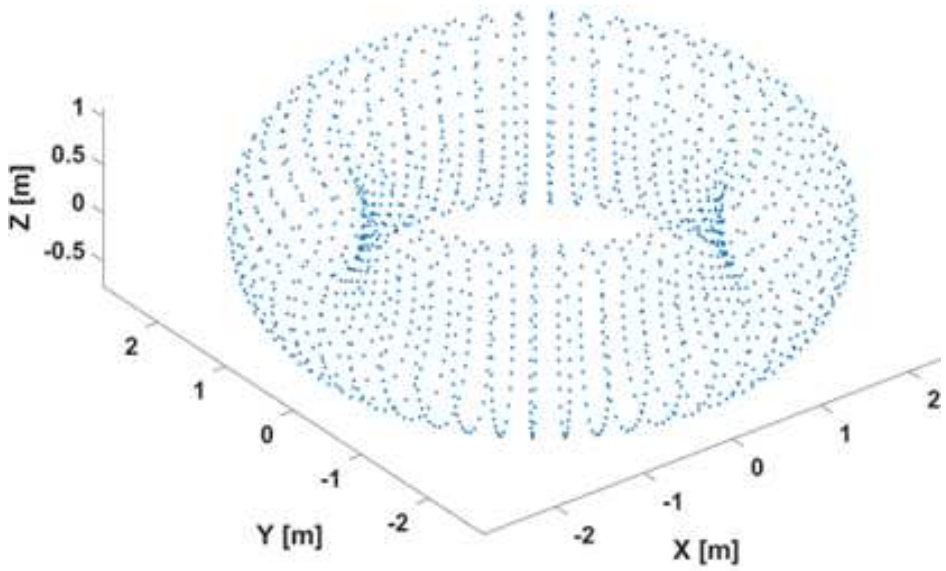

(a)

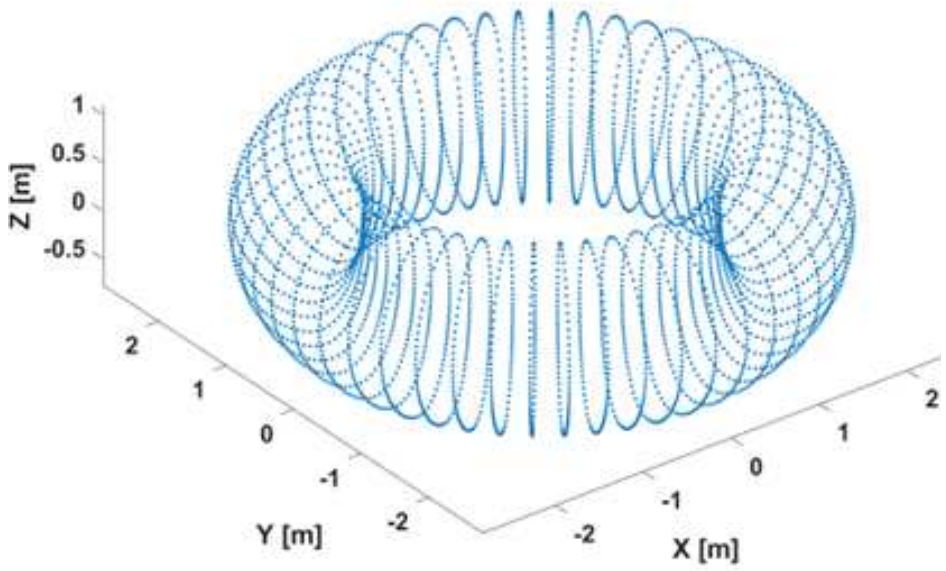

(b)

Figure 5.3: Coarse poloidal discretization level (about 30 samples) (a) and intermediate discretization level (about 100 samples) (b), with 50 cross sections along the toroidal direction, of the DTT q=2 surface at the flat-top reference instant.

Harmonics $\tilde{B}_{1,1}$, $\tilde{B}_{1,2}$ and $\tilde{B}_{1,3}$ were calculated by varying the number of samples along theta N_θ={400, 500, 600} and fixing the sampling along ϕ at 50 sections, and compared with the reference case at N_θ^{ref} =700. The three cases were obtained by rotating (since rotations are subject to greater approximation errors) CSs, PFs and TFs, independently fed at the current values of associated to the instant, and choosing the appropriate level of discretization (4000 sticks for each coils filament) in order to ensure the accuracy about 1μT. The results about the q=2 discretization, shown in Tabs. 5.8, 5.9 and 5.10, have suggested to use 600 poloidal samples and 50 cross sections along the toroidal direction in order to guarantee the accuracy level needed.

poloidal samples	$\|\Delta\tilde{B}_{1,1}\|$ [T]	$\|\Delta\tilde{B}_{1,2}\|$ [T]	$\|\Delta\tilde{B}_{1,3}\|$ [T]
400	2.741e-06	2.701e-06	2.083e-06
500	1.751e-06	1.701e-06	1.192e-06
600	5.441e-07	5.762e-07	4.619e-07

Table 5.8: Harmonics differences obtained comparing q=2 reference poloidal sampling (N_θ^{ref} =700 samples) and the three cases of sampling due to CS1 (obtained as the CS1-U H, CS1-U M and CS1-U L series, see Fig. 6.10) rotation along x (y) producing a maximum displacement of 4mm.

poloidal samples	$\|\Delta\tilde{B}_{1,1}\|$ [T]	$\|\Delta\tilde{B}_{1,2}\|$ [T]	$\|\Delta\tilde{B}_{1,3}\|$ [T]
400	8.349e-07	1.765e-06	5.506e-07
500	5.782e-07	1.031e-06	3.359e-07
600	1.803e-07	4.014e-07	8.425e-08

Table 5.9: Harmonics differences obtained comparing q=2 reference poloidal sampling (N_θ^{ref} =700 samples) and the three cases of sampling due to PF3 rotation along x (y) producing a maximum displacement of 4mm.

poloidal samples	$\|\Delta\tilde{B}_{1,1}\|$ [T]	$\|\Delta\tilde{B}_{1,2}\|$ [T]	$\|\Delta\tilde{B}_{1,3}\|$ [T]
400	2.618e-07	1.452e-06	2.565e-07
500	1.902e-07	8.051e-07	1.317e-07
600	5.144e-08	3.461e-07	7.383e-08

Table 5.10: Harmonics differences obtained comparing q=2 reference poloidal sampling (N_θ^{ref} =700 samples) and the three cases of sampling due to TF rotation along x (y) producing a maximum displacement of 4mm.

5.3 Validation of the first order Taylor approximation on DTT

Validation of the PF, CS, TF Taylor approximation: comparison between the "approximate" TMEI harmonics (obtained using the first order Taylor approximation) and the actual TMEI harmonics within the bounds of 1μT. Tables 5.11, 5.12, 5.13, 5.14, 5.15, 5.16 and 5.17 show the results about the linearity check on the harmonics, while Fig. 5.4 shows the normal component of the EF amplitude on the q=2 points of both the methods for a TF tilting with a maximum displacement of 4 mm. The discrepancy is less than 2%.

TMEI harms	**Actual [T]**	**Approximate [T]**	**Δ [T]**
$\tilde{B}_{1,1}$	6.8873e-06-5.9813e-06i	6.8873e-06-5.9813e-06i	-1.5404e-12-1.2757e-12i
$\tilde{B}_{1,2}$	1.2689e-06+5.2724e-06i	1.2689e-06+5.2724e-06i	2.1661e-12-3.5998e-13i
$\tilde{B}_{1,3}$	-2.7111e-06-2.4265e-07i	-2.7111e-06-2.4265e-07i	-4.0336e-13+1.4542e-12i

Table 5.11: CS3: comparison of actual and approximate harmonic: translations in x (y) of 1mm.

TMEI harms	**Actual [T]**	**Approximate [T]**	**Δ [T]**
$\tilde{B}_{1,1}$	1.378e-5-1.196e-5i	1.378e-5-1.196e-5i	-1.2323e-11-1.0205e-11i
$\tilde{B}_{1,2}$	2.538e-6+1.055e-5i	2.538e-6+1.055e-5i	1.7329e-11-2.8799e-12i
$\tilde{B}_{1,3}$	-5.422e-6-4.853e-7i	-5.422e-6-4.853e-7i	-3.2269e-12+1.1634e-11i

Table 5.12: CS3: comparison of actual and approximate harmonic: translations in x (y) of 2mm.

TMEI harms	**Actual [T]**	**Approximate [T]**	**Δ [T]**
$\tilde{B}_{1,1}$	2.7549e-05-2.3925e-05i	2.7549e-05-2.3925e-05i	-9.8586e-11-8.1643e-11i
$\tilde{B}_{1,2}$	5.0756e-06+2.109e-05i	5.0755e-06+2.109e-05i	1.3863e-10-2.304e-11i
$\tilde{B}_{1,3}$	-1.0844e-05-9.7051e-07i	-1.0844e-05-9.7061e-07i	-2.5815e-11+9.3071e-11i

Table 5.13: CS3: comparison of actual and approximate harmonic: translations in x (y) of 4mm.

TMEI harms	**Actual [T]**	**Approximate [T]**	**Δ [T]**
$\tilde{B}_{1,1}$	-2.1464e-05+1.5018e-05i	-2.1464e-05+1.5018e-05i	-3.7045e-11+2.395e-11i
$\tilde{B}_{1,2}$	-2.5411e-05+1.705e-05i	-2.5411e-05+1.705e-05i	-6.8007e-11+6.4314e-12i
$\tilde{B}_{1,3}$	-1.9484e-05+5.4413e-06i	-1.9484e-05+5.4413e-06i	-7.4846e-11-2.7112e-11i

Table 5.14: PF3: comparison of actual and approximate harmonic: translations in x (y) of 4mm.

TMEI harms	Actual [T]	Approximate [T]	Δ [T]
$\tilde{B}_{1,1}$	1.8439e-05-4.8542e-05i	1.8402e-05-4.8473e-05i	3.7261e-08-6.8611e-08i
$\tilde{B}_{1,2}$	3.2766e-05-1.7622e-05i	3.2648e-05-1.7604e-05i	1.1812e-07-1.841e-08i
$\tilde{B}_{1,3}$	1.9775e-05-4.7036e-06i	1.9683e-05-4.7145e-06i	9.2599e-08+1.0882e-08i

Table 5.15: PF3: comparison of actual and approximate harmonic: tilting along x (y) with a maximum displacement of 4mm.

TMEI harms	Actual [T]	Approximate [T]	Δ [T]
$\tilde{B}_{1,1}$	3.4447e-05-0.00024712i	3.4454e-05-0.00024715i	-7.3117e-09+3.1648e-08i
$\tilde{B}_{1,2}$	5.1495e-06+1.0046e-06i	5.1489e-06+1.0054e-06i	6.2063e-10-7.7301e-10i
$\tilde{B}_{1,3}$	-2.0834e-05+1.5072e-05i	-2.0837e-05+1.5074e-05i	2.1606e-09-2.2623e-09i

Table 5.16: TF: comparison of actual and approximate harmonic: translations in x of 4mm (y and z comparable).

TMEI harms	Actual [T]	Approximate [T]	Δ [T]
$\tilde{B}_{1,1}$	-1.8048e-04+1.3487e-04i	-1.8043e-04+1.3492e-04i	-4.8839e-08-5.0051e-08i
$\tilde{B}_{1,2}$	-9.4831e-06-2.317e-05i	-9.479e-06-2.3291e-05i	-4.0798e-09+1.2129e-07i
$\tilde{B}_{1,3}$	1.6688e-05+1.0209e-05i	1.6694e-05+1.0237e-05i	-6.4089e-09-2.8171e-08i

Table 5.17: TF: comparison of actual and approximate harmonic: 3D-Spline on 9 control points, with a maximum deformation of 4mm.

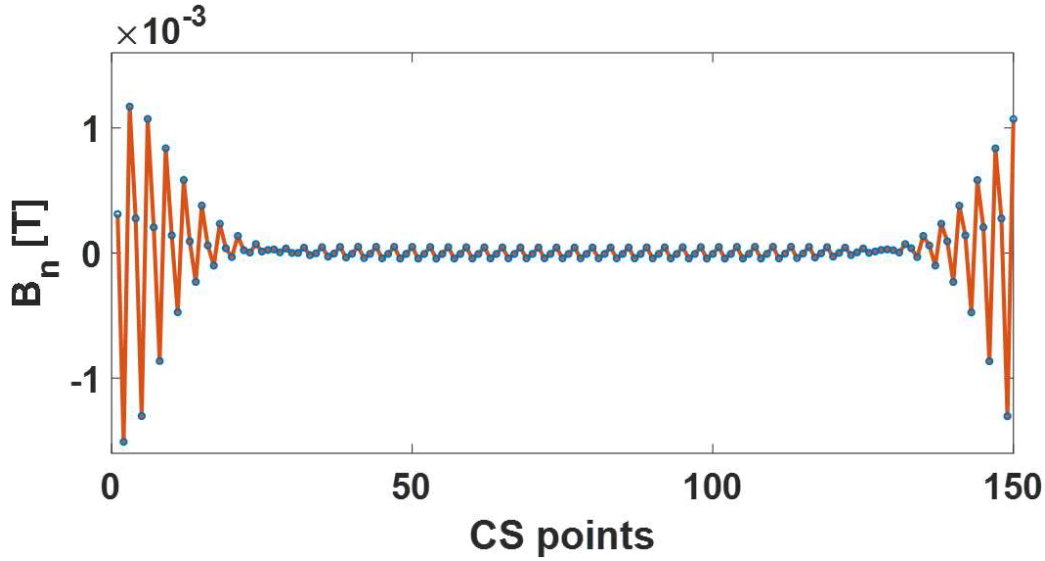

Figure 5.4: DTT TF tilting producing a maximum displacement of 4mm: comparison between B_n from the 1^{st} order Taylor (blue circles) and direct computation using MISTIC (orange curve).

5.4 Validation of the first order Taylor approximation tool on DEMO

Here the linearity check has been approached together with the validation of the MARS-F vacuum interface matrix using the model shown in Section 3.4. For the linearity check, a tilting producing a maximum displacement of 2mm of both DEMO PF and TF are considered [3]. The EF has been computed both using CARIDDI and the 1^{st} Taylor tool. Each coil filament has been discretized using 4000 sticks and the coupling surface using 99×150 points, where 99 is the sampling in the toroidal angle ϕ and 150 in the toroidal angle θ. The comparison between the outputs produced an error less than 2%. Fig. 5.5 and Fig. 5.6 show the normal component of the EF on the coupling surface of both the tools for the PF3 and the TF respectively.

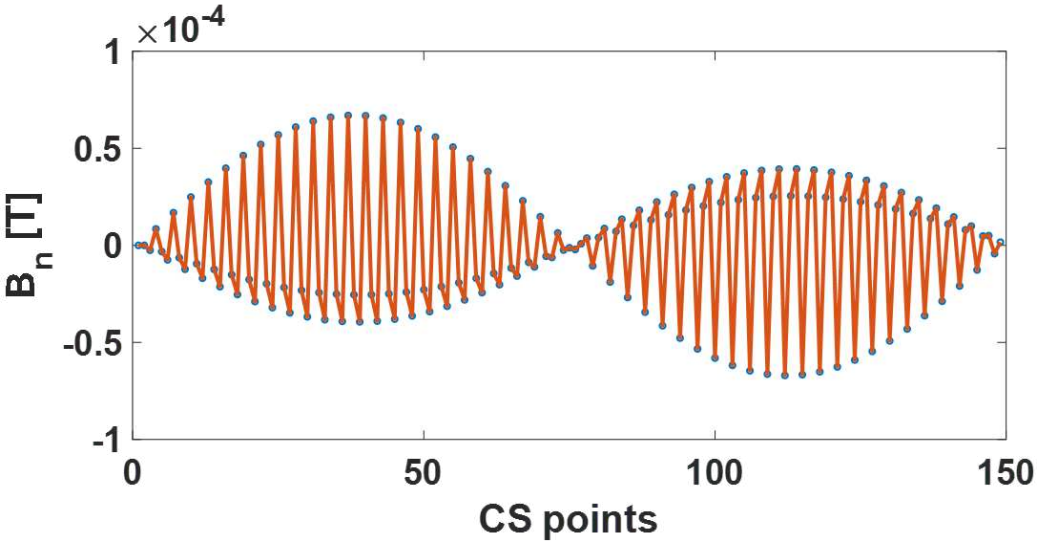

Figure 5.5: DEMO PF3 tilting producing a maximum displacement of 2mm: comparison between B_n from the 1^{st} order Taylor (blue circles) and CARIDDI direct computation (orange curve).

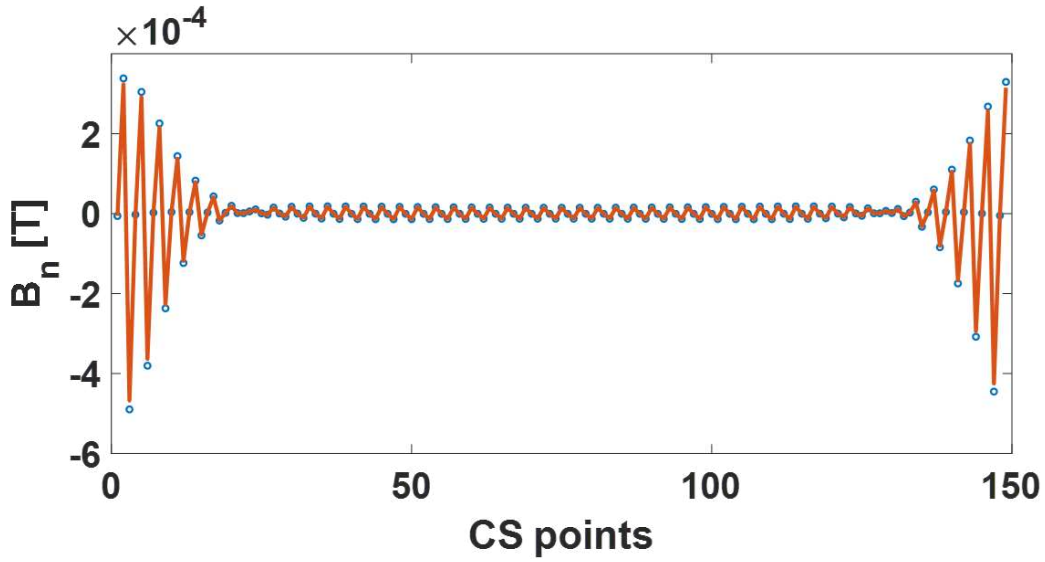

Figure 5.6: DEMO TF tilting producing a maximum displacement of 2mm: comparison between B_n from the 1^{st} order Taylor (blue circles) and CARIDDI direct computation (orange curve).

The MARS-F vacuum response matrix $\underline{\underline{K}}_{resp}$ on the q=2 surface is used to compute the poloidal spectrum of the normal component of the EFs starting from those on the coupling surface, obtained as a result of direct computation on the coupling surface. Then, a direct computation of such field on q=2 is also performed. Fig 5.7 and Fig. 5.8 show a good agreement from the comparison between the direct computation and MARS-F output for PF tilting and TF tilting respectively.

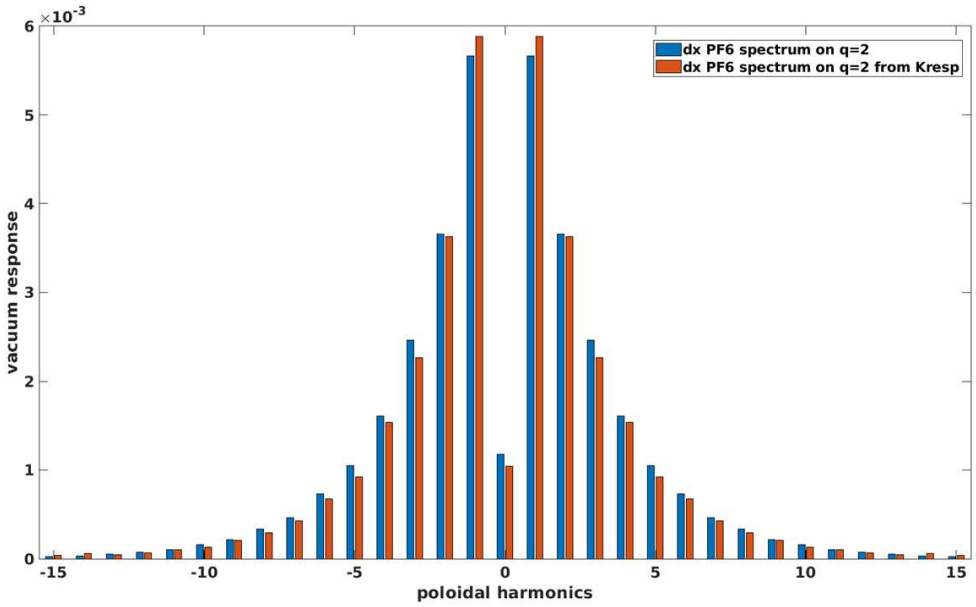

Figure 5.7: Vacuum response spectrum due to a PF6 tilting with a maximum displacement of 1mm: MARS-F interface matrix output (red bars) and direct computation (blue bars).

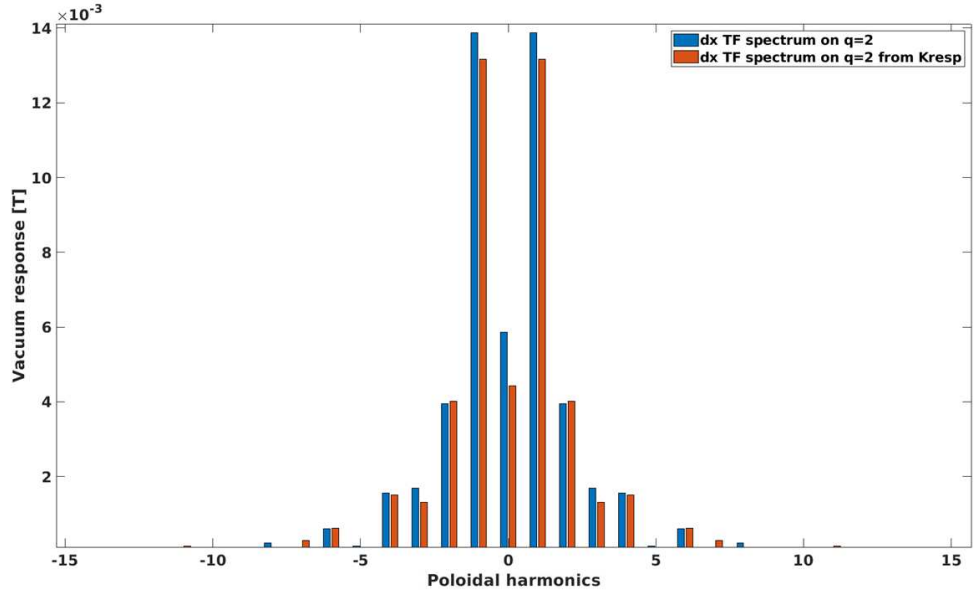

Figure 5.8: Vacuum response spectrum due to a TF1 tilting with a maximum displacement of 1mm: MARS-F interface matrix output (red bars) and direct computation (blue bars).

Bibliography

[1] R. Martone, et al. (Eds.), DTT Divertor Tokamak Test facility Interim Design Report, ENEA ("Green. Book"). ISBN 978-88-8286-378-4, https://www.dtt-dms. enea.it/share/s/avvglhVQT2aSkSgV9vuEtw, 2019.

[2] A. Castaldo, et al. (2000). Plasma Scenarios for the DTT Tokamak with Optimized Poloidal Field Coil Current Waveforms. Energies. Energies, 15(5), 1702, 1804-1807. DOI: 10.3390/en15051702.

[3] Author private communication.

6
Results

The tool presented in Section 2.4, which utilizes a first-order Taylor approximation, has been here used to perform a Monte Carlo analysis. This analysis provided worst cases of EFs resulting from deviations of the magnets from their nominal configuration. Furthermore, the currents of the EFCCs were optimized for correction purposes. The EFs analysis was carried out for the DTT, JT60SA and DEMO tokamaks. The JT60SA EFs analysis was performed to validate the results obtained by G. Matsunaga and his research team. For both JT60SA and DTT devices, the TMEI criterion was employed, whereas for DEMO, the Overlap field criterion was chosen to include the plasma response. Finally, the effectiveness of the method presented in chapter 4 is benchmarked in two different applications for which analytical solutions are available.

6.1 JT60SA EFs estimation and correction

HERE, the EFs analysis has been performed, considering CS/PF currents of the flat-top instant of the JT60SA reference Scenario and TF currents, to reproduce comparable results as in [5]. The threshold above which the effects of EFs are considered harmful in JT60SA has been identified as 100 ppm, but a safety coefficient of 2 has been introduced. The threshold considered was than:

$$B_{TMEI} < 0.1\ mT\ (TMEI < 50\ ppm) \tag{6.1}$$

where $B_{TMEI}= TMEI \cdot B_t$, and B_t is the toroidal field on the magnetic axis of JT60SA.

6.1.1 TMEI Estimation due to magnets misalignments

The TF system consists of 18 identical D-shaped coils, produces a toroidal field about 2.25T on the device axis, while the set of axisymmetric coils used is illustrated in Tab. 6.1 and Tab. 6.2. The PF/CS system has been perturbed using two typologies of parameters: i) assembly inaccuracies, modelled as translations respect to x, y and z directions, and rotations respect to $\widetilde{x}//x$, $\widetilde{y}//y$ and z axes, passing through the coil barycenter (see Fig. 2.4). TF assembly inaccuracies are implemented similarly to the PF/CS case but using a suitable coordinate system $(\widetilde{r}, \widetilde{t}, \widetilde{z})$ (see Fig. 2.5). Manufacturing errors are not included in this analysis.

Name	R_B **[m]**	Z_B **[m]**	**DR [m]**	**DZ [m]**	**nR**	**nZ**
CS1	0.822	2.407	0.327	1.574	23	23
CS2	0.822	0.802	0.327	1.574	23	23
CS3	0.822	-0.802	0.327	1.574	23	23
CS4	0.822	2.407	0.327	1.574	23	23

Table 6.1: JT60SA CS system geometrical info adopted.

Name	R_B **[m]**	Z_B **[m]**	**DR [m]**	**DZ [m]**	**nR**	**nZ**
PF1	5.801	1.179	0.329	0.334	12	12
PF2	4.607	3.171	0.357	0.334	13	12
PF3	1.913	4.025	0.543	0.428	18	14
PF4	1.913	-4.117	0.543	0.611	18	20
PF5	3.902	-3.722	0.302	0.39	11	14
PF6	5.039	-2.774	0.357	0.39	13	14

Table 6.2: JT60SA PF system geometrical info adopted.

For the stochastic analysis, N_{cases}=1e6 has been considered and bounds for the maximum perturbations have been introduced (see in Tab. 6.3). The histograms of the pdf of the $TMEI$ (B_{TMEI}) and the first three harmonics B_{11}, B_{21} and B_{31}, are reported in Figs. 6.1, 6.2, 6.3 and 6.4 respectively.

	CS [mm]	PF [mm]	TF [mm]
Translations	2.0	4.0	4.0
Rotations	2.0	4.0	4.0
Deformations	Not present	Not present	4.0

Table 6.3: CS, PF and TF deformations bounds.

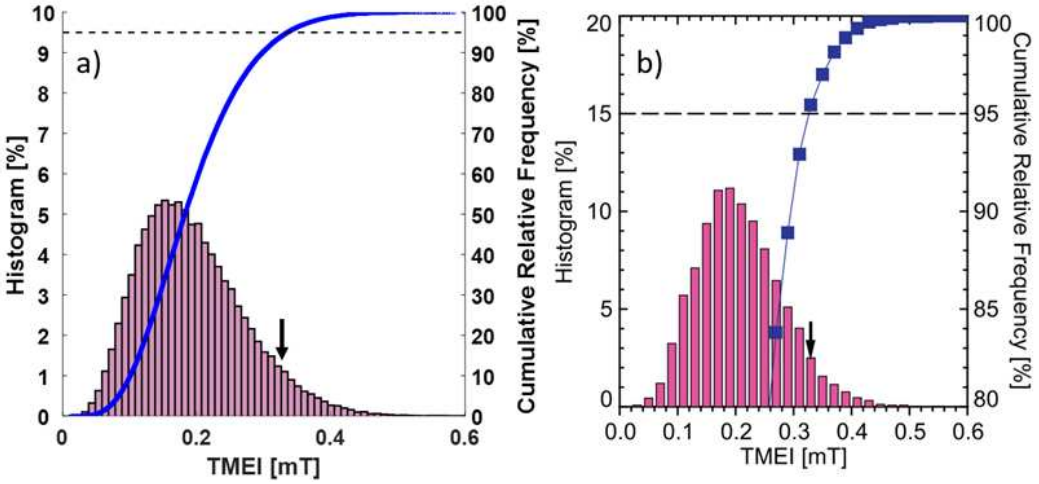

Figure 6.1: JT60SA predicted B_{TMEI} from TF and PF coils: upper obtained using the method presented, lower from G. Matsunaga results [5].

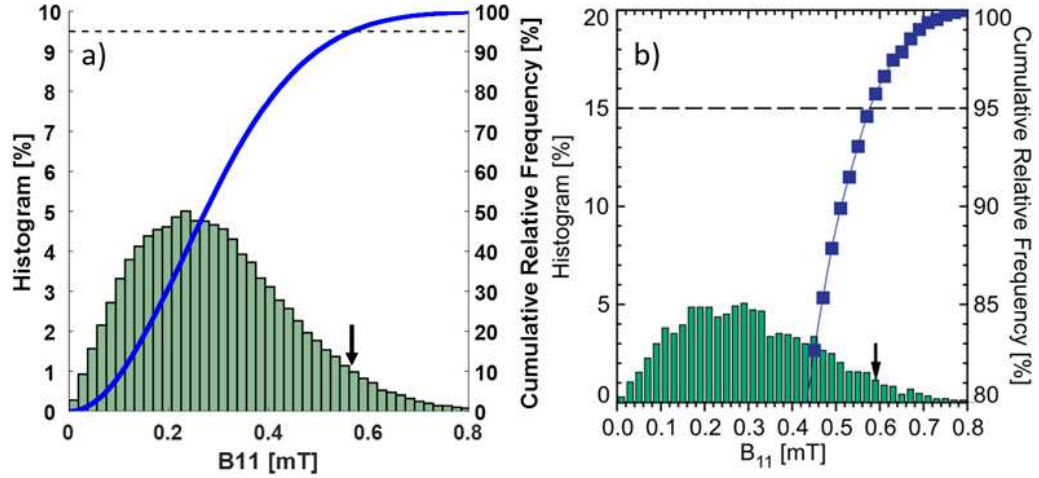

Figure 6.2: JT60SA predicted B_{11} EF harmonic from TF and PF coils: upper obtained using the method presented, lower from G. Matsunaga results [5].

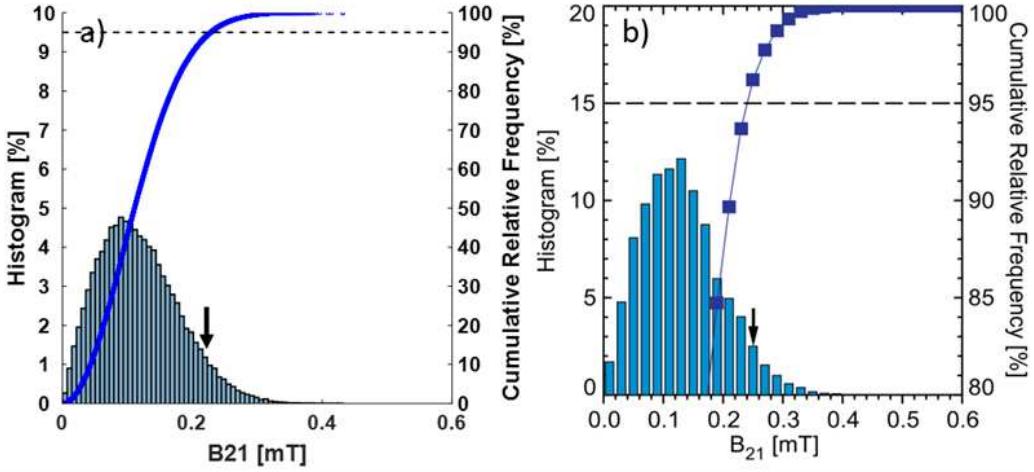

Figure 6.3: JT60SA predicted B_{21} EF harmonic from TF and PF coils: upper obtained using the method presented, lower from G. Matsunaga results [5].

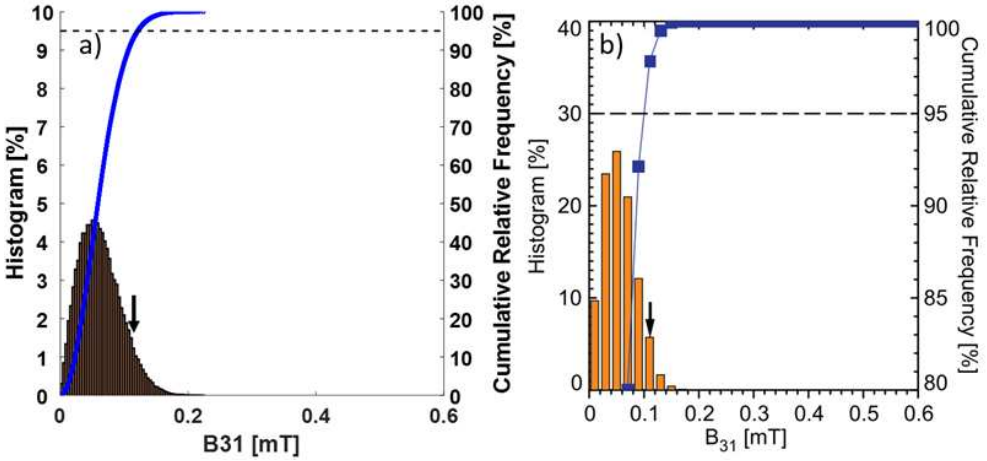

Figure 6.4: JT60SA predicted B_{31} EF harmonic from TF and PF coils: upper obtained using the method presented, lower from G. Matsunaga results [5].

6.1.2 TMEI Correction action

An EFCC system, consisting in three arrays of 6 identical independent filamentary copper coils (just the Centre Coils Lines (CCLs) of the saddle coils considered), is arranged on the inner wall face of the vessel in order to correct the three poloidal modes of TMEI in JT60SA [5]. In Fig. 6.5 the CCLs of the 18 EFCCs, are shown. The results are similar to the ones obtained in [5], but the performance of the present method based on quadratic programming

is slightly better (Fig. 6.6) probably because a different approach has been used.

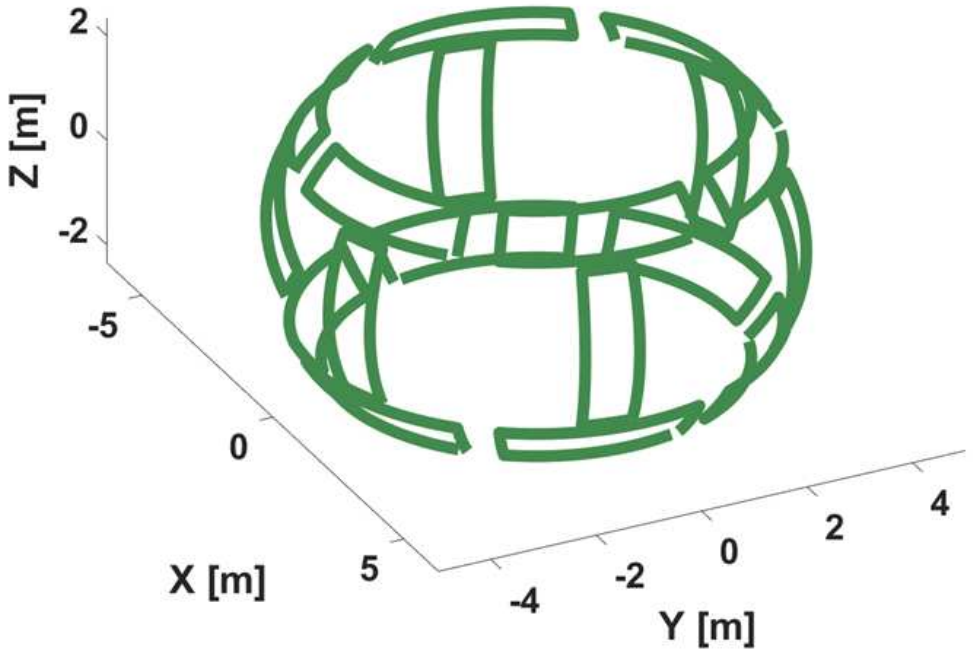

Figure 6.5: EFCCs system in JT-60SA [5].

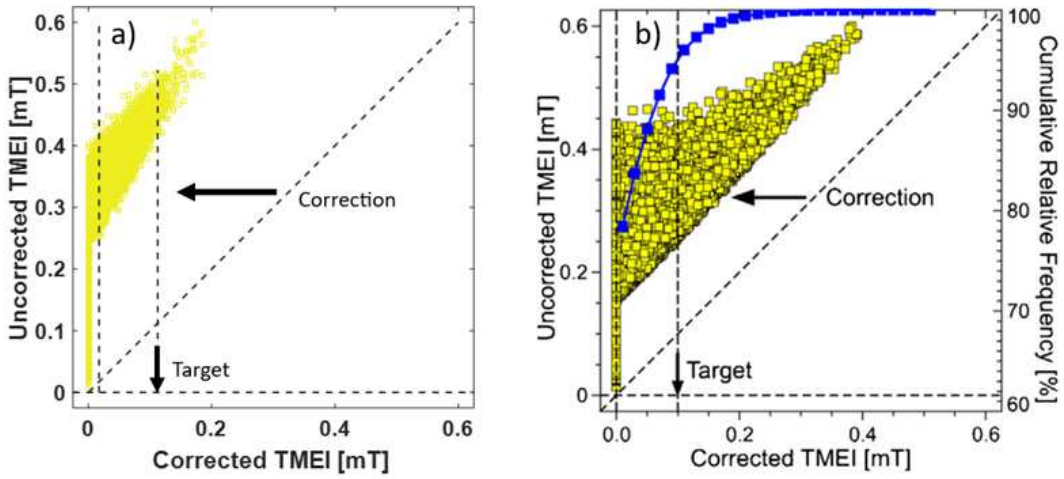

Figure 6.6: Diagrams of corrected vs. uncorrected TMEIs ($B_t[mT]$) by EFCC, left obtained using the method presented, right from G. Matsunaga results [5].

The histograms of required EFCC currents, limited within 45 kA are reported in Figs. 6.7, 6.8 and 6.9.

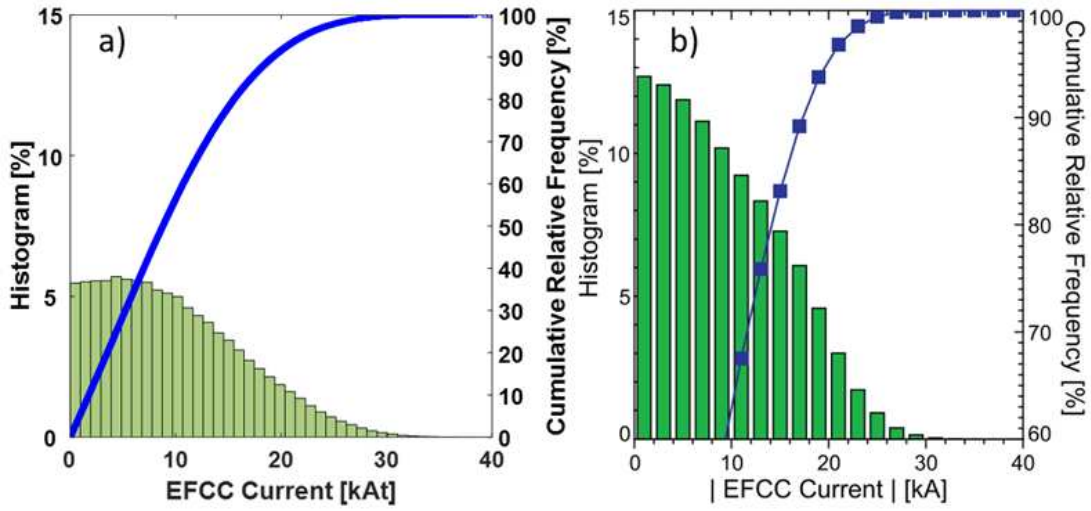

Figure 6.7: Histogram of required EFCC Upper array of currents: upper obtained using the method presented, lower from G. Matsunaga results [5].

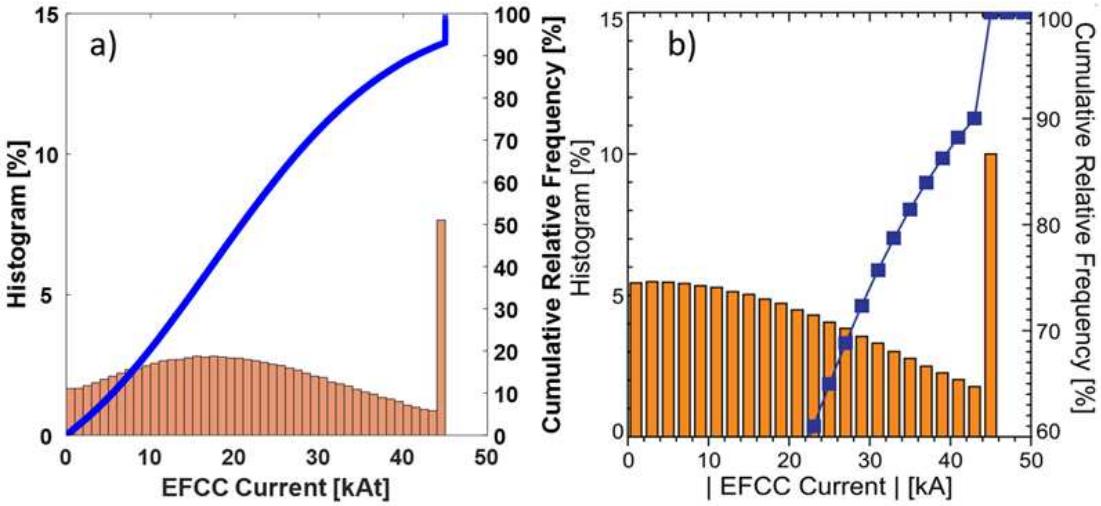

Figure 6.8: Histogram of required EFCC Middle array of currents: upper obtained using the method presented, lower from G. Matsunaga results [5].

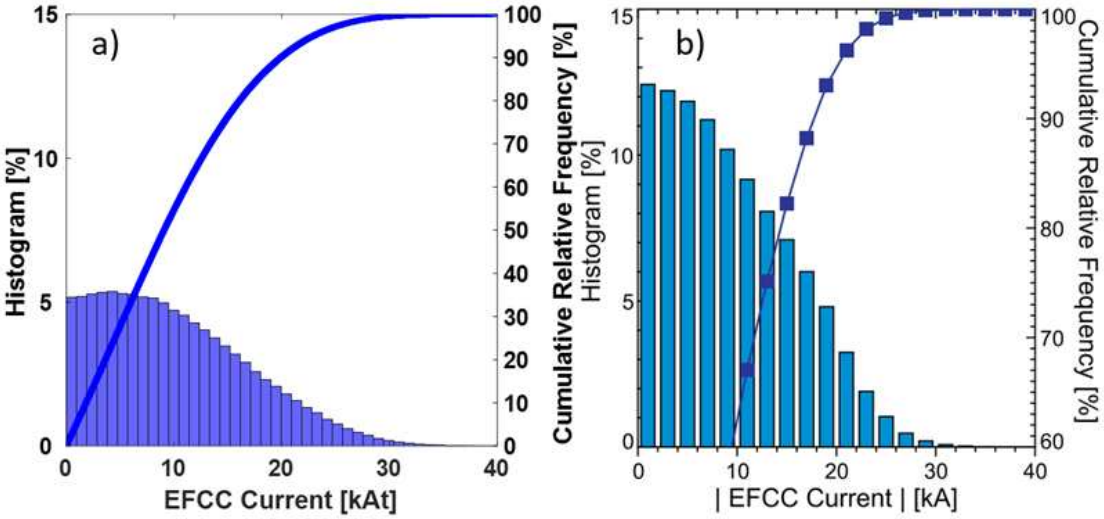

Figure 6.9: Histogram of required EFCC Lower array of currents: upper obtained using the method presented, lower from G. Matsunaga results [5].

6.2 DTT EFs estimation and correction

Here, the analysis, considering simplified models for the manufacturing and assembly inaccuracies, such as independent rigid displacement, rotations, and deformations of coils, has been carried out for DTT [1] to study the impact of the EFs and design an EFCCs system able to reduce the TMEI below a specific threshold. The threshold above which the effects of EFs are considered harmful in DTT has been identified as 100 ppm, but a safety coefficient of 2 has been introduced. The threshold considered was than:

$$TMEI < 50\ ppm \tag{6.2}$$

6.2.1 TMEI Estimation due to magnets misalignments

The EFs impact has been performed, considering CS/PF currents of the Single Null flat-top instant t=36s [2] and TF currents (Tab. 6.4). The TF system consists of 18 identical D-shaped coils, produces a toroidal field of 6T on the device axis, while the set of axisymmetric coils used is illustrated in Tab. 5.1 and Tab. 5.2. The PF/CS system has been perturbed using two typologies of parameters: i) assembly inaccuracies, modelled as translations respect to x, y and z directions, and rotations respect to $\widetilde{x}//x$, $\widetilde{y}//y$ and z axes, passing through the coil barycenter (see Fig. 2.4). Manufacturing errors, modelled as deformations, implemented as an elliptical striation parameter and a coil radius perturbation do not act on n=1 modes since they have no impact on the TMEI and can be disregarded. TF assembly inaccuracies are implemented similarly to the PF/CS case but using a suitable coordinate system $(\widetilde{r}, \widetilde{t}, \widetilde{z})$ (see Fig. 2.5). The non-rigid deformations, working on TF D-shape, have been implemented using cubic spline interpolation functions on nine control points (for more details see section 2.4.1). In Fig. 6.10 a poloidal sketch of DTT together with the CCLs of the three correction coil arrays is shown.

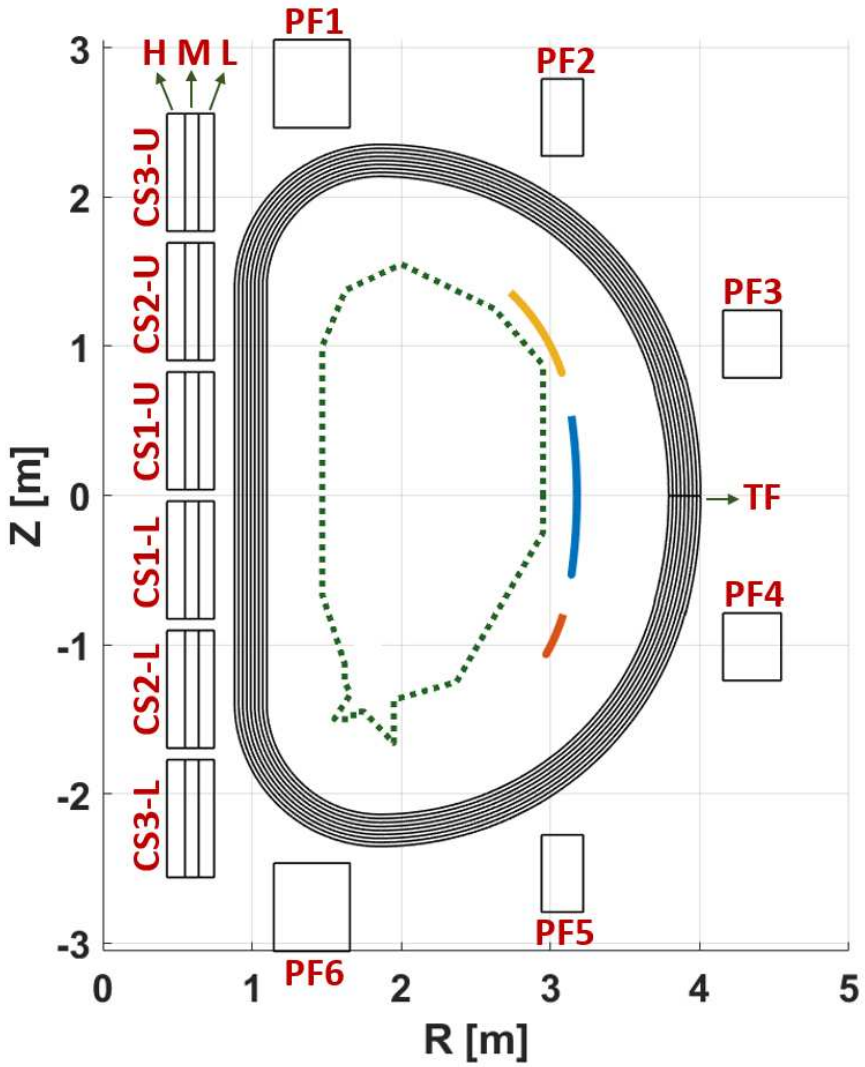

Figure 6.10: sketch of DTT magnetic system (black), EFCCs (upper (yellow), equatorial (blue) and lower (red)) coil profiles and First Wall (dark green dots).

Name	Current [MAt]
PF1	4.109
PF2	-1.815
PF3	-1.910
PF4	-3.211
PF5	-2.047
PF6	9.331
CS3U-H	-0.07104
CS3L-H	-1.346
CS3U-M	-0.08358
CS3L-M	-1.583
CS3U-L	-0.1504
CS3L-L	-2.850
CS2U-H	0.3978
CS2L-H	-0.9327
CS2U-M	0.4680
CS2L-M	-1.097
CS2U-L	0.8424
CS2L-L	-1.975
CS1U-H	-1.596
CS1L-H	0.2946
CS1U-M	-1.878
CS1L-M	0.3466
CS1U-L	-3.380
CS1L-L	0.6239
TFs (× 18)	3.520

Table 6.4: CS/PF and TF currents of the flat-top reference instant.

For the stochastic analysis, N_{cases}=1e6 has been considered and bounds for the maximum perturbations have been introduced (see in Tab. 6.5). A Gaussian distribution of deformation parameters, appropriately truncated to fit within the bounds, has been used.

	CS [mm]	PF [mm]	TF [mm]
Translations	2.0	4.0	4.0
Rotations	2.0	4.0	4.0
Deformations	Not present	Not present	4.0

Table 6.5: CS, PF and TF deformations bounds.

A cumulative distribution function (cdf) has been used to compute 80%, 90% and 95% of the cumulative TMEI values of the probability density function (pdf). Tab. 6.6 reports the TMEI values for different combinations, while Fig. 6.11 and Fig. 6.12 show the CS+PF+TF pdf for 1e6 and 1e7 cases, confirmation that 1e6 cases are sufficient to characterise worst cases of TMEI.

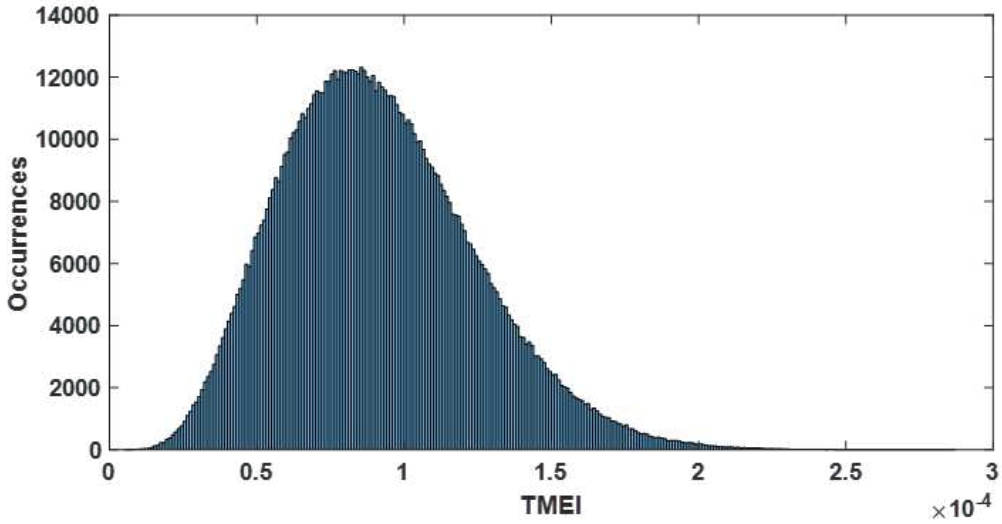

Figure 6.11: Pdf of CS+PF+TF contribution to TMEI, 1e6 cases.

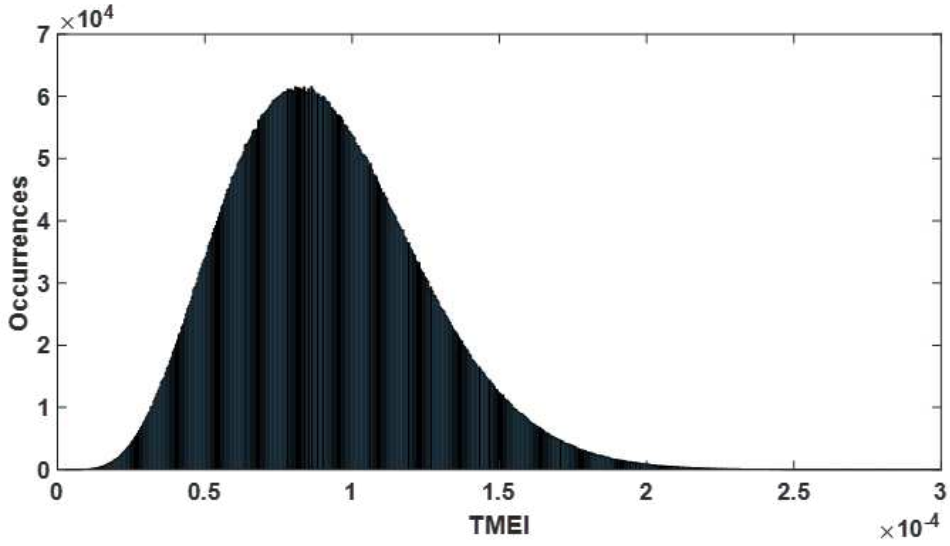

Figure 6.12: Pdf of CS+PF+TF contribution to TMEI, 1e7 cases.

Percentage	CS only	PF only	TF only	CS+PF+TF
80%	30.38	39.35	132.8	140.4
90%	35.39	45.48	154.2	162.0
95%	39.55	50.65	172.9	180.8

Table 6.6: TMEI (ppm) values for main percentages of the pdf.

6.2.2 TMEI Correction action

An EFCC system, consisting in three arrays of 9 identical independent filamentary copper coils (just the CCLs of the saddle coils considered), is arranged on the inner wall face of the vessel in order to correct the three poloidal modes of TMEI in DTT. In Tab. 6.7, the R-Z coordinates of upper (R_U,Z_U) and lower (R_L,Z_L) extremes of the CCLs poloidal profiles of each EFCC, are reported.

	R_U[m]	Z_U[m]	R_L[m]	Z_L[m]
Lower array	3.093	-0.7737	2.975	-1.072
Equat. array	3.142	0.5251	3.142	-0.5251
Upper array	2.729	1.399	3.109	0.8190

Table 6.7: R-Z coordinates of the CCL profiles of DTT correction coil arrays.

The analysis has shown that 50kAt are able to reduce the TMEI under 50 ppm in 95% of the cases considered, when the CS+PF+TF set of sources is used (see Fig. 6.13 and Tab. 6.8)[3]).

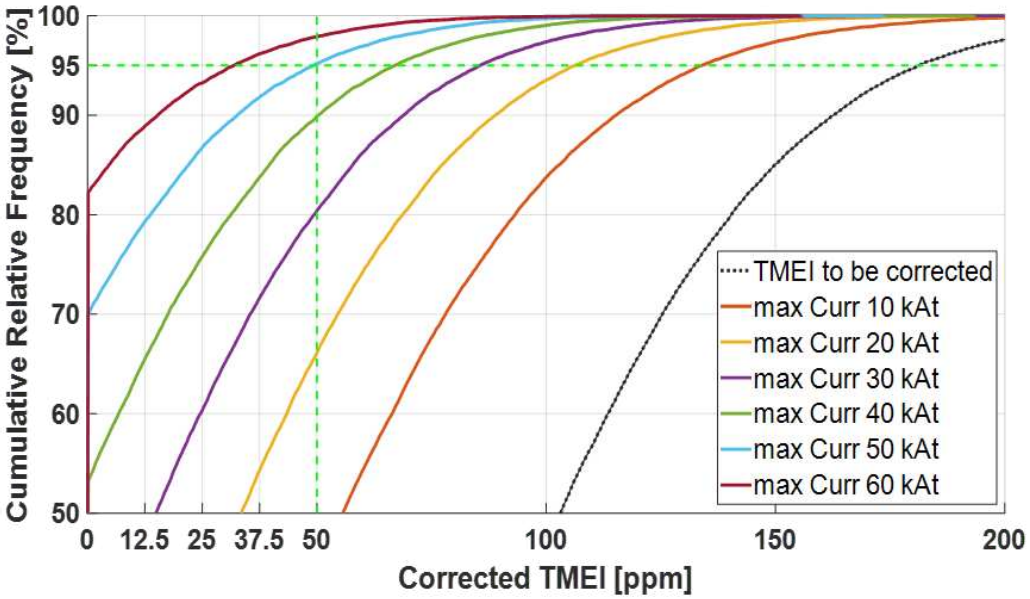

Figure 6.13: Cdf curves of TMEI varying currents constraints of EFCCs for the CS+PF+TF case. The 95% at 50 ppm has been highlighted.

Currents	CS only	PF only	TF only	CS+PF +TF	TF def. only	TF pert. only
10 kAt	100 %	100 %	49.78 %	44.01 %	80.70 %	73.21 %
20 kAt	100 %	100 %	70.72 %	66.12 %	93.77 %	90.17 %
30 kAt	100 %	100 %	84.43 %	80.43 %	98.35 %	97.06 %
40 kAt	100 %	100 %	92.41 %	89.87 %	99.66 %	99.28 %
50 kAt	100 %	100 %	96.62 %	95.18 %	99.95 %	99.84 %
60 kAt	100 %	100 %	98.76 %	97.85 %	100 %	99.98 %

Table 6.8: TMEI below 50 ppm: percentages of corrected cases varying EFCCs current bounds for different combinations of magnetic sources.

6.3 DEMO EFs estimation and correction in presence of plasma response

Here, the analysis, considering simplified models for the manufacturing and assembly inaccuracies, such as independent rigid displacement, rotations of coils, has been performed for the EU-DEMO to study the impact of the EFs, using the overlap field criterion, and designing an EFCCs system, able to reduce the perturbations below a specific threshold. The threshold above which the effects of EFs in presence of plasma reaction are harmful has been identified as:

$$OVF < 110\ ppm \tag{6.3}$$

Tab. 6.9 and Tab. 6.10 show the last version of the geometrical info of CS and PF systems in EU-DEMO. In Fig. 6.14 a poloidal sketch of DEMO together with the CCLs of the two correction coil arrays is shown.

Name	R_B **[m]**	Z_B **[m]**	**DR [m]**	**DZ [m]**	**nR**	**nZ**
CS1	2.77	7.07	0.80	2.99	13	50
CS2	2.77	4.08	0.80	2.99	13	50
CS3	2.77	-0.40	0.80	5.97	13	100
CS4	2.77	-4.88	0.80	2.99	13	50
CS5	2.77	-7.86	0.80	2.99	13	50

Table 6.9: DEMO CS system geometrical info adopted.

Name	R_B **[m]**	Z_B **[m]**	**DR [m]**	**DZ [m]**	**nR**	**nZ**
PF1	5.40	9.26	1.20	1.20	20	20
PF2	14.0	7.90	1.40	1.40	14	14
PF3	17.75	2.50	1.00	1.00	17	17
PF4	17.75	-2.50	1.00	1.00	17	17
PF5	14.0	-7.90	1.40	1.40	23	23
PF6	7.00	-10.50	2.00	2.00	33	33

Table 6.10: DEMO PF system geometrical info adopted

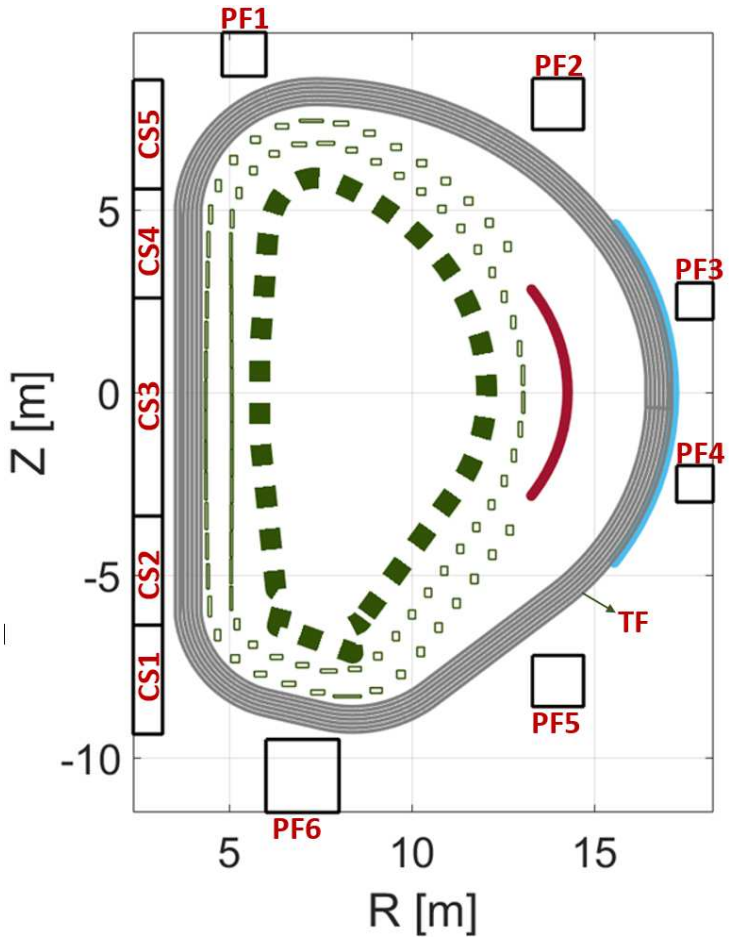

Figure 6.14: sketch of DEMO magnetic system (black), EFCCs Inner and outer (red and light blue coil profiles respectively) and blanket (dark green rectangles).

6.3.1 Estimation and correction of the overlap field due to magnets misalignments

The EFs impact has been performed, considering CS/PF currents of the flat-top instant of the DEMO reference Scenario and TF currents (Tab. 6.11) [4]. The TF system consists of 16 identical D-shaped coils, produces a toroidal field about 4.9T on the plasma axis (particular chosen case), while the set of axisymmetric coils used is illustrated in Tab. 6.9 and Tab. 6.10. The PF/CS system has been perturbed using two typologies of parameters: i) assembly inaccuracies, modelled as translations respect to x, y and z directions, and rotations respect to $\widetilde{x}//x$, $\widetilde{y}//y$ and z axes, passing through the coil barycenter

(see Fig 2.4). TF assembly inaccuracies are implemented similarly to the PF/CS case but using a suitable coordinate system $(\widetilde{r}, \widetilde{t}, \widetilde{z})$ (see Fig 2.5). Manufacturing errors are not included in this analysis.

Name	Current [MAt]
PF1	12.495
PF2	-3.807
PF3	-7.668
PF4	-1.654
PF5	-9.788
PF6	18.712
CS1	16.11
CS2	4.79
CS3	-3.27
CS4	0.77
CS5	22.01
TFs (× 16)	13.66

Table 6.11: CS/PF and TF currents of the flat-top reference instant

For the stochastic analysis, N_{cases}=1e6 and N_{cases}=1e7 have been considered and bounds for the maximum perturbations have been introduced (see in Tab. 6.12). The bounds are chosen scaling ITER bounds of 9/6 for the coils misalignments [6]. A uniform distribution of deformation parameters has been chosen.

	CS [mm]	PF [mm]	TF [mm]
Translations	3.0	3.0	3.0
Rotations	1.5	1.5	3.0 (1.5 along x)
Deformations	Not present	Not present	Not present

Table 6.12: CS, PF and TF deformations bounds

Fig. 6.15 and Fig. 6.16 show the CS+PF+TF pdf of N_{cases}=1e6 and N_{cases}=1e7 respectively and confirm 1e6 cases are sufficient to well characterise worst cases of OVF.

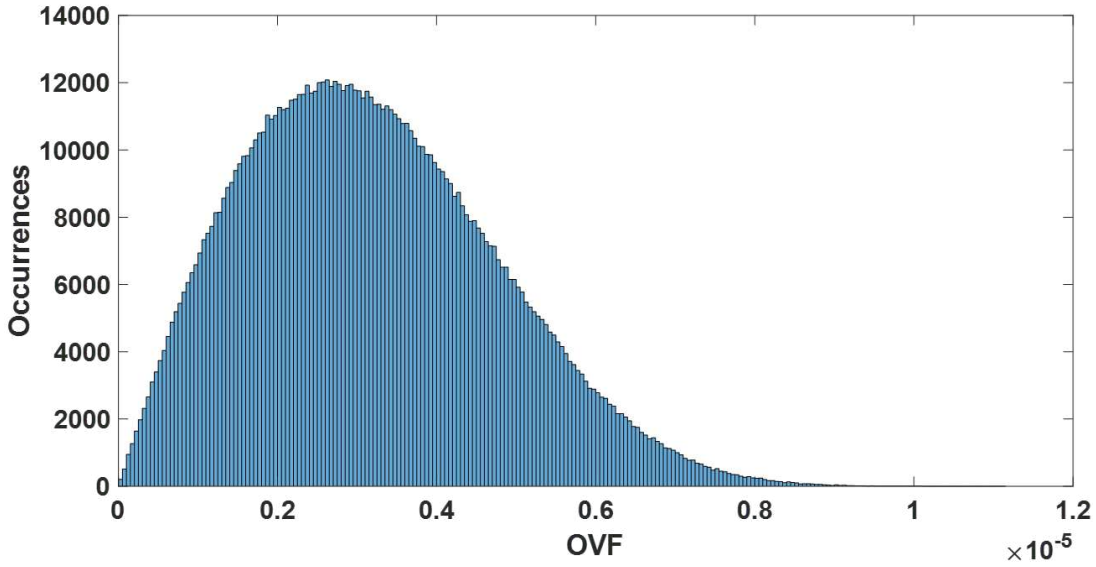

Figure 6.15: Pdf of CS+PF+TF contribution to OVF (1e6 cases).

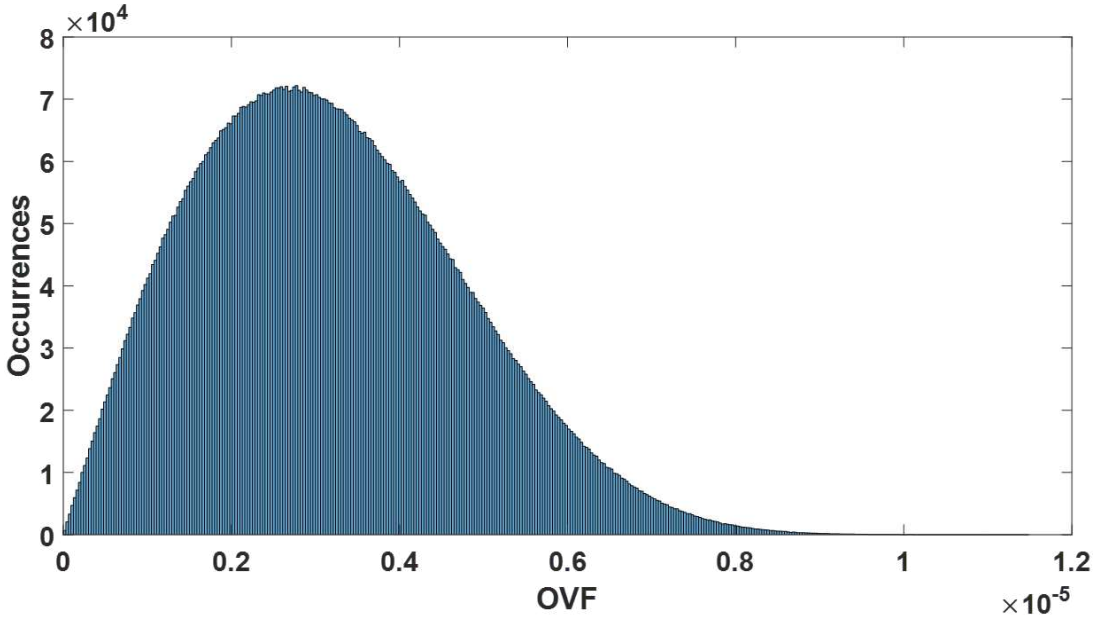

Figure 6.16: Pdf of CS+PF+TF contribution to OVF (1e7 cases).

Two different EFCC systems, consisting of an equatorial array of 16 identical independent filamentary coils, were considered independently. The two

arrays have been arranged on the inner wall face of the DEMO Breeding Blanket (BB) (inner array) and outside the TF system (outer array) respectively and both have been used to counteract the overlap field produced by the Monte Carlo analysis of the misalignments of the coils. In Tab. 6.17, the R-Z coordinates of upper (R_U,Z_U) and lower (R_L,Z_L) extremes of the CCLs poloidal profiles of each EFCC, are reported, while Fig. 6.17 shows a 3D sketch of the two sets of coils and their relative positioning with respect to the TF coil.

	R_U[**m**]	Z_U[**m**]	R_L[**m**]	Z_L[**m**]
Inner array	13.14	2.82	13.14	-2.82
Outer array	15.39	4.60	15.43	-4.65

Table 6.13: DEMO EFCCs system R-Z coordinates.

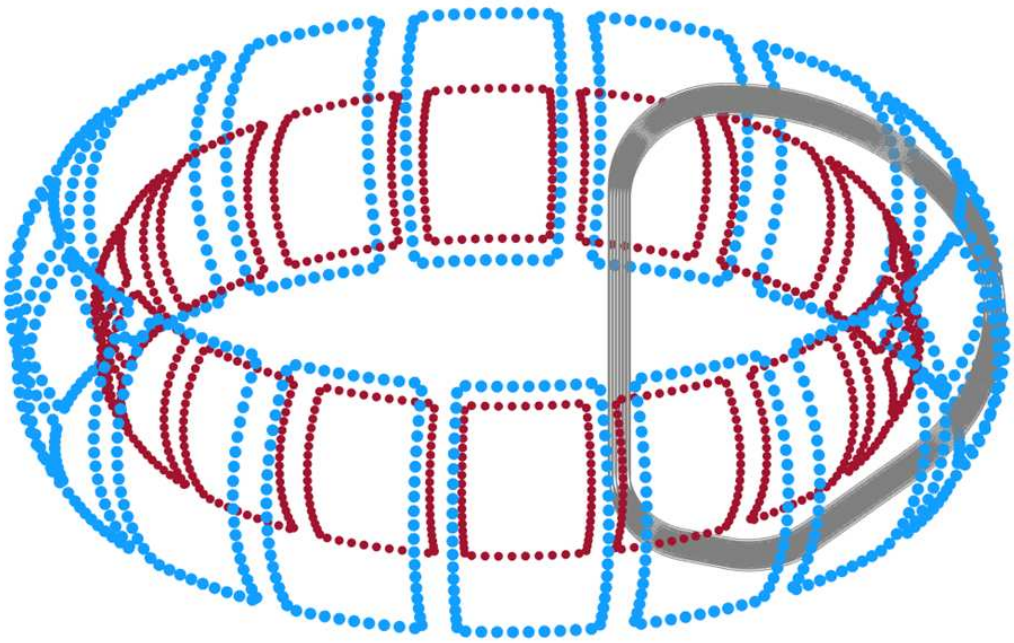

Figure 6.17: A pair of 16 equatorial EFCCs tested in DEMO: Inner (red saddles) and Outer array (light blue saddles) and TF coil (grey).

The correction action of the two sets of coils, performed solving (3.18) produced similar results (Figs. 6.18 and 6.19), but with a very different current demand.

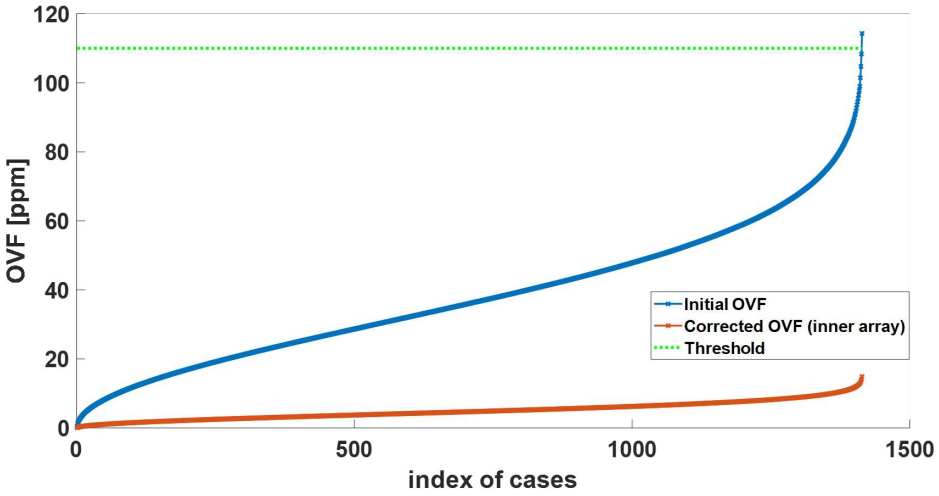

Figure 6.18: Correction action of the inner array: Initial OVF (blue curve), OVF after the correction (orange curve), threshold (dashed curve) for each case (ascending sort).

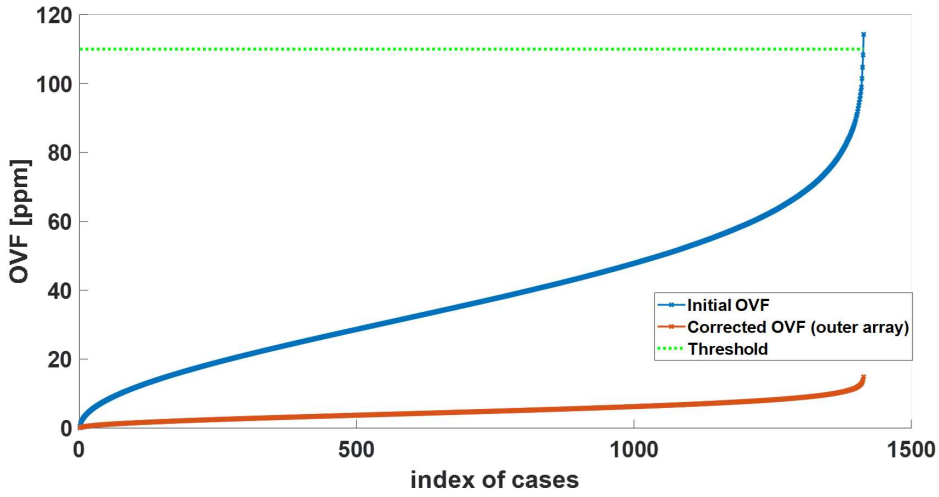

Figure 6.19: Correction action of the outer array: Initial OVF (blue curve), OVF after the correction (orange curve), threshold (dashed curve) for each case (ascending sort).

The analysis has shown that, when the CS+PF+TF set of EFs sources is used, the outer array has required a maximum current about 180kAt to reduce the overlap field below 20 ppm, while the inner array requires a very high current (see Fig. 6.20). The reason is related to the cancellation of the

main spectral components due to the proximity to the plasma (see Fig. 6.21). For this reason, the outer array, (or different configurations of correction coils) might be preferred for further analysis.

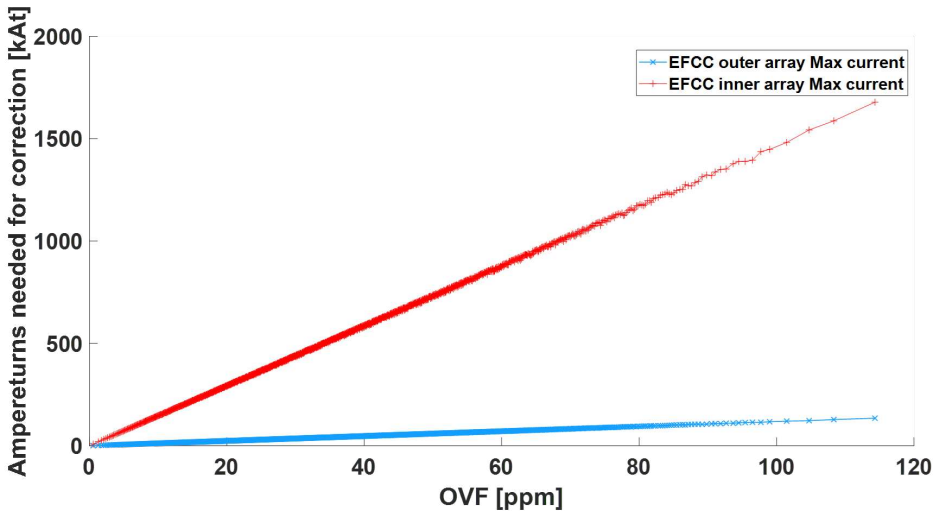

Figure 6.20: Correction action of both inner and outer array: maximum current demand for each case (ascending sort).

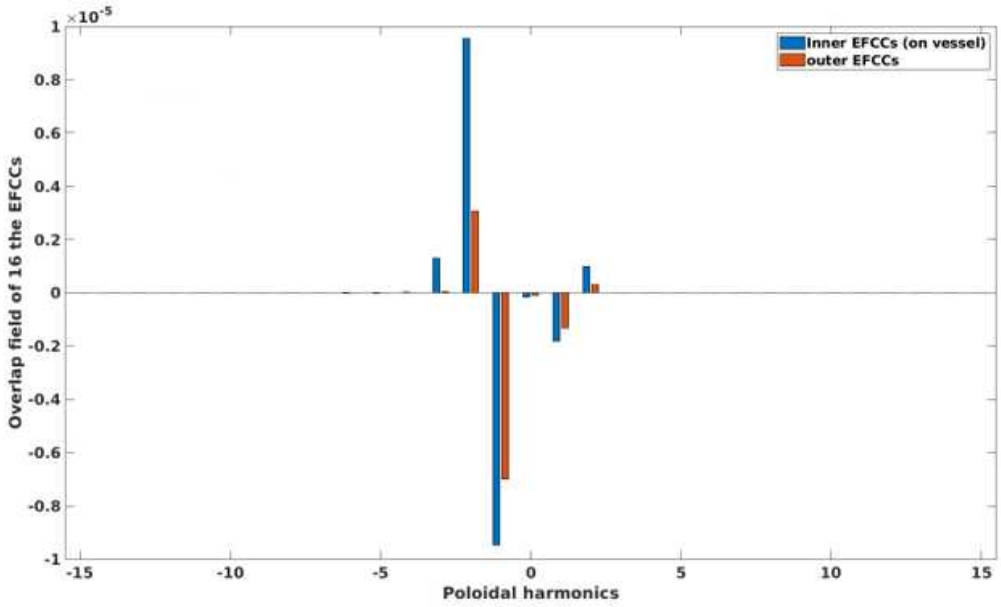

Figure 6.21: harmonics cancellation problem for the inner EFCCs array.

6.4 Overlap field effects due to ECRH ports discontinuities and magnetic system power supply in DEMO

The presence of additional asymmetries, such as ferromagnetic parts, magnet feeders (transmission lines and coil terminals), non-ideal coil winding distribution of the coils [7], etc., could affect the nominal magnetic configuration in a tokamak. Here, using the MARS-F interface matrices, the effect on the OVF due to the DEMO ferromagnetic BB cut-outs used as Electron Cyclotron Resonance Heating (ECRH) ports [8] and to the presence of the coil terminals [9], i.e. the terminating parts of the magnet power supply system, has been investigated.

6.4.1 Ferromagnetic ECRH ports OVF

The DEMO BB is the inner and ferromagnetic component that will be used to produce (or "breed") tritium fuel for the nuclear fusion reactions [10]. Although the DEMO BB is designed to cover about 85% of the plasma, several holes or ports are included for several purposes. The ferromagnetic material from which the BB is made, *EUROFER* steel [11], makes its discontinuities real magnetic sources that could alter the nominal magnetic configuration and need to be investigated. Here, the six ports hosting the ECRH antennas are considered for the analysis. The ports, arranged around the torus, break the periodicity and affect the n=1 toroidal mode as well as the poloidal modes of the OVF (see Fig. 6.22). Due to the high field to which is subjected (about 4T), the *EUROFER* BB reaches the saturation. A magnetization amplitude of about M=1.45e6 [A/m] has been estimated from the EUROFER initial magnetization curve (see Fig. 6.23). Although the main contribution is along the toroidal direction, a not negligible vertical component M_z is also present due to the poloidal field. From the equilibrium data [4] it results $B_t \approx$3.5T and $B_z \approx$1.2T at the ECRH port barycenter ($R_{\text{port}} \approx 12.43\,\text{m}$, $Z_{\text{port}} \approx 0.02\,\text{m}$). Therefore, less than one third of M amplitude is along the z axis. In Fig. 6.24 the toroidal field as function of r is reported together with the poloidal section of DEMO including the port barycenter.

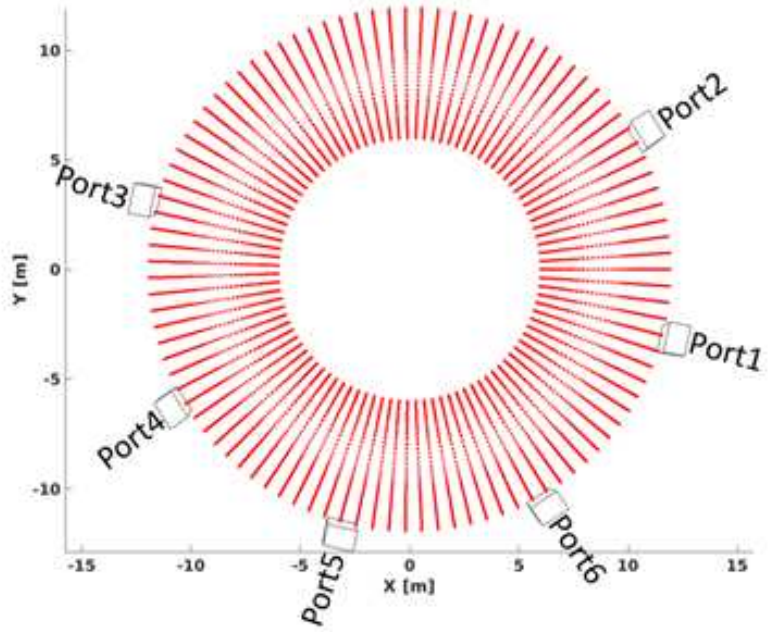

Figure 6.22: DEMO ports top view: initial 6-ports (white rectangles) and the boundary of the plasma (red dashed crown).

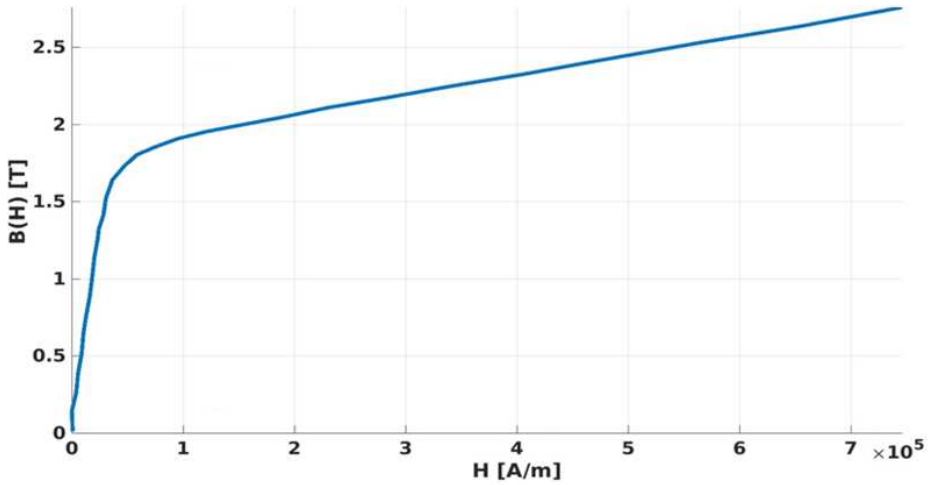

Figure 6.23: EUROFER initial magnetization curve.

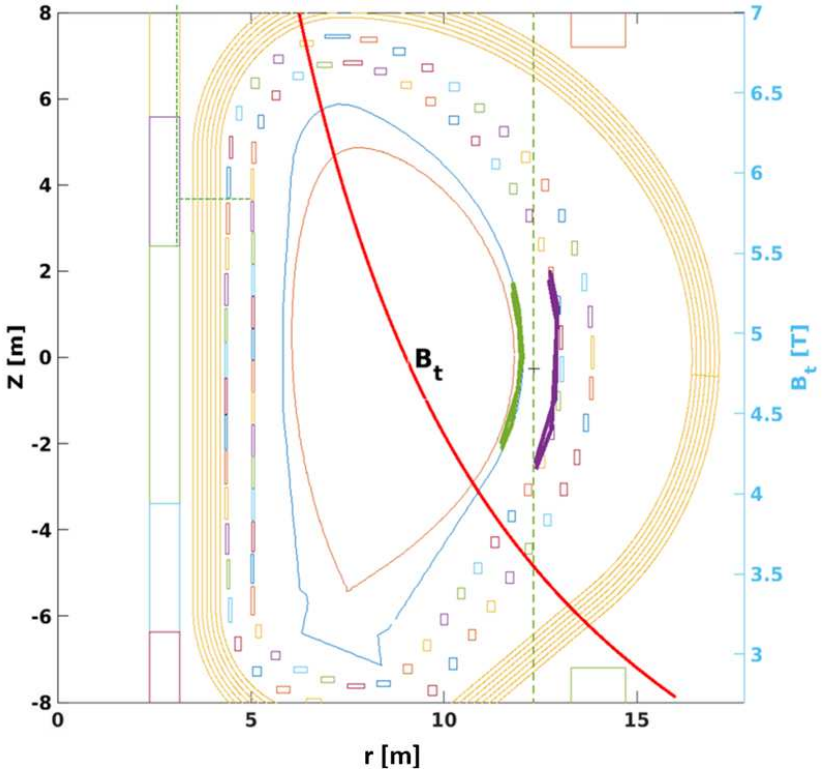

Figure 6.24: Overlapping between the toroidal field B_t as function of r (light blue axis) and poloidal section of DEMO (black axes). B_t=3.5T reached at the barycenter of the ECRH port.

Due to the size of the structure, the computational effort for the numerical treatment of the BB is very high. Here two different approaches, based on the compensation theorem, are shown. The ports have been treated as magnetic sources with opposite magnetization to the BB. This allows a huge reduction of the computational burden. The first method, based on an integral formulation [12], returns the magnetic field produced by uniformly magnetized polyhedrons (hexahedrons) used to discretize each port. The second approach treats the ports as windings fed by the currents previously "calibrated", in order to produce the desired magnetization at the windings barycenters.

In Figs. 6.25a and 6.25b the representations, based on the two approaches mentioned before, of a DEMO ECRH port, are reported. It should be clear that the second model has the only limitation of producing just a toroidal magnetization M_ϕ.

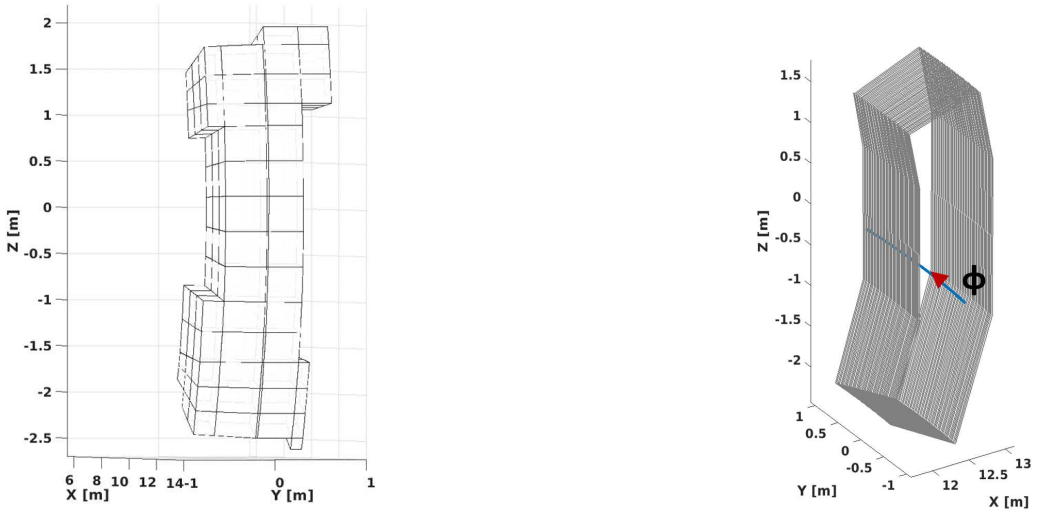

(a) (b)

Figure 6.25: Port model based on a) the use of magnetized hexahedrons, b) the use of winding producing the desired magnetization M_ϕ in the barycenter.

In order to compare the two approaches, only the toroidal component of the magnetization M_ϕ has been considered for the assessment. In Fig. 6.26 the two behaviors of normal component of the magnetic field B_n are reported.

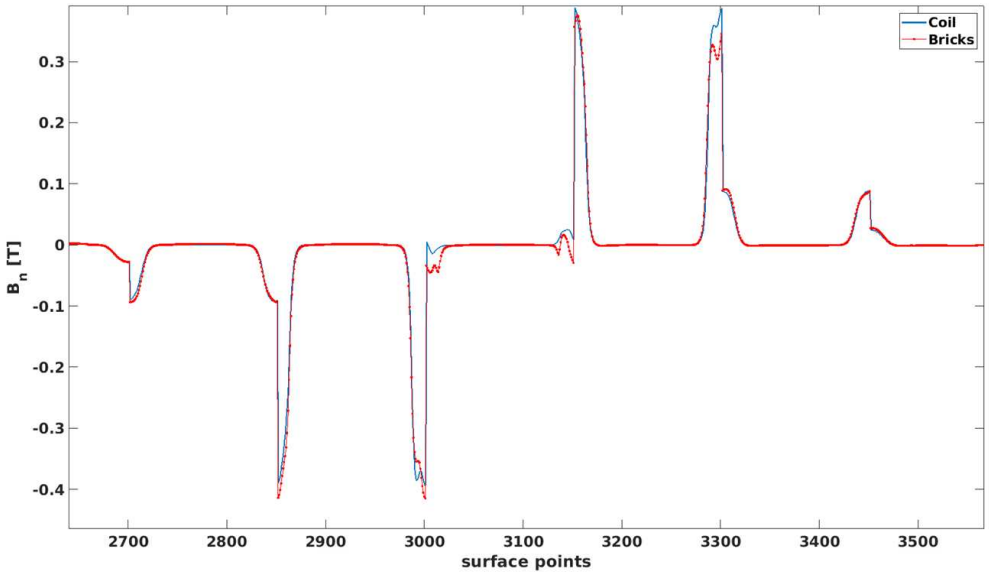

Figure 6.26: B_n behavior on the coupling surface: equivalent coil (blue curve) and hexahedrons model neglecting M_z for the hexahedrons (orange curve).

The results of the comparison show a good agreement between the two approach when only the toroidal magnetization is considered. In Tab. 6.14 the OVF computed using two approaches independently is shown. If M_z is included in the model based on the hexahedrons, an increasing of the OVF is observed about 70% probably due to the vicinity of the ports to the plasma. This amount of OVF, together with the one produced by the coils misalignments, might be dangerous since could overcome the threshold of 110 ppm. A drastic reduction of the OVF due to the ports can be obtained by re-establishing the toroidal periodicity of the ports, in this way they do not affect the n=1 anymore and make the corresponding OVF negligible (see an example in Fig. 6.27).

ECRH port model	**OVF [ppm]**
Hexahedral 6-ports	29
Equivalent 6-ports coils	20
Hexahedral 6-ports (including M_z)	83

Table 6.14: ECRH ports effects for three models

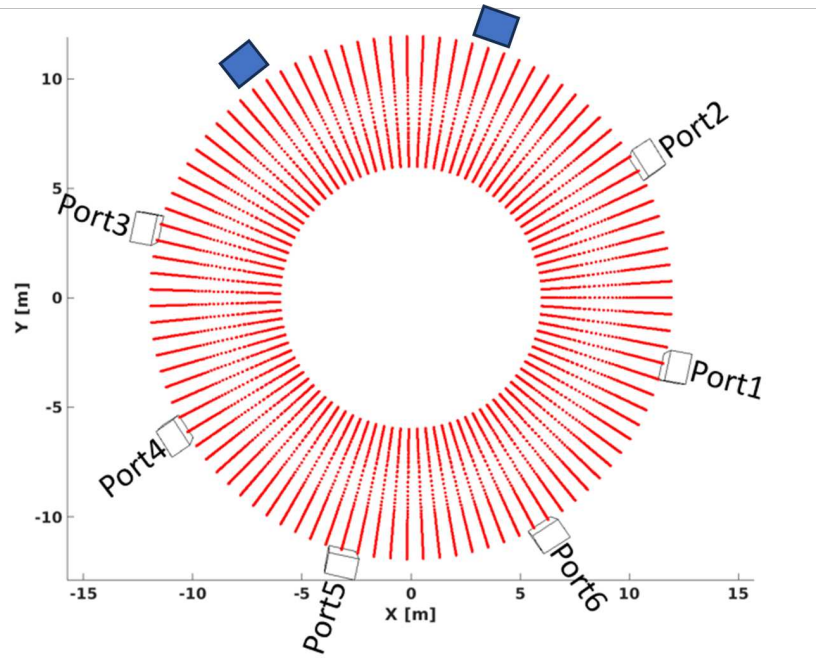

Figure 6.27: DEMO ports top view: initial 6-ports (white rectangles), two ports re-establishing the periodicity (blue rectangles) and the boundary of the plasma (red dashed crown).

6.4.2 Terminals connections OVF

For the purposes of this preliminary analysis, the presence of the transmission lines is considered negligible, as they consist of pairs of wires with opposite currents which are very close to each other in terms of distance to the coupling surface, and are therefore such that they cancel each other out. Since the design of the power supply in DEMO is still ongoing, just the boxes for the positioning of the terminals are available from the CAD projects. In Fig. 6.28a the boxes for the positioning of the terminals of PFs, CSs and TFs are sketched. Simplified model of the terminals consists in using rectangular filamentary currents. Fig. 6.28b shows the models used for the PFs terminals.

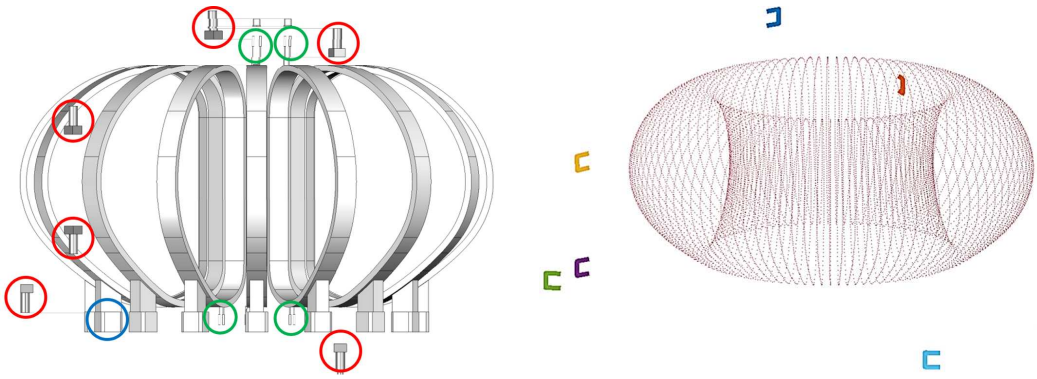

(a) (b)

Figure 6.28: Sketch of a) boxes containing DEMO terminals connections: 6 PFs(red circles), 5 CSs(green circles) and 16 periodic TFs(blue circles); b) PF terminals filamentary model

The normal component of the magnetic field for each filament has been calculated on the coupling surface and the OVF, $B^{\mathrm{OVF}}_{\mathrm{terminals}}$, returned using MARS-F. An appropriate relative error is introduced to characterise the weight of each terminal with respect to the expected OVF of the corresponding coil:

$$\mathrm{Error}\% = \left(\frac{B^{\mathrm{OVF}}_{\mathrm{Terminals}}}{B^{\mathrm{OVF}}_{\mathrm{Expexted}}} \right) \times 100 \tag{6.4}$$

where $B^{\mathrm{OVF}}_{\mathrm{Expexted}}$ was obtained from a Monte Carlo analysis by deforming the coil relative to the terminal studied.

In Tabs. 6.15 and 6.16, the results, for CS and PF terminals OVF respectively, are reported. The positioning of the TF terminals, which is periodic (n=16), does not affect the OVF and has been ignored.

	CS1	**CS2**	**CS3**	**CS4**	**CS5**
OVF Terminals (ppm)	0.17	0.15	0.21	0.02	0.15
Error%	8.41	11.7	23.45	9.85	7.52

Table 6.15: DEMO CS terminals effects in terms of OVF.

	PF1	**PF2**	**PF3**	**PF4**	**PF5**	**PF6**
OVF Terminals (ppm)	0.05	0.015	0.016	0.003	0.014	0.017
Error%	2.74	1.44	1.81	1.80	0.49	0.82

Table 6.16: DEMO PF terminals effects in terms of OVF.

The results show that the "PFs+CSs" terminals OVF is about 0.45 ppm, with a threshold of about 110 ppm, then < 1%.

6.5 Grad-Shafranov solutions with accurate magnetic field using linear triangular elements

The effectiveness of the method presented in chapter 4 has been assessed in two different applications for which analytical solutions are available. The first case refers to a linear problem. The second one shows the applicability to a nonlinear case. It is useful to define the relative error for the generic variable V used for method bench-marking:

$$\text{err} = \frac{\|V_{\text{num}} - V_{\text{an}}\|}{\|V_{\text{an}}\|} \tag{6.5}$$

where V_{num} is the numerical evaluation of V and V_{an} the analytical one.

6.5.1 Application to a linear problem

The linear problem considered for bench-marking is taken from [13]. Assuming the following current density profile:

$$\begin{aligned} J_\phi(\psi) &= \frac{S}{\mu_0} r + \frac{1}{\mu_0 r}(T\psi + U) \\ \textit{with } p'(\psi) &= \frac{S}{\mu_0} \quad \textit{and} \quad f f'(\psi) = T\psi + U \end{aligned} \tag{6.6}$$

with S, $T > 0$, U arbitrary constant parameters, the following analytical expression verifies Grad-Shafranov equation (4.5) for arbitrary values of the integration constants c_1, c_2, z_0 and k (with $k^2 \leq T$):

$$\psi(r,z) = rJ_1\left(\sqrt{T-k^2}r\right)\left[c_1 cos(k(z-z_0)) + c_2 sin(k(z-z_0))\right] \tag{6.7}$$

where J_1 is the first kind order-one Bessel function. The following choice of parameters has been made: S=0.75, U=2, T=17.8116, z_0=0.08667, k=$\sqrt{T}/2$, c_1=0.17795, c_2=-0.03291, expressed in SI units.

To fix the boundary conditions for a feasible tokamak plasma, a boundary with a constant ψ_b=-0.25 Wb/rad has been obtained from (6.7), fixing the value of r in a certain range and calculating the corresponding two solutions for z:

$$z_1 = z_0 + \frac{1}{k}\left[sin^{-1}\left(-\frac{C}{\sqrt{A^2+B^2}}\right) - tan^{-1}\left(\frac{B}{A}\right)\right] \tag{6.8}$$

$$z_2 = z_0 + \frac{1}{k}\left[\pi - sin^{-1}\left(-\frac{C}{\sqrt{A^2+B^2}}\right) - tan^{-1}\left(\frac{B}{A}\right)\right] \tag{6.9}$$

where:

$$A = rJ_1\left(\sqrt{T-k^2}r\right)c_2 \tag{6.10}$$

$$B = rJ_1\left(\sqrt{T-k^2}r\right)c_1 \tag{6.11}$$

$$C = -\frac{Sr^2}{T} - \frac{U}{T} - \psi_b \tag{6.12}$$

Fig. 6.29a shows the plasma region and the equilibrium flux. Fig. 6.29b illustrates the magnitude of the poloidal field. Fig. 6.29c shows the lines where the present procedure provides zero values of the two components of the poloidal field. The intersection of the two lines provides an estimation of the magnetic axis, where both components are zero. This procedure is also applicable for the localization of X-points at the plasma boundary or elsewhere. Fig. 6.29d shows that the accuracy is far better than the first order procedure, for which magnetic axes and X-points are necessarily nodes of the grid. Fig. 6.30 shows the behavior of the relative error of the numerical flux, its derivative and the magnetic field, highlighting the convergence rate of $O(h^2)$.

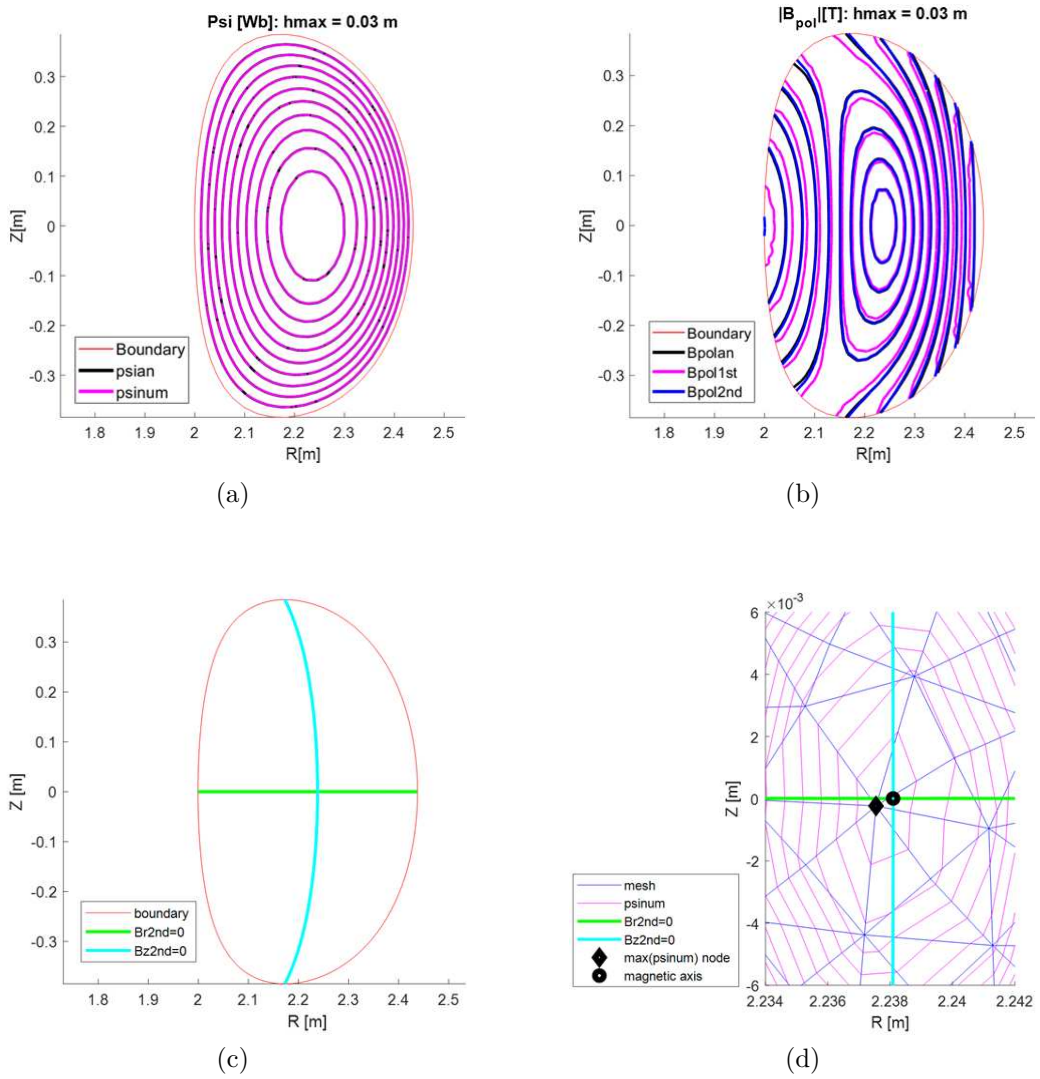

Figure 6.29: Comparison with the analytical solution of the linear problem reported in [13] in the plasma region 1.99925m $\leq r$ 2.43763m, $z_1(r) \leq z(r) \leq z_2(r)$: a) poloidal flux per radian ψ, where psian and psinum are the analytical and numerical solutions, respectively; b) magnitude of the poloidal field $|\boldsymbol{B}_{pol}|$, where Bpolan is the analytical solution, Bpol1st is the solution obtained by the standard technique in terms of ψ used in the first step and Bpol2nd the one obtained by the present procedure; c) curves where the two components of Bpol2nd are zero; d) exact position of the magnetic axis (black circle) compared to the evaluation of the first order procedure (black diamond, at a distance of 0.60 mm) and the estimation provided by the present procedure (intersection of the thick curves, at a distance of less than 0.01 mm).

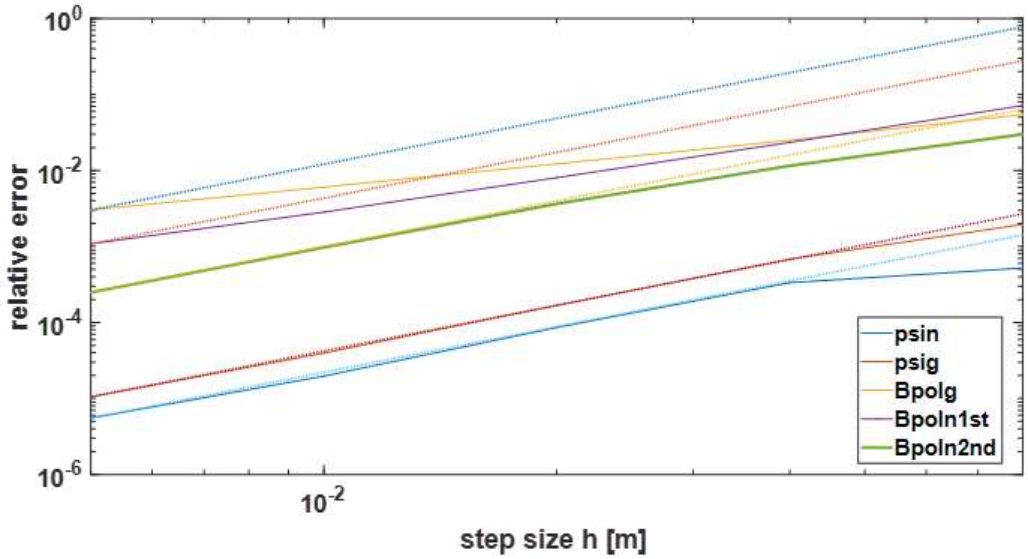

Figure 6.30: Linear problem [13]: relative error, defined in (6.5), of the numerical flux, its derivative and the magnetic field as functions of the mesh size h, highlighting (dash lines) the convergence rate of $O(h^2)$. Here psin refers to the nodal values of ψ, psig and Bpolg to the barycentric values of ψ and Bpol, respectively, provided by the standard solver in terms of ψ; Bpoln1st corresponds to the interpolation from Bpolg to nodal values of Bpol; Bpoln2nd refers to the nodal values of Bpol provided by the present procedure.

6.5.2 Application to a non-linear problem

The non-linear problem considered for benchmark is taken from [14]. Assuming the following current density profile:

$$J_\phi(\psi) = \frac{\psi^2}{r}\left(\frac{k_1}{3} + \frac{2k_1^2(z+c_1)^2\psi}{9} + 18a^2r^2\psi\right) \tag{6.13}$$

with a, c_1 and k_1 arbitrary constant parameters, the following analytical expression verifies Grad-Shafranov equation (4.5):

$$\psi(r,z) = -\frac{6}{9ar^2 + k_1(z+c_1)^2} \tag{6.14}$$

The family of solutions given by (6.14) has constant flux lines that are ellipses centered at $r = 0$. For this reason, they cannot represent real plasma configurations in a tokamak. Nevertheless, they can be used to test the effectiveness of the present procedure. Thus, the following choice of parameters has been made: a=5/9, k_1=0.8, c_1=-0.1, all expressed in SI units. The boundary is a polygon where (6.14) has been applied in order to fix non-uniform boundary conditions.

Fig. 6.31 shows the plasma boundary, the equilibrium flux and the magnitude of the poloidal field. Fig. 6.32 shows the behavior of the relative error of the numerical flux, its derivative and the magnetic field, highlighting the convergence rate of $O(h^2)$.

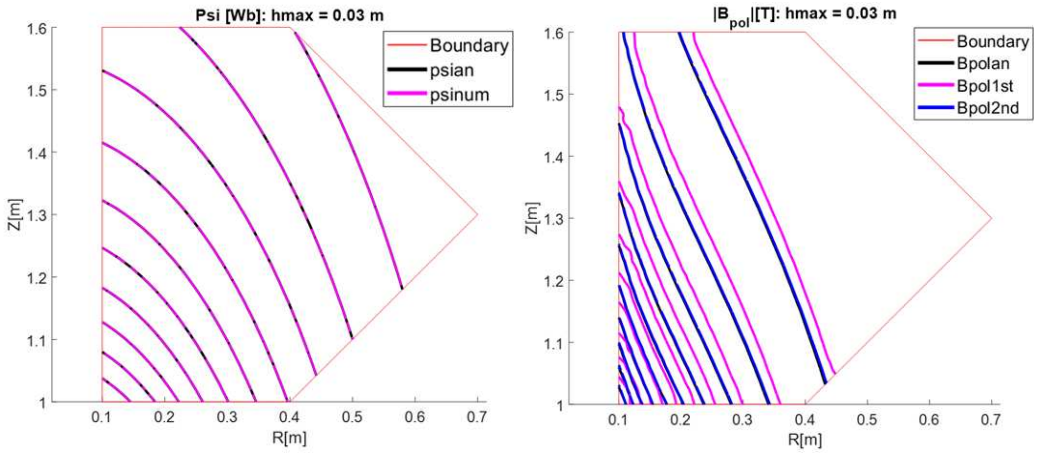

(a) (b)

Figure 6.31: Comparison with the analytical solution of the nonlinear problem reported in [14] inside the plasma region defined by the polygon with vertices [r[m], z[m]]=[0.1,1], [0.4,1], [0.7,1.3], [0.4,1.6], [0.1,1.6]: a) poloidal flux per radian ψ; b) magnitude of the poloidal field $|\boldsymbol{B}_{pol}|$. The legends psian, psinum, Bpolan, Bpol1st, and Bpol2nd are defined in Fig. 6.29.

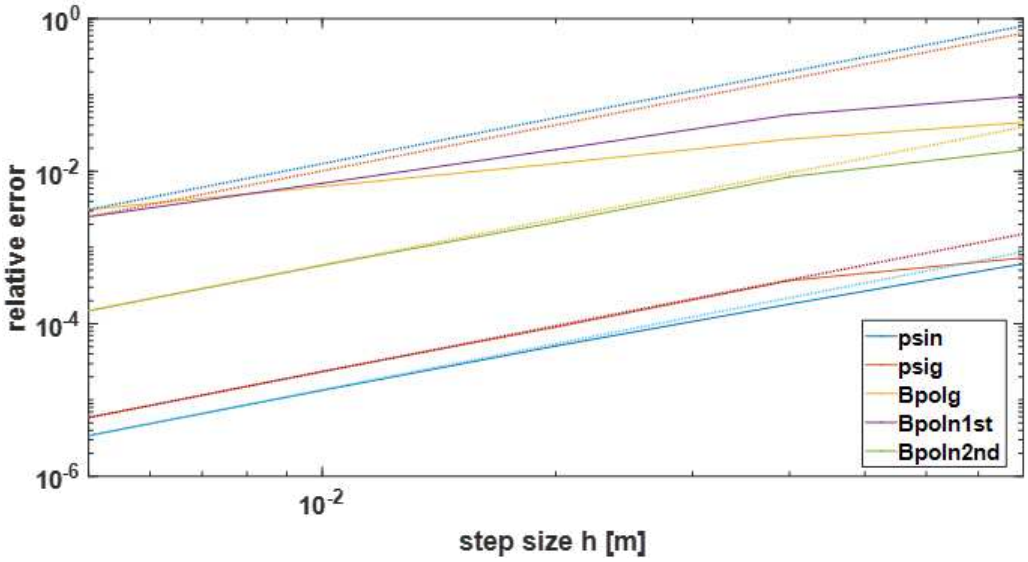

Figure 6.32: Nonlinear problem [14]: relative error, defined in (6.5), of the numerical flux, its derivative and the magnetic field as functions of the mesh size h, highlighting (dash lines) the convergence rate of $O(h^2)$. The legends psin, psig, Bpolg, Bpoln1st, and Bpoln2nd are defined in Fig. 6.30.

Bibliography

[1] R. Martone, et al. (Eds.), DTT Divertor Tokamak Test facility Interim Design Report, ENEA ("Green. Book"). ISBN 978-88-8286-378-4, https://www.dtt-dms. enea.it/share/s/avvglhVQT2aSkSgV9vuEtw, 2019.

[2] Castaldo, Aet al (2000). Plasma Scenarios for the DTT Tokamak with Optimized Poloidal Field Coil Current Waveforms. Energies. Energies, 15(5), 1702, 1804-1807. DOI: 10.3390/en15051702.

[3] Albanese, R., Bolzonella, T., Chiariello, A. G., Cucchiaro, A., Iaiunese, A., Lampasi, A., ... & Zumbolo, P. (2023). Error field and correction coils in DTT: A preliminary analysis. Fusion Engineering and Design, 189, 113437. https://doi.org/10.1016/j.fusengdes.2023.113437

[4] Author private communication.

[5] Matsunaga, G., Takechi, M., Sakurai, S., Suzuki, Y., Ide, S., & Urano, H. (2015). In-vessel coils for magnetic error field correction in JT-60SA. Fusion Engineering and Design, 98, 1113-1117. DOI: http://dx.doi.org/10.1016/j.fusengdes.2015.06.024.

[6] IAEA website, http://www-naweb.iaea.org/napc/physics/FEC/FEC2012 /papers/154 ITRP529.pdf

[7] Romanelli, G., Giannini, L., Martone, R., Ambrosino, R., Albanese, R., Zoboli, L., Zumbolo, P., ... & della Corte, A. (2023). Estimation of the error field due to winding manufacturing and assembly tolerances of the DTT SC magnet system. Fusion Engineering and Design, 192, 113588. https://doi.org/10.1016/j.fusengdes.2023.113588

[8] Mirizzi, F., Spassovsky, I., Ceccuzzi, S., Dattoli, G., Di Palma, E., Doria, A., ... & Force, E. C. T. (2015). A high frequency, high power CARM proposal for the DEMO ECRH system. Fusion Engineering and design, 96, 538-541. https://doi.org/10.1016/j.fusengdes.2015.02.026.

[9] De Marzi, G., Cucchiaro, A., De Baggis, F., della Corte, A., Giannini, L., Muzzi, L., & Di Zenobio, A. (2020). Electromagnetic Analysis of the Superconducting Magnet Feeders System of the Divertor Tokamak Testing Facility. Group, 1(6.0), 4-3. DOI:10.13140/RG.2.2.29556.99209

[10] Federici, G., Boccaccini, L., Cismondi, F., Gasparotto, M., Poitevin, Y., & Ricapito, I. (2019). An overview of the EU breeding blanket design strategy as an integral part of the DEMO design effort. Fusion Engineering and Design, 141, 30-42. https://doi.org/10.1016/j.fusengdes.2019.01.141

[11] Maviglia, F., Albanese, R., Ambrosino, R., Arter, W., Bachmann, C., Barrett, T., ... & Wenninger, R. (2018). Wall protection strategies for DEMO plasma transients. Fusion Engineering and Design, 136, 410-414. https://doi.org/10.1016/j.fusengdes.2018.02.064

[12] Fabbri, M. (2007). Magnetic flux density and vector potential of uniform polyhedral sources. IEEE Transactions on Magnetics, 44(1), 32-36. DOI: 10.1109/TMAG.2007.908698

[13] P. J. Mc Carthy, Analytical solutions to the Grad–Shafranov equation for tokamak equilibrium with dissimilar source functions, (1999), Physics of Plasmas, 6(9), pp. 3554-3560 DOI: 10.1063/1.873630. https://doi.org/10.1063/1.873630

[14] A. H. Khater, S.M. Moawad, Exact solutions for axisymmetric nonlinear magnetohydrodynamic equilibria of aligned magnetic field and plasma flow with applications to astrophysics and plasma confinement devices, (2009), Physics of Plasmas, 16. https://doi.org/10.1063/1.3127502

7 Conclusions

In this thesis work, the tool presented in Section 2.4, which utilizes a first-order Taylor approximation, was assessed and then employed to conduct a Monte Carlo analysis in order to map EFs in a tokamak. This analysis provided worst cases of EFs resulting from deviations of the magnets from their nominal configuration. Furthermore, a procedure for EFCCs current optimization for correction purposes has been developed. The EFs analysis was conducted for both the DTT and DEMO tokamaks.

For the DTT tokamak, the TMEI criterion was employed, whereas for DEMO, the Overlap field criterion was chosen to include the plasma response. EFs from manufacturing and assembly worst cases of DTT superconducting coils have been calculated and the required EFCC currents to push them below a given threshold in terms of TMEI. EFCC currents of 50 kAt are sufficient to correct the TMEI under 50 ppm with a 95% probability.

In DEMO, the analysis has shown that, when the CS+PF+TF set of EFs sources is randomly deformed, the outer array has required a maximum current of 180kAt to reduce the overlap field below 20 ppm for the worst cases, while the inner array requires a very high current. The reason is related to the cancellation of the main spectral components due to the proximity to the plasma. In addition, the study of ferromagnetic cut-outs will host ECRH antennas have shown a not negligible effect in terms of OVF (unless "precautions" on their disposition are taken); while about the magnet terminals connections effects, the analysis has shown a negligible OVF.

Finally, a formulation able to achieve continuity and convergence rate of order $O(h^2)$ for the magnetic field by using three-node linear triangles, based

on an application of Helmholtz's theorem, has been presented. These properties are very useful, providing a high level of accuracy and the possibility of deriving reliable linearized models with a limited computational effort. The procedure has been extended so as to be applied to nonlinear elliptic problems, in particular to the solution of Grad-Shafranov equation. It can be implemented as a post-processor of the magnetic flux solution obtained with linear triangles. The effectiveness of the method has been shown in linear and nonlinear cases for which analytical solutions are available.

8 Publications

8.1 Published and/or presented

1. Albanese, R., Chiariello, A. G., Fresa, R., Iaiunese, A., Martone, R., Zumbolo, P. (2022). Effectiveness of the Chebyshev Approximation in Magnetic Field Line Tracking. Energies, 15(20), 7619.

2. Albanese, R., Bolzonella, T., Chiariello, A. G., Cucchiaro, A., Iaiunese, A., Lampasi, A., Martone R., Piron L., Pizzuto A., Zumbolo, P. (2023). Error Field and Correction Coils in DTT: a preliminary analysis. Fusion Engineering and Design, 189, 113437.

3. Bolzonella, T., Pigatto, L., Piron, L., Villone, F., Albanese, R., Bonotto, M., ... & Zumbolo, P. (2022, June). Physics based design of a multi-purpose non-axisymmetric active coil system for the Divertor Test Tokamak. In 48th EPS Conference on Plasma Physics.

4. Albanese, R., Chiariello, A. G., Di Grazia, L. E., Iaiunese, A., Martone, R., Mattei, M., ... & Zumbolo, P. (2023). Three-dimensional evaluation of the connection lengths in a Tokamak. Fusion Engineering and Design, 192, 113622.

5. Albanese, R., Iaiunese, A., & Zumbolo, P. (2023). Solution of Grad-Shafranov equation with linear triangular finite elements providing magnetic field continuity with a second order accuracy. Computer Physics Communications, 108804.

6. Romanelli, G., Giannini, L., Martone, R., Ambrosino, R., Albanese, R., Zoboli, L., Zumbolo, P., ... & della Corte, A. (2023). Estimation of the error field due to winding manufacturing and assembly tolerances of the DTT SC magnet system. Fusion Engineering and Design, 192, 113588.